Carnegie Mellon University
MELLON COLLEGE OF SCIENCE

THESIS

SUBMITTED IN PARTIAL FULFILLMENT OF THE REQUIREMENTS
FOR THE DEGREE OF

DOCTOR OF PHILOSOPHY IN THE FIELD OF PHYSICS

TITLE: **"**Search for supersymmetry using leptons and jets and no missing transverse energy."

PRESENTED BY: Benjamin Carlson

ACCEPTED BY THE DEPARTMENT OF PHYSICS

James Russ	04/25/15
JAMES RUSS, CHAIR PROFESSOR	DATE
Stephen Garoff	04/25/15
STEPHEN GAROFF, DEPT HEAD	DATE

APPROVED BY THE COLLEGE COUNCIL

Fred Gilman	04/25/15
FRED GILMAN, DEAN	DATE

Probing the standard model: a search for supersymmetry in events with leptons, jets, and no missing transverse energy and a production study of $\Upsilon(1S)$, $\Upsilon(2S)$, and $\Upsilon(3S)$ states at high tranvserse momentum

Benjamin T. Carlson

Submitted in partial fulfillment of the
requirements for the degree of
Doctor of Philosophy
at
Carnegie Mellon University
Department of Physics
Pittsburgh, Pennsylvania

Advised by Professor James Russ

April 22, 2015

Abstract

This thesis presents two results: a search for supersymmetry (SUSY) and a measurement of the $\Upsilon(n\mathrm{S})$ (n = 1, 2, 3) cross sections as a function of the Υ transverse momentum. Both results are based on data from pp collisions at $\sqrt{s} = 7\,\mathrm{TeV}$ and $\sqrt{s}$ = 8 TeV collected with the Compact Muon Solenoid (CMS) detector at the CERN Large Hadron Collider (LHC). The two topics examine different aspects of the standard model. The mechanism for producing heavy-quark bound states in pp collision remains elusive despite 40 years of study. This measurement provides new data that will contribute to the understanding of how heavy-quark bound states are produced. In a different way, the search for supersymmetry attacks a weakness of the present formulation of the standard model related to the very high energy behavior of the fundamental interactions. The two projects have the common goal of improving our knowledge of the properties of the standard model using data from the LHC.

Most searches for SUSY focus on the presence of large missing transverse energy $E_{\mathrm{T}}^{\mathrm{miss}}$ carried away by the lightest SUSY particle. Recent searches at the CERN LHC using events with high $E_{\mathrm{T}}^{\mathrm{miss}}$ have found no found evidence for SUSY. Therefore, it is important to study well-motivated alternatives with low $E_{\mathrm{T}}^{\mathrm{miss}}$, such as models that include R-parity violation, where SUSY particles decay to SM particles. Similar low-$E_{\mathrm{T}}^{\mathrm{miss}}$ final states can be achieved in R-parity conserving scenarios, such as "stealth SUSY" by means of a new hidden sector in which SUSY is approximately conserved. This thesis presents results of a search for stealth SUSY using events that contain an electron and a muon. The search is the first of its kind. It uses proton-proton colliding beam data collected with the CMS detector in 2012, and corresponds to $19.7\,\mathrm{fb}^{-1}$ of integrated luminosity at a center of mass energy of 8 TeV. No excess of events is observed. A lower limit of 550 GeV is placed on the mass of possible degenerate first and second-generation squarks that decay in the stealth SUSY framework.

Differential cross sections as a function of transverse momentum p_{T} are presented for the production of $\Upsilon(n = 1, 2, 3)$ states decaying into a pair of muons. Data corresponding to an integrated luminosity of $4.9\,\mathrm{fb}^{-1}$ in pp collisions at $\sqrt{s} = 7\,\mathrm{TeV}$ were collected with the CMS detector at the LHC. The analysis selects events with dimuon rapidity $|y| < 1.2$ and dimuon transverse momentum in the range $10 < p_{\mathrm{T}} < 100\,\mathrm{GeV}$. The measurements show a transition from an exponential to a power-law behavior at $p_{\mathrm{T}} \approx 20\,\mathrm{GeV}$ for the three Υ states. Above that transition, the $\Upsilon(3S)$ spectrum is significantly harder than that of the $\Upsilon(1S)$ and $\Upsilon(2S)$. The ratios of the $\Upsilon(3S)$ and $\Upsilon(2S)$ differential cross sections to the $\Upsilon(1S)$ cross section show a rise as p_{T} increases at low p_{T}, then become flatter at higher p_{T}.

Acknowledgments

I would like to thank all of the friends I have made in particle physics over the last few years, who have made my Ph.D. experience fun. Graduate students I would like to thank are Yutaro Iiyama, for help with life at CERN as well as technical questions. I would like to thank Andrew Brinkerhoff and Joe Goodell for always being up for an adventure near CERN. I would like to thank Brian Francis for always being willing to help and collaborate with technical issues. At Fermilab, I would like to thank Tutanon Sinthuprasith and Sam Bein for always being willing to engage in lively discussion, and making the environment an exciting place to work in. I am particularly grateful to all of the stealth SUSY team; Marc Weinberg and Alexey Ferapotov were always willing to discuss things, remotely when necessary. Jim Hirschauer of course deserves special thanks for mentoring me over the last two years.

At CMU, I am grateful to Manfred Paulini for everything from supporting travel plans to CERN to introductions to the SUSY group and Tom Ferguson for help writing the upsilon cross section paper. Finally, I am particularly grateful to my advisor, Jim Russ. His door was almost always open, he was extremely accessible, and offered insightful advice on all sorts of problems from technical to general. From my time as an undergraduate, I would particularly like to thank Jeff Wolinski for encouraging me to pursue experimental physics, and particle physics in particular.

I am also thankful to my family for supporting my academic endeavors over the last few years. They were always encouraging. I am also thankful for the support of my wife, Jamie.

Contents

List of Tables

List of Figures

Chapter 1

Introduction

Particle physics is the study of the constituents of matter and their interactions. The ultimate goal of particle physics is to understand the most fundamental building blocks of the universe at the shortest distance scale possible. This is accomplished by studying processes at high energy. In addition, particle physics seeks to understand the unifying principles behind the interactions and learn to make predictions. Thus, particle physics is often thought of as the study of the most fundamental principles of nature.

The experimental tool for examining high energy processes is scattering. Ernest Rutherford's 1911 discovery of the nucleus using the scattering of Helium nuclei off of gold atoms is the prototypical particle physics experiment. During the 20th century, experimentalists became experts at increasing the energy of scattering experiments by accelerating charged particles with large electric field gradients. From these experiments, smaller levels of structure were discovered, including constituents of the nucleus. In the following decades, hundreds of other short-lived states were found.

As experimentalists increased the energy of scattering events, theorists were required to make calculations in a regime that required the use of both relativity and quantum mechanics. The tools of quantum field theory were at least in part invented as a way to keep up with the rapid experimental progress of high energy physics. These tools naturally allow for theories to be constructed in a way that is equivalent in all reference frames, or Lorentz invariant.

Eventually it became apparent that the tools of quantum field theory could be used to construct a single model that described all of the known particles. The standard model (SM) consists of two families of spin-$\frac{1}{2}$ particles: leptons and quarks. The interactions between these states are mediated by spin-1 particles: the W and Z bosons, the photon, and the gluon. The final ingredient is a spin-0 particle, called the Higgs boson. As will be described in the theory Section, this particle breaks the symmetry of the theory and gives mass to the particle content of the standard model. While it is not necessary that there be additional physics beyond the standard model, there are many compelling reasons to suspect that there is new physics. This will be

discussed in more detail in Section 2.

As will be described in Section 3, the Large Hadron Collider (LHC) is a proton-proton collider, designed to operate at a center-of-mass energy $\sqrt{s} = 14\,\text{TeV}$. The compact muon solenoid (CMS) detector records the collisions, and allows proton collisions to be studied. The LHC and CMS detector were designed to carry out detailed studies of the standard model, discovery the Higgs boson, and search for new physics at the TeV scale. Supersymmetry is a compelling extension of the standard model, and can be searched for at the LHC. A unique search for supersymmetry in a final state with one muon, one electron, at least four jets, and no missing transverse energy will be described in Section 4. In addition to searches for new physics, the LHC can study the strong production of quark bound states, such as the Υ meson. A measurement of the Υ cross section will be described in Section 5. The conclusions of these two analyses are discussed in Section 6.

Chapter 2

Theoretical motivation

2.1 The standard model

The SM is an effective field theory that describes all known particles and interactions as of 2015 [1]. The particles of the SM are summarized in Table 2.1, and consist of spin-1/2 fermions and spin-1 bosons. The fermions are quarks and leptons. There are six quarks that occur in three generations, the up and down quarks (u, d), the strange and charm (s, c), and the top and bottom (t, b). The leptons also occur in three generations, the electron and electron-neutrino (e, ν_e), the muon and muon-neutrino (μ, ν_μ), and the tau and tau-neutrino (τ, ν_τ). The interactions between leptons are mediated by the electroweak W and Z bosons and the photon. The quarks interact by electroweak boson exchange and have color charge and couple to the gluon, the mediator of the strong force.

The electroweak portion of the SM is described by four degrees of freedom, three of which have weak isospin ($W^{1,2}$, W^0) and one with weak hypercharge (B^0). These fields are characterized by their transformations under the gauge group $SU(2)_L \times U(1)_Y$, where SU(n) represents a special unitary group of order n, and U(1) the unitary group. The left-handed fields transform as doublets under SU(2) and right-handed

Table 2.1: Summary of the standard model particle content.

Name	spin	charge
leptons (e,μ,τ)	1/2	1
leptons (neutrinos: ν_e,ν_μ,ν_τ)	1/2	0
quarks	1/2	2/3(-1/3)
gluon	1	0
W	1	$\pm$1
Z	1	0
γ	1	0
Higgs	0	0

fields as singlets.

The $SU(2)_L \times U(1)_Y$ symmetry described above precludes terms that would give mass to the fermions or gauge bosons because such terms would not be gauge invariant. The gauge bosons and fermions obtain a mass from the method of spontaneous symmetry breaking [2, 3, 4, 5, 6]. A spin-0 field that is a doublet under the $SU(2)_L$ symmetry breaks the electroweak symmetry, where λ and μ^2 must be real, and λ positive. The scalar field can then break the $SU(2)_L \times U(1)_Y$ symmetry with a doublet of the form,

$$\Phi = \frac{1}{\sqrt{2}} \begin{pmatrix} 0 \\ v + H \end{pmatrix}, \tag{2.1}$$

where Φ is the scalar field, v the is the minimum of the potential that gives the scalar a non-zero vacuum expectation value, and H propagates around the new minimum v. With a potential,

$$V(\Phi^\dagger \Phi) = \lambda[\Phi^\dagger \Phi - \mu^2/2\lambda]^2, \tag{2.2}$$

the minimum of the field takes the value $v^2 = \mu^2/\lambda$. After the $SU(2)_L \times U(1)_Y$ symmetry is broken, the W^0 and B^0 fields mix to form the massive Z boson and the massless photon [7]. The other two degrees of freedom $W^{1,2}$ form the massive $W^\pm$ fields. The breaking of the $SU(2)_L \times U(1)_Y$ by the spin-0 field also allows for fermion masses. The spin-0 field itself is massive, and called the Higgs boson.

The strong interactions between quarks and gluons are described three color charges and their transformations under $\mathrm{SU}(3)_c$ in the theory of quantum chromodynamics (QCD) [8, 9, 10, 11]. The strength of the coupling α_s is a function of momentum transfer Q, and has the following form:

$$\alpha_s(Q) = \frac{2\pi}{b_0 log(\frac{Q}{\Lambda_{\mathrm{QCD}}})} \tag{2.3}$$

where b_0 is a constant, and $\Lambda_{\mathrm{QCD}} \approx 200\,\mathrm{MeV}$ (in this thesis, natural units will be used, where $\hbar = \mathrm{c} = 1$) is the scale where the QCD interaction is strong. For values of Q much larger than this value, the strong coupling is small, and thus it is said that QCD is "asymptotically" free. Though quarks are charged under the SU(3) symmetry and have color, and the observable particles only occur in color-neutral combinations [12] called hadrons. Hadrons can occur as mesons or baryons. Mesons are bound states of a quark and an antiquark, such as the Υ, which has the valence quark composition $|b\bar{b}\rangle$. Baryons are bound states of three quarks such, including the proton, which has the valence quark composition $|udd\rangle$.

The SM describes the interactions between quarks, leptons, and bosons, as characterized by the transformations under the gauge group: $SU(3)_c \times SU(2)_L \times U(1)_Y$, and a scalar field with a non-zero vacuum expectation value. The structure of the SM described above is extremely successful, it is worth pointing out that it is deduced from experimental observations, and not derived from first principles.

One of the issues with the SM is how to perform calculations that describe the QCD interactions needed to form low-mass states, which will be discussed in the Section 2.2. The other issues with the SM point to more general signatures of new physics. The hierarchy problem is related to the fact that the SM is a low energy effective field theory when viewed from the perspective of the Planck scale at which gravity becomes strong. This is a particularly interesting problem in the context of a 125 GeV Higgs boson, as discovered by the ATLAS and CMS Collaborations [13, 14] in 2012. The issue is that in the high-energy limit of the SM, the Higgs mass is sensitive to positive radiative corrections that would naively make the Higgs mass larger than 125 GeV. Independently, astrophysical observations suggest that approximately 25% of the combined mass and energy of universe is composed of dark matter (DM). Supersymmetry is one promising approach that promises to solve both of the hierarchy problem and provide a candidate for DM. A more detailed description of the hierarchy problem, DM and supersymmetry will be provided in the following sections.

2.2 Quarkonium production

In the production of heavy-quark states, the quark production happens rapidly, at a time $t \propto \frac{1}{\Lambda_Q}$, where Q is the momentum transfer. The hardronization, where color-neutral hardrons are formed occurs at a later time $t \propto \frac{1}{\Lambda_{QCD}}$. At a hadron collider, the quark production can generally be computed using perturbative QCD, while the hardonization involves non-perturbative terms.

Models that describe production of heavy-quarks must correctly describe both terms. Measurements of $b\bar{b}$ mesons, such as Υ states, provide an important probe of QCD, and a method to evaluate these models. A common feature of models such the color singlet model [15] and the k_t-factorization model [16] are that various terms have different p_{T} dependence, some of which are power-law forms. The non-relativistic QCD (NRQCD) approach [17, 18] assumes that the relative velocity between the quarks is low enough that it can be expanded in powers of velocity. This expansion includes long-distance matrix element (LDME) terms that depend on the non-perturbative dynamics, and are typically evaluated using fits to data. There are calculations using the NRQCD methods with next-to-leading-order (NLO) corrections [19], which have recently been extended to describe production of all three $\Upsilon(n\mathrm{S})$ (n = 1, 2, 3) states for p_{T} up to 100 GeV. To clarify the theoretical picture, new measurements that emphasize the high-p_{T} cross section are needed.

2.3 Supersymmetry

Supersymmetry (SUSY) [20] relates fermion states $|f\rangle$ to boson states $|B\rangle$, as generated by the operator Q:

$$Q\,|B\rangle = |f\rangle\,, Q\,|f\rangle = |B\rangle\,. \tag{2.4}$$

SUSY was first proposed as a spacetime symmetry between fermions and bosons during the 1970's [21], and leads to an additional set of states that differ from the SM partners only by spin. A summary of the supersymmetric particle content is listed in Table 2.2.

SUSY subsequently began to generate substantial interest when it was learned that it can potentially solve the hierarchy problem, unify the strong, weak, and electromagnetic coupling strengths, and provide a DM candidate. On the other hand, SUSY predicts that for each SM particle, there should be a "superpartner" with the same mass but different spin. This point is trivially falsified by the lack of evidence for this supersymmetric spectrum. SUSY must be a broken symmetry. There must be some portion of the SUSY Lagrangian, denoted $\mathcal{L}_{\text{soft}}$ that contains terms that break the symmetry. As usual in a broken symmetry, $\mathcal{L}_{\text{soft}}$ obeys the symmetry it breaks. The remainder of the SUSY Lagrangian, including the Yukawa and gauge, terms are contained in the term $\mathcal{L}_{\text{SUSY}}$, so the total Lagrangian is:

$$\mathcal{L} = \mathcal{L}_{\text{SUSY}} + \mathcal{L}_{\text{soft}}. \tag{2.5}$$

2.3.1 Hierarchy problem

In the SM, the Higgs mass is sensitive indirectly to all physics between M_W and the Planck mass $M_P \approx 10^{18}\,\text{GeV}$ due to quantum corrections, such as the diagram shown in Fig. 2.1. The corrections to the square of the Higgs boson mass ΔM_h^2 have the

Table 2.2: Summary of the supersymmetric particle content. Note that the partners to the gauge fields and Higgs bosons are listed before electroweak symmetry breaking, hence the name "Bino".

Name	spin	charge
sleptons ($\tilde{e}$, $\tilde{\mu}$, $\tilde{\tau}$)	0	1
sneutrinos ($\tilde{\nu_e}$, $\tilde{\nu_\mu}$, $\tilde{\nu_\tau}$)	0	0
squarks ($\tilde{q}$)	0	2/3(-1/3)
gluino ($\tilde{g}$)	1/2	0
Wino ($\tilde{W}$)	1/2	± 1
Bino ($\tilde{B}$)	1/2	0
Higgsinos ($\tilde{H}$)	1/2	0

form,

$$\Delta M_h^2 \approx \lambda_f^2 \int d^4k \frac{k^2 + m}{(k^2 + m^2)^2}. \tag{2.6}$$

If the momentum k from the integral in Eq. 2.6 is regulated using a cutoff scale Λ, then the corrections to the Higgs mass are approximately,

$$\Delta M_h^2 \approx \lambda_f^2 \Lambda^2. \tag{2.7}$$

According to Eq. 2.7, corrections to the Higgs mass are proportional to Λ^2. The issue is that the SM applies to energies at the scale $M_W \approx 100\,\text{GeV}$, while the effects of quantum gravity become relevant at M_P. If Λ is allowed to be as large as M_P, it is extremely difficult to obtain a Higgs mass of 125 GeV without some way to cancelation divergent term in Eq. 2.7. SUSY provides a way to cancel these divergent pieces by introducing a scalar. The corrections to the Higgs mass then receive contributions from the scalar diagram in Fig. 2.1, so that:

$$\Delta M_h^2 = (\lambda_S - \lambda_f^2)\Lambda^2. \tag{2.8}$$

If $\lambda_S = \lambda_f^2$, as is the case in an unbroken symmetry, the correction terms automatically cancel. To maintain the requirement that the scalar and fermion couplings be equal once the symmetry is broken, we refer back to Eq. 2.5, where the largest mass scale in the SUSY breaking sector is denoted by m_{soft}. The corrections to the Higgs mass then diverge logarithmically in Λ:

$$\Delta M_h^2 = m_{\text{soft}}^2[ln(\Lambda/m_{\text{soft}})]. \tag{2.9}$$

Since the scale m_{soft} sets the scale for the mass difference between SM and SUSY, m_{soft} cannot be too large without reintroducing the hierarchy problem. Thus, even though SUSY is a broken symmetry, it can still solve the hierarchy problem if the masses of the superpartners are not too large [22].

2.3.2 Dark matter

Astrophysical observations suggest that 25% of the combined mass and energy of the universe is non-luminous, non-absorbing "Dark Matter" (DM). DM was proposed to

Figure 2.1: One-loop corrections to the square of the Higgs mass due to (left) a fermion (f) and (right) a scalar (S).

explain the rotational velocity distribution of stars orbiting in galaxies [23]. For a star orbiting around a galaxy with mass distribution $M(r)$ enclosed at radius r, the expected velocity distribution from Newton's laws is $v(r) \approx \sqrt{M(r)/r}$. This velocity distribution can be calculated based on the mass distribution determined from stars and other optically observable matter, and is expected to peak then drop off for large values of r. Observational evidence instead finds that the velocity approaches a constant with increasing r. This suggests that the galaxy also includes matter that cannot be optically detected.

In addition, DM can be detected by gravitational lensing [24], which occurs when light is deflected around mass objects. The lensing effect is equivalent to the first experimental test of general relativity: the deflection of starlight passing near the edge of the sun. A depiction of gravitational lensing is shown in Fig. 2.2, where the lensing effect is seen in the arcs.

There are a variety of models that attempt to explain the particle content of DM [25]. SUSY provides several popular candidates. Among the candidates are a neutralino χ_1^0 that commonly occurs in the minimal supersymmetry standard model

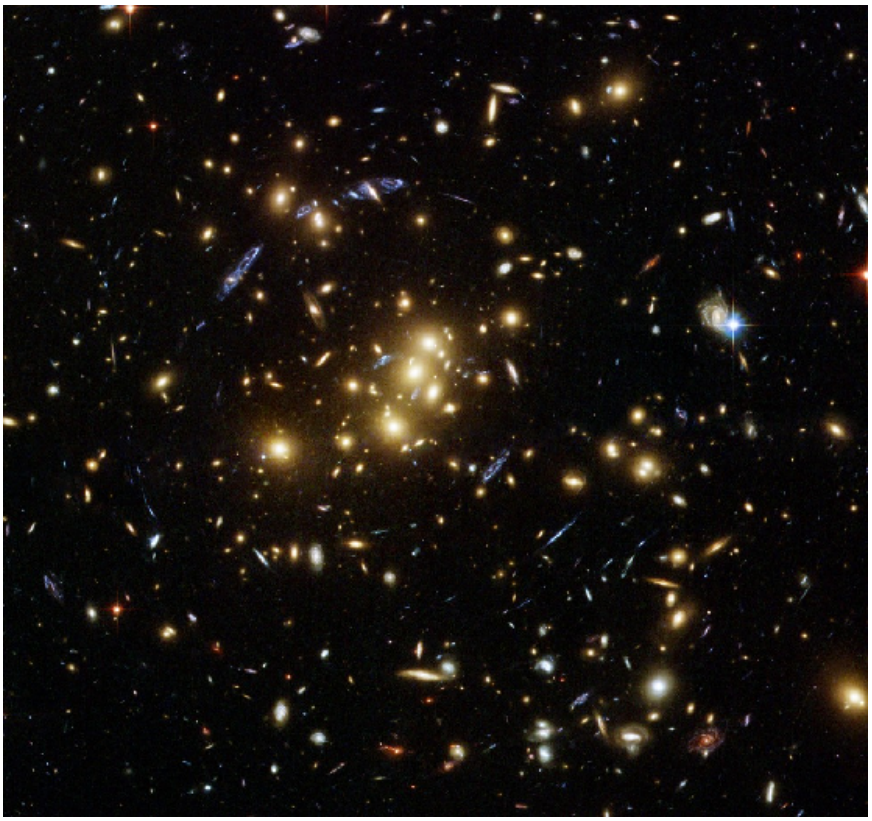

Figure 2.2: Gravitational lensing can be seen in the distorted arcs due to the invisible DM.[24].

(MSSM) and the gravitino $\tilde{G}$ related to gravitationally mediated SUSY breaking (GMSB) [26]. In the MSSM there are four neutralinos that are linear combinations of the electroweak superpartners ($\tilde{B}$, $\tilde{W}$) and the Higgs superpartners ($\tilde{H}_d$, $\tilde{H}_u$). The lowest-mass eigenstate χ_1^0 can be a stable DM candidate.

2.3.3 Unification of couplings

Given that the electroweak unification program successfully described the weak and electromagnetic interactions as part of the same phenomena, people started to wonder if all the interactions could be understood in a single framework [27]. In 1974, Georgi and Glashow proposed that the SM gauge group $SU(3)_c \times SU(2)_L \times U(1)_Y$ is really the low-energy limit of a single theory with only one coupling constant and gauge group [28]. They argued that the simplest group that contains $SU(3)_c \times SU(2)_L \times U(1)_Y$ is SU(5).

An interesting consequence is that the running of the couplings from the weak scale to high energy results in a clustering of the three couplings of the $SU(3)_c \times SU(2)_L \times U(1)_Y$ gauge group at around 10^{16} GeV. What is even more striking is when SUSY particles are introduced, the high-energy limit of the inverse couplings all converge to the same value at 10^{16} GeV. The three inverse coupling constants in Fig. 2.3 are computed for a specific choice of m_{soft}. Varying m_{soft} changes the Q value at which the MSSM predictions deviate from the SM predictions. In Fig. 2.3, the blue curves are computed using $m_{soft} = 500\,\text{GeV}$, and the red curves with $m_{soft} = 1.5\,\text{TeV}$.

2.3.4 Searches for SUSY

At the LHC, SUSY particles can be produced by gluon-gluon, gluon-quark, or quark-antiquark scattering. Exchange of an electroweak boson (W, γ/Z) can also produce electroweak gauginos and sleptons. Cross Sections from strong processes have coupling strength related to QCD and are larger than electroweak SUSY production cross sections. A few sample diagrams are depicted in Fig. 2.4.

Typical SUSY searches emphasize decays of gluinos and squarks that terminate in a high-momentum, stable, neutral particle. The simplest example is the decay: $\tilde{q} \rightarrow q\tilde{\chi}_1^0$ where $\tilde{\chi}_1^0$ is the lightest SUSY particle (LSP). The LSP is neutral and escapes undetected, resulting in missing transverse momentum $\vec{p}_{\text{T}}^{\,\text{miss}}$. This quantity is the projection of the negative vector sum of the p_{T} of all invisible particles:

$$\vec{p}_{\text{T}}^{\,\text{miss}} = -\sum_k \vec{p}_{\text{T}\,k}^{\,\text{inv}}. \tag{2.10}$$

The magnitude of $\vec{p}_{\text{T}}^{\,\text{miss}}$ is referred to as $E_{\text{T}}^{\text{miss}}$. Since this Eq. 2.10 is evaluated as a vector sum over invisible particles, if there are multiple invisible particles, then the vectors can cancel and result in a small $E_{\text{T}}^{\text{miss}}$. For example, if two invisible particles are produced back to back, so the invisible p_{T} vectors from Eq. 2.10 cancel and result

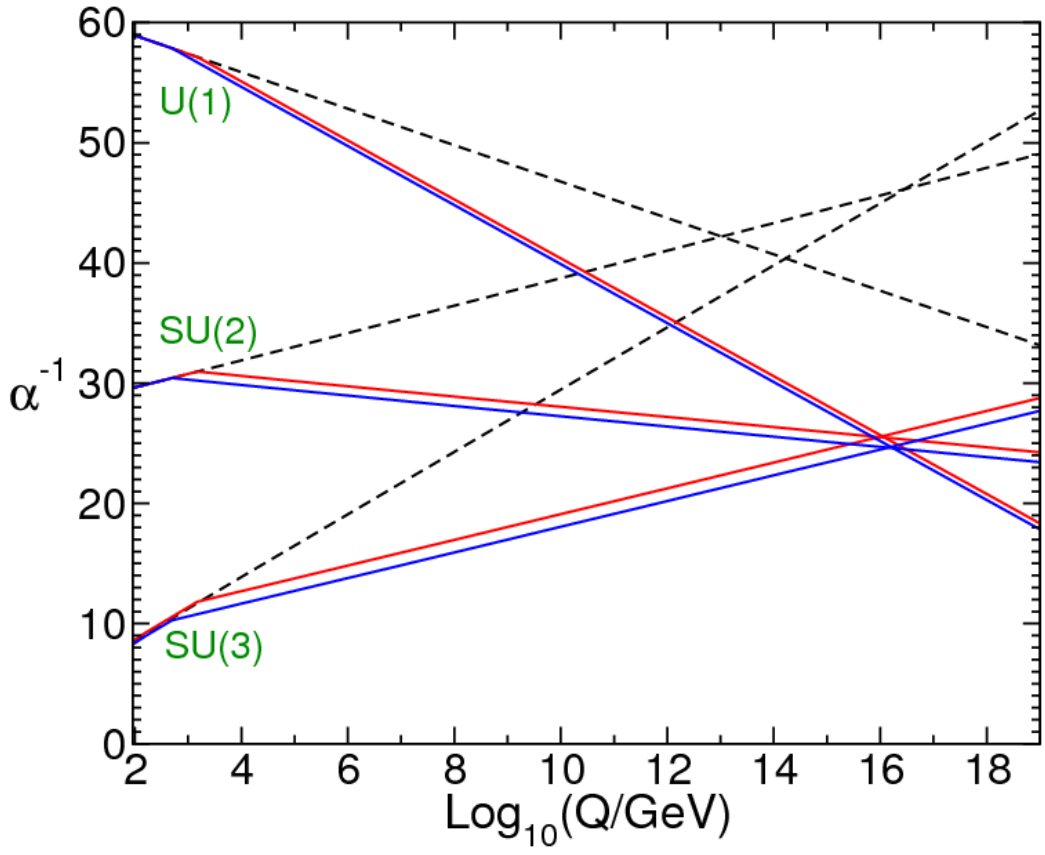

Figure 2.3: Two-loop renormalization group evolution of the inverse of the gauge couplings α^{-1} [20]. The solid lines are the result of the group evolution in the MSSM with different values of m_{soft} and the dashed lines are the result of the calculation in the SM.

in no $E_{\mathrm{T}}^{\mathrm{miss}}$. In general, this occurs in only a fraction of the decays, since initial-state radiation can boost both LSPs and the total $E_{\mathrm{T}}^{\mathrm{miss}}$ is again large. SUSY decays typically result in substantial $E_{\mathrm{T}}^{\mathrm{miss}}$ due to high p_{T} invisible particles. In these decays, it is typically assumed that R-parity is conserved, where $R = 1$ for SM particles and R = -1 for SUSY particles. As a result, SUSY particles cannot decay to two SM particles. More complicated decays can include gauge bosons, quarks, and gluons leading to additional leptons and jets, in addition to $E_{\mathrm{T}}^{\mathrm{miss}}$.

None of these searches with $E_{\mathrm{T}}^{\mathrm{miss}}$ in the final state have so far seen evidence for SUSY. In addition, searches for top squark production have excluded some models up to a mass of near 600 GeV, as can be seen in Fig. 2.5 (left). These plots show the exclusion limits for a number of different analyses, interpreted in the same model. The solid (dashed) lines indicate the curve as a function of squark and LSP masses where the expected (observed) upper limit on the cross section for a given model is equal to the theoretical cross section. The region to the left and below the curves is

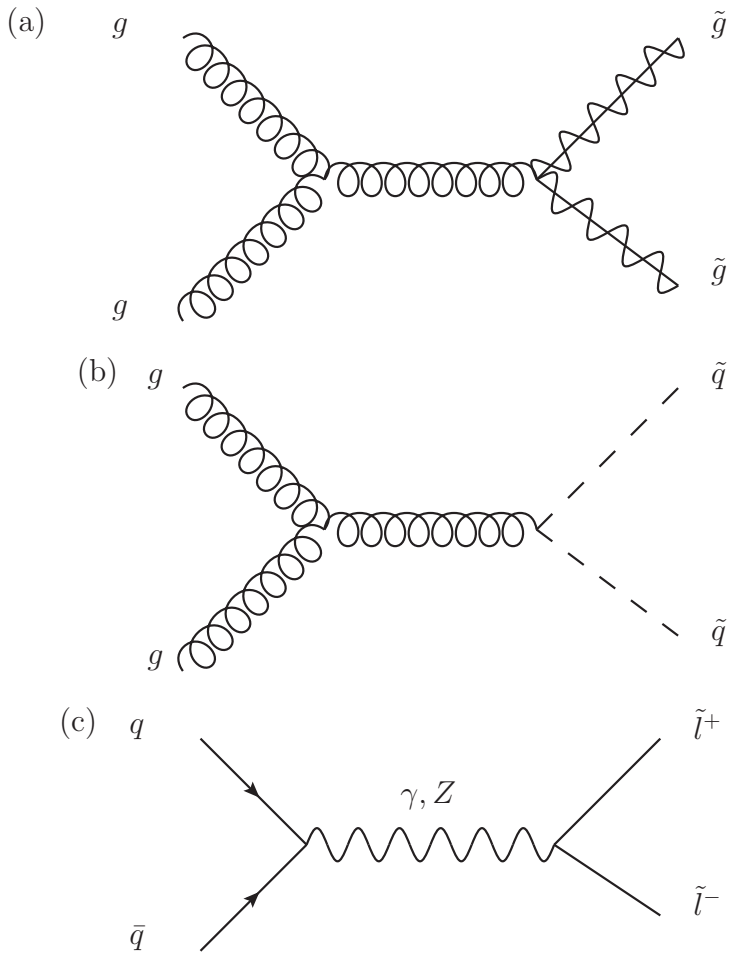

Figure 2.4: Feynman diagrams for various production modes of SUSY particles at the LHC. (a)One diagram of QCD-strength gluino production by gluon-gluon collisions. (b)Squark production by the same mechanism. (c)Electroweak production of sleptons.

excluded. Details of the statistics behind the limit-setting procedure will be described in Section 4.8.1. As can be seen in Fig. 2.5 (right), similar but more stringent limits exist for light-flavor squark production (assuming the $\tilde{u}$, $\tilde{d}$, $\tilde{s}$, $\tilde{c}$ squarks are degenerate in mass). Though not shown here, gluinos with masses up to 1.3 TeV are excluded by LHC searches. If SUSY is to solve the hierarchy problem, there must be new physics near 1 TeV. The exclusion limits for SUSY with mass scales near 1 TeV have led to the introduction of SUSY models that do not produce $E_{\mathrm{T}}^{\mathrm{miss}}$. There are several ways to reduce $E_{\mathrm{T}}^{\mathrm{miss}}$ in SUSY decays, though some of these are overlapping categories:

- Compressed spectra: small mass differences between SUSY particles result in soft, invisible particles.
- Long decay chains: SUSY particles decay through many particles.

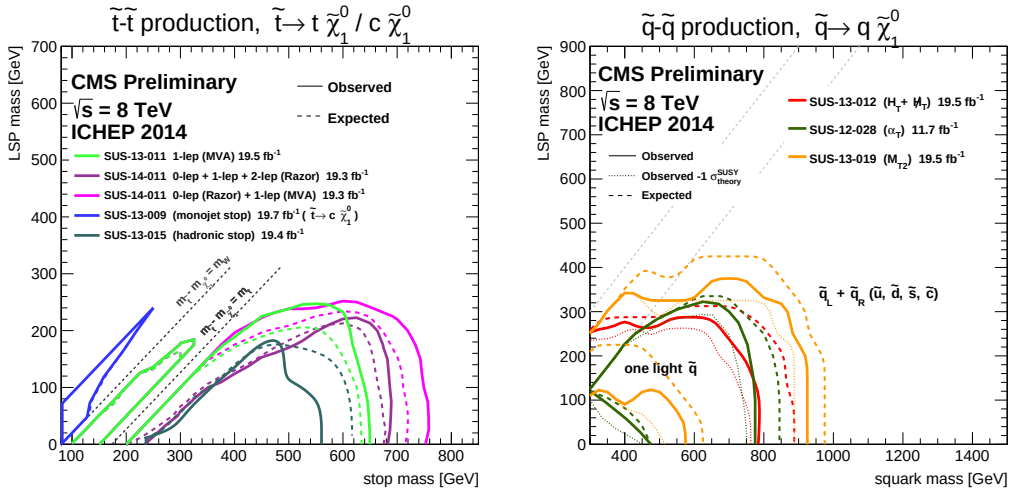

Figure 2.5: Exclusion limits for top squark production and light-flavor squark production.

- "Stealth" SUSY: low-$E_{\mathrm{T}}^{\mathrm{miss}}$ final state due to mass degeneracy enforced by SUSY in a hidden sector.
- R-parity violation (RPV): allows SUSY particles to decay directly to two SM particles.

R-parity violation

The superpotential terms that result in RPV can be characterized by three trilinears with Yukawa couplings λ_{ijk}, λ'_{ijk}, and λ''_{ijk}:

$$W_{\mathrm{RPV}} = \frac{1}{2}\,\lambda_{ijk} L_i L_j \overline{E}_k + \lambda'_{ijk} L_i Q_j \overline{D}_k \;+\; \frac{1}{2}\,\lambda''_{ijk} \overline{U}_i \overline{D}_j \overline{D}_k, \tag{2.11}$$

where i, j, and k are generation indices; L and Q are the $SU(2)_L$ doublet superfields of the lepton and quark; and the $\overline{E}$, $\overline{D}$, and $\overline{U}$ are the $SU(2)_L$ singlet superfields of the charged lepton, down-type quark, and up-type quark. A non-negligble product of couplings such as $\lambda \cdot \lambda'$ or $\lambda \cdot \lambda''$ is excluded by low-energy processes such as limits on the lifetime of the proton [29]. Constraints on RPV effects are less stringent for the third generation, and constraints can be weakened if only one of the RPV couplings is to be non-zero. Thus, a search is performed with only one non-zero RPV coupling allowed.

A top quark can decay directly by RPV. The decay $\tilde{t} \to \tau\ \bar{b}$ can occur via a non-zero coupling constant λ'_{333}. This is identical to the decay of a third-generation leptoquark (LQ) [30]. This SUSY decay does not result in $E_{\mathrm{T}}^{\mathrm{miss}}$. As can easily be seen by the flexibility of the RPV operators in Eq. 2.11, there are a variety of allowed decays not covered by the current search program [31].

"Stealth" SUSY

Models of "stealth" SUSY introduce a new hidden sector at the weak scale where SUSY is approximately conserved. This sector is referred to as the "stealth sector" and contains at least one set of nearly mass-degenerate superpartners. The mass degeneracy reduces the $\vec{p}_{\mathrm{T}}^{\,\mathrm{miss}}$ in the event. This occurs because the lightest "visible sector" SUSY particle (LVSP) (i.e., neutralino) can decay to the lighter stealth-sector particle, $\tilde{S}$. This decay chain starts with an R-odd squark. Therefore, the decay chain of the LVSP must end in an R-odd and R-even state. The simplest models terminate in a gravitino $\tilde{G}$ and the R-even S: $\tilde{S} \to \tilde{G}S$. Since S is even under R-parity, it can decay to SM particles, e.g., $S \to gg$, where g is a gluon. The entire decay chain is depicted in Fig. 2.6. Thus, the only $E_{\mathrm{T}}^{\mathrm{miss}}$ contribution from these models comes from $\tilde{G}$, and the momentum of $\tilde{G}$ is forced to be small by the mass degeneracy of the stealth sector. This is easy to see based on the momentum of the invisible particle $\tilde{G}$. Here it is assumed that $\tilde{S}$ has mass $M_{\tilde{S}}$, $\tilde{G}$ is massless and S has mass M_S. In the rest frame of $\tilde{S}$, the magnitude of the momentum p of the daughter particles is equal. Conservation of energy gives,

$$E_{\tilde{S}} = E_{\tilde{G}} + E_S. \tag{2.12}$$

In the rest frame of $\tilde{S}$, this results in:

$$M_{\tilde{S}} = p + \sqrt{p^2 + M_S^2}, \tag{2.13}$$

re-arranging and squaring gives:

$$(M_{\tilde{S}} - p)^2 = p^2 + M_S^2. \tag{2.14}$$

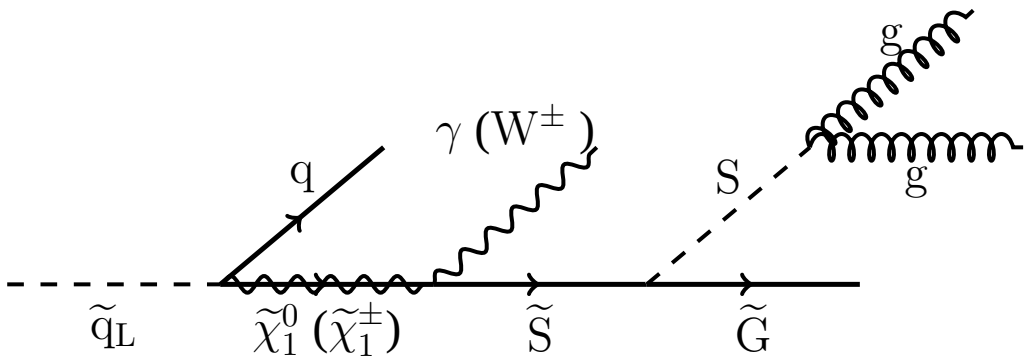

Figure 2.6: Decay of a $\tilde{q}_L$ to a quark and gaugino ($\tilde{\chi}_1^{\pm}$, $\tilde{\chi}_1^0$) in stealth SUSY. Subsequent decay of the gaugino to a singlino produces a vector boson, and the singlino decay yields two gluons and a soft gravitino. The $\tilde{S}$-S mass-splitting is fixed at 10 GeV, and $\tilde{S}$ mass is 100 GeV.

After some algebra, the momentum p can be written as:

$$p = \frac{M_{\tilde{S}}^2 - M_S^2}{2M_{\tilde{S}}}. \tag{2.15}$$

If $\delta M = M_{\tilde{S}} - M_S$, the above expression can be used to determine the limiting case as δM goes to zero. Equation 2.15 can be written as:

$$p = (M_{\tilde{S}} - M_S)\frac{M_{\tilde{S}} + M_S}{2M_{\tilde{S}}} = \delta M \frac{M_{\tilde{S}} + M_S}{2M_{\tilde{S}}} = \delta M \frac{-(M_{\tilde{S}} - M_S) + 2M_{\tilde{S}}}{2M_{\tilde{S}}} \tag{2.16}$$

$$p = \delta M - \frac{(\delta M)^2}{2M_{\tilde{S}}} \xrightarrow{\delta M \ll M_{\tilde{S}}} \delta M. \tag{2.17}$$

Thus, the total momentum p is directly proportional to δM. In the lab frame, the momentum is increased by the Lorentz boost factor γ, and the momentum in the lab frame $p_{\text{lab}} = \gamma \delta M$.

For models of stealth SUSY on the other hand, the lab frame momentum can be made arbitrarily small by δM. In fact, the salient point of stealth models is that SUSY is conserved in the stealth sector, requiring a small δM. This results in a robust mechanism where SUSY particles decay without $\vec{p}_{\text{T}}^{\,\text{miss}}$.

There are a variety of specific stealth SUSY models that describe the interaction between the hidden sector, the SM and the remainder of the SUSY spectrum. In one model, the hidden sector couples to the SM Higgs fields, resulting primarily in the decay $S \to b\bar{b}$ through mixing with the Higgs. In another model, S decays to gluons through a loop involving the messenger field that obeys the transformation laws of the GUT SU(5) group.

Model details

The specific model studied in this thesis is shown in Fig. 2.6, with degenerate first- and-second-generation squark masses $M_{\tilde{q}}$ in the range of 300–900 GeV. The branching fractions $\tilde{\chi}_1^{\pm} \to W, \tilde{S}$ and $\tilde{\chi}_1^0 \to \gamma, \tilde{S}$ were set equal to one. This is motivated by the branching fractions from the MSSM [32, 33], where the neutral bino-like states decay primarily to photons, and the charged states decay to primarily W. These decay chains were searched for separately using final states with photons and leptons. Only the search for final states involving leptons will be discussed in this thesis. Stealth decays can involve b quarks, but the focus of this analysis will be final states without b quarks, and it is assumed that $S \to gg$ as in SU(5) models.

The mass splitting between the chargino with mass $M_{\tilde{\chi}_1^{\pm}}$ and the singlino with mass $M_{\tilde{S}}$ impacts the detection sensitivity in two ways. If $M_{\tilde{\chi}_1^{\pm}} - M_{\tilde{S}} \leq M_W$, then the W is off-shell and it is difficult to reconstruct the leptons coming from its decay. If $M_{\tilde{\chi}_1^{\pm}} - M_{\tilde{S}} \gg M_W$, then the $W - \tilde{S}$ system can be boosted. In this case, the gluons from the singlet decay could be close to the lepton. The efficiency to reconstruct a

lepton in this scenario is decreased, and therefore the detection sensitivity is lower. Since this analysis has not been presented before, we performed the analysis for a set of points where we fixed $M_{\tilde{S}}$ at 100 GeV, and $M_{\tilde{\chi}_1^\pm} = \frac{1}{2} M_{\tilde{q}}$. The singlino-singlet mass splitting is the main feature of stealth SUSY models, and was set to 10 GeV with a massless gravitino. The 10 GeV mass splitting is motivated by the fact that models with mass splitting larger than 20 GeV are excluded by current $E_{\mathrm{T}}^{\mathrm{miss}}$ based searches.

Chapter 3

The LHC and CMS experiment

3.1 The LHC

This Section will discuss the basic operating procedure of the LHC accelerator and the operating parameters at a center-of-mass energy of 8 TeV.

The Large Hadron Collider (LHC) is a 27 km proton-proton collider on the French-Swiss border (Fig. 3.1) designed to study physics at the TeV scale [34, 35, 36]. The particular goals were to discover the Higgs boson predicted by the Standard Model, and perform direct searches for new physics. Table 3.1 lists some machine parameters related to the operation of the LHC.

The LHC accelerates 450 GeV protons from the main injector using superconducting radio frequency (RF) cavities, cycling the beams around the LHC ring at 400 MHz. The beams are controlled by NbTi superconducting dipole magnets with an 8 T magnetic field operated at 1.9 K, and focused using quadrupole magnets. The LHC is constructed in the former LEP tunnel that has a diameter of only 3.7 m. Due to the space constraints and cost, a single cold-mass magnet system with separate

tb

Table 3.1: Summary of some LHC machine parameters.

Circumference (km)	26.7
Beam Current (A)	0.58
Dipole operating temperature (K)	1.9
Peak dipole field (T)	8.33
Energy gain per turn (keV)	485
Beam lifetime 1/e (hr)	15
Injection energy (GeV)	450
Beam pipe pressure [room temperature] (mbar)	10^{-10}-10^{-11}
Residual beam pipe gas density [cryogenic] (molecules/m^3)	10^{15}

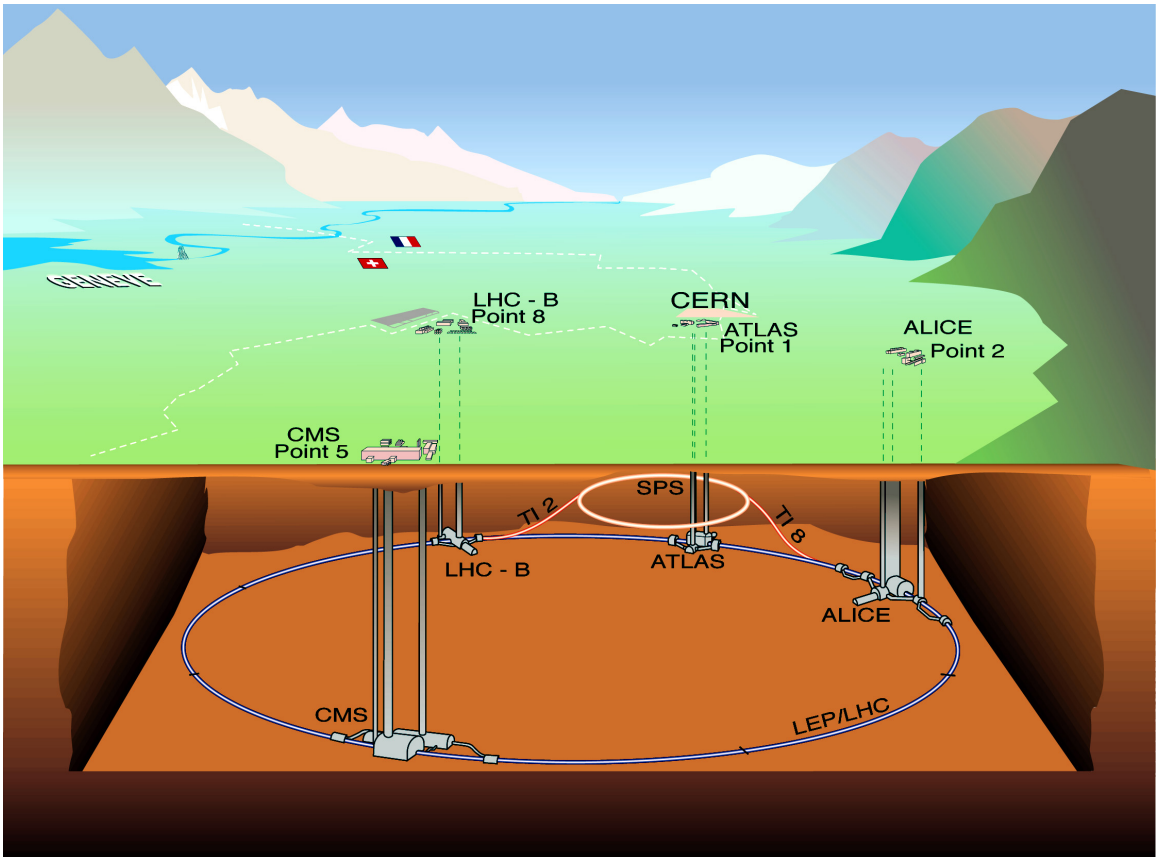

Figure 3.1: Illustration of the LHC, depicting the locations of the experiments.

beam pipes is used.

The LHC has several vacuum systems. The beam pipe requires an excellent vacuum to reduce losses from collisions with residual gas. More moderate vacuum systems are then used for the insulation of the magnet and helium systems. The dominate beam loss mechanism is due to collisions at the interaction points, leading to a beam lifetime of approximately 15 hours.

The primary particle physics consideration when designing a collider is the number of events of a given process which can be produced:

$$N = \sigma \times L = \sigma \times \int \mathcal{L} dt, \tag{3.1}$$

where σ is the process cross section, L the integrated luminosity and $\mathcal{L}$ the instantaneous luminosity. Note, that σ for a given process at a hadron collider is a function of the center-of-mass energy of the proton-proton system, and the parton probability distribution (PDF) of the proton constituents (quarks and gluons), as this will be described in more detail in Section 4.2. The instantaneous luminosity $\mathcal{L}$ is a function

of the machine operating parameters [37]:

$$\mathcal{L} = \frac{N_p^2 n_b \gamma f_{\text{rev}}}{4\pi\varepsilon_n \beta^*} \times F = \frac{N_p^2 n_b f_{\text{rev}}}{4\pi\sigma_x^* \sigma_y^*} \times F \tag{3.2}$$

where,

- N_p - number of protons per bunch
- n_b - number of bunches
- γ - relativistic gamma: $1/\sqrt{1-\beta^2}$ where β=v/c
- f_{rev} - revolution frequency
- ε_n - normalized emittance
- β^* - machine beta function at the interaction point (IP)
- $\sigma_{x,y}$ - width in two dimensions, x and y, perpendicular to the beam direction
- F - the geometric reduction factor for non-zero bunch-crossing angle

The right-hand side of the expression does not contain a factor of γ because the normalized emittance include a factor of γ in the definition. Examination of the right-hand side of Eq. 3.2 shows that $\mathcal{L}$ has units of $[Length]^{-2}[t]^{-1}$ or inverse cross section per unit time. In practice, the LHC normally presents the luminosity in terms of $cm^{-2}s^{-1}$ which results in the luminosity numbers given in Table 3.2.

As highlighted by Table 3.2 and Fig. 3.2, the LHC enjoyed an extremely successful run between 2010–2012. The luminosity delivered by the LHC at the end of 2012 was approaching 300 pb^{-1} per day, and the total integrated luminosity was approximately 23 fb^{-1} for 2012. The data set collected in 2011 at $\sqrt{s} = 7\,\text{TeV}$ resulted in $4.9\,\text{fb}^{-1}$ of integrated luminosity. This thesis will present analyses on both data samples, where

Table 3.2: Summary of LHC parameters for 8 TeV, as well as design parameters.

Parameter	$\sqrt{s}$=8 TeV	design
Beam energy (TeV)	4	7
Peak $\mathcal{L}(cm^{-2}s^{-1})$	7.7×10^{33}	10^{34}
Bunch spacing (ns)	50	25
n_b	1374	2808
N_p	$1.6 - 1.7 \times 10^{11}$	1.15×10^{11}
β^* at IP 1,2,5,8 (m)	0.6, 3.0, 0.6, 3.0,	0.55
ε_n (μm)	2.5	3.75
Beam energy (MJ)	≈ 140	362
f_{ref} (MHz)	400	400

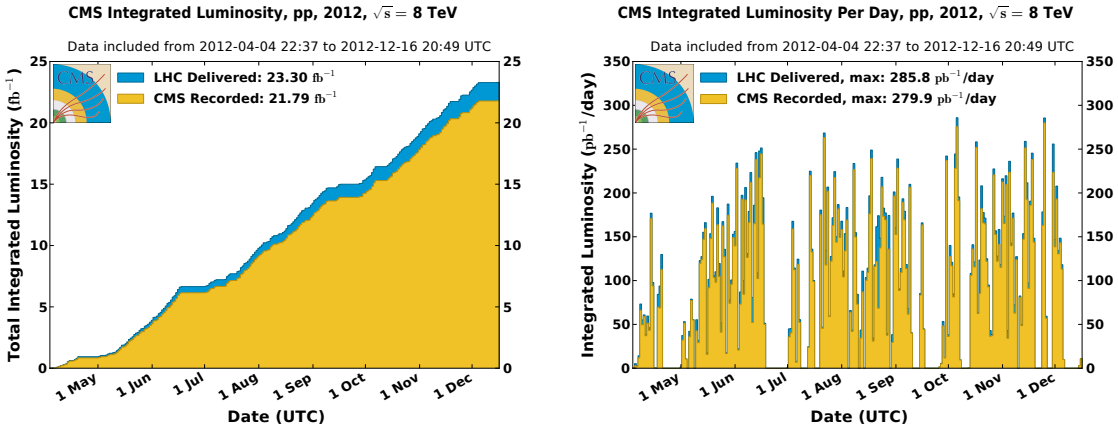

Figure 3.2: Left: plot of the integrated luminosity at the LHC. Right: plot of the integrated luminosity recorded per day. Both plots show the luminosity delivered (blue) by the LHC and recorded (yellow) by the CMS experiment.

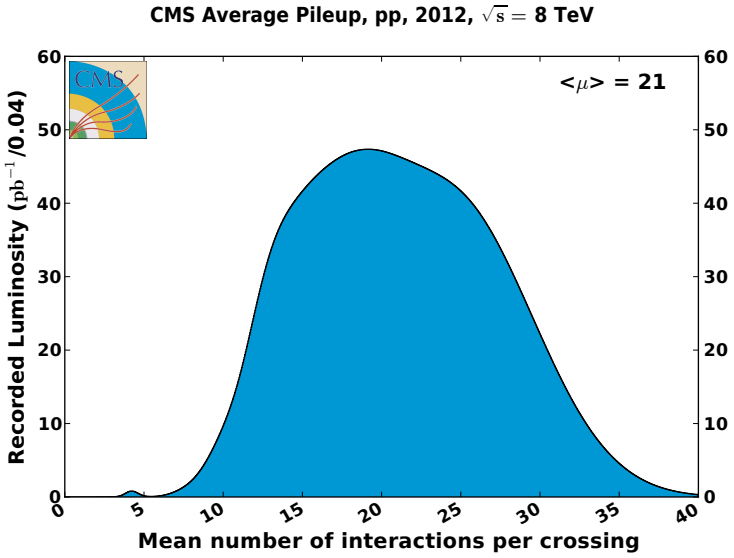

Figure 3.3: Plot of the average number of interactions per beam crossing in the 2012 run of the LHC.

the 2012 data sample was used in the search for stealth supersymmetry and the 2011 sample for the measurements of the Υ cross sections.

The high luminosity of the LHC leads to multiple pp interactions per bunch crossing, which is referred to as pileup. As depicted in Fig. 3.3, the average number of pileup interactions at 8 TeV was around 21. One of the challenges of analyzing the 2012 dataset was understanding the impact of pileup.

3.2 CMS

This Section discusses the goals of the CMS experiment [38, 39, 40], and how they are achieved. The general methods of particle detection and identification outlined, and how this is achieved in CMS. This discussion will start with the magnetic field of CMS and work outward, discussing the charged particle tracking system, both calorimeters, muon identification, and the trigger system.

The goals of the CMS physics program include elucidating electroweak symmetry breaking (Higgs mechanism) and exploring new physics at the TeV scale. To accomplish this at the high luminosities of the LHC requires a high-granularity detector with good muon identification and charged particle momentum resolution (1%), tagging of objects such as b-jets and taus, good energy resolution from the electromagnetic detector (1%) and $\vec{p}_{\mathrm{T}}^{\,\mathrm{miss}}$ resolution, requiring an hermetic detector. The CMS detector was designed with all of these constraints in mind, as shown in Fig. 3.4. It has a diameter of 14.6 m, a length of 21.6 m and weighs 12,500 tons.

3.2.1 The CMS coordinate system

In the CMS coordinate system, the x-axis points towards the center of the LHC, the y-axis points up, and the z-axis along the anti-clockwise beam direction. The azimuthal angle ϕ is measured in the x-y plane, with ϕ=0 along the positive x-axis, and $\phi = \pi/2$ points along the positive y-axis. The polar angle θ is measured from the z-axis, and the pseudorapidity is defined as $\eta = -ln[\tan(\theta/2)]$.

3.2.2 Particle detection overview

To appreciate the physics of the CMS detector, it is useful to first review the main interactions of particles with matter, which are discussed in more detail in [12, 41, 42].

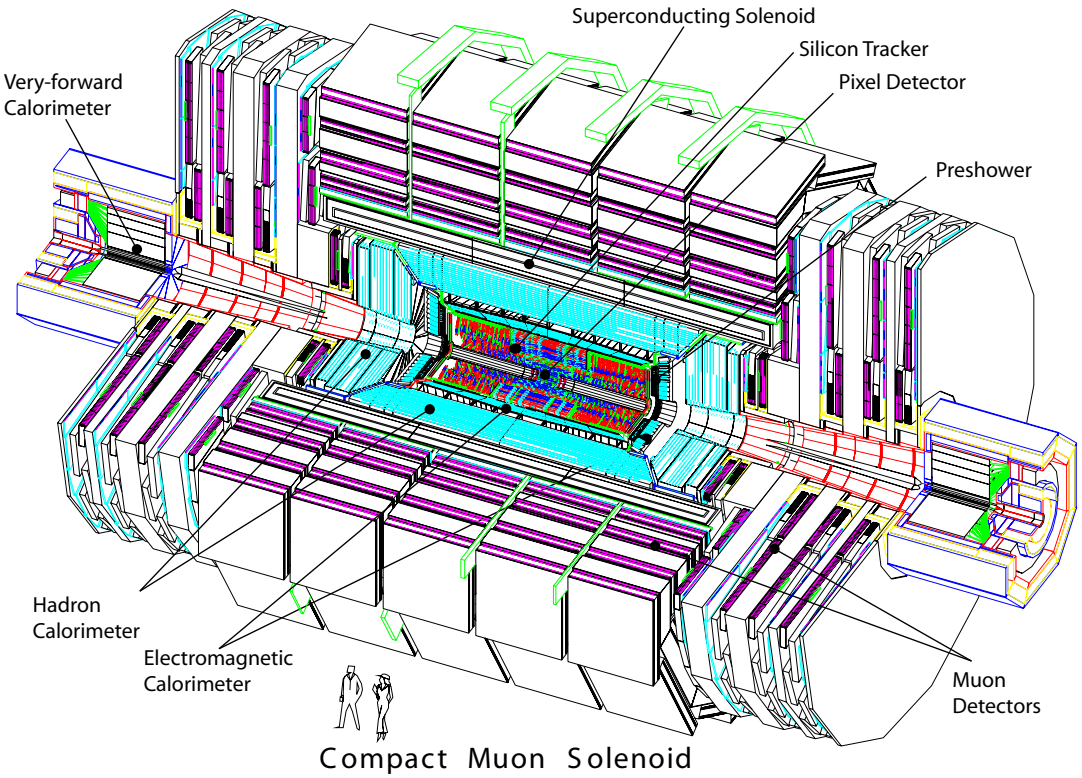

Figure 3.4: Diagram of the CMS detector, showing the overall layout and various subsystems.

The main mechanisms of energy loss are:

- ionization,
- bremsstrahlung,
- pair production,
- multiple scattering,
- hadronic interactions.

For a charged particle at low energy, ionization tends to dominate energy loss. Electrons can also scatter off the nucleus and emit a photon (bremsstrahlung) as depicted in Fig. 3.5. The energy loss from ionization and bremsstrahlung are proportional to $1/m$ and $1/m^2$, respectively, where where m is the mass of the incident particle. Thus, bremsstrahlung tends to dominate the energy loss above an energy of about 10 MeV. On the other hand, for more massive particles, such as muons muons, ionization energy loss can dominate.

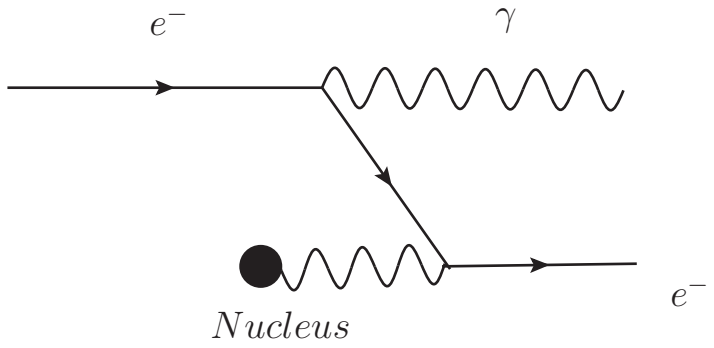

Figure 3.5: Sample diagram for the emission of a bremsstrahlung photon from an electron.

As a charged particle, such as an electron, passes through a material, it tends to lose energy in a shower of particles. The radiation length is the average material thickness needed to reduce the particle energy by a factor of e, on average.

For photons, the main method of energy loss is pair production, where a photon scatters off the nucleus and produces an e^+e^- pair, as depicted in Fig. 3.6. At energies below a few MeV, other mechanisms such as Compton scattering are also relevant.

For hadrons, the strong interaction with protons tends to dominate, for example the inelastic reaction:

$$\pi^- + p \to \pi^+ + \pi^- + \pi^0 + n$$

produces additional pions and a neutron. At very low energy (< 3 GeV), there are a

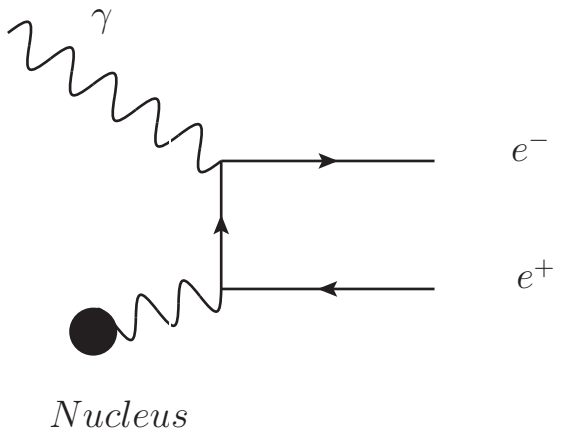

Figure 3.6: Sample diagram for pair production of a photon from the interaction with a nucleus.

number of resonances that can also impact the interaction. For hadrons, the energy loss is dominated by strong interactions, and not electromagnetic processes such as bremsstrahlung. The interaction length is the mean distance a particle travels in a material before interacting with the nucleus. Note that a showering phenomena happens for hadronic interactions as well. This means that a pion incident on a material will tend to produce a spray of additional pions, including neutral pions. Since the lifetime of the neutral pion is very short, it decays immediately to photons.

Multiple scattering is the combined impact of many small-angle scattering events of a particle as it travels through a medium. The distribution of deflections is gaussian for small angles, with a non-gaussian tail for large angles.

3.2.3 Magnetic field

The 3.8 T magnetic field [43, 44] is produced by a superconducting solenoid, which provides excellent momentum resolution for charged particles. Some of the key physical quantities are summarized in Table 3.3. The distinguishing feature of the CMS solenoid is the large magnetic energy density ratio, shown in Fig. 3.7. The innovative part of the CMS magnet is that it obtains a large energy-to-mass ratio by being primarily self-supporting.

The solenoid is encapsulated with a return yoke made of structural steel. This makes the magnetic field more homogeneous, and returns the stray magnetic flux to the solenoid. In addition, the steel provides an absorber for muon identification.

A precise knowledge of the magnetic field is important for reconstruction and simulation, which is described in detail in Ref. [45]. The magnetic field was simulated using finite-element analysis (FEA) [46], and is depicted in Fig. 3.8. To determine the validity of FEA, the magnetic field was directly measured in the tracker volume using

Table 3.3: Summary of some general features of the CMS magnet.

Magnetic field	
Diameter (m)	6
Length (m)	12.5
Mass of return yoke (kilotons)	10
Cold mass (tons)	220
Conducting material	NbTi
Operating temperature (K)	4
Stored energy (GJ)	2.6
Stored energy per cold mass (kJ/kg)	11.6
Current (kA)	19
Maximum design field (T)	4
CMS operating field (T)	3.8
Absorber lengths (X_o)	3.9

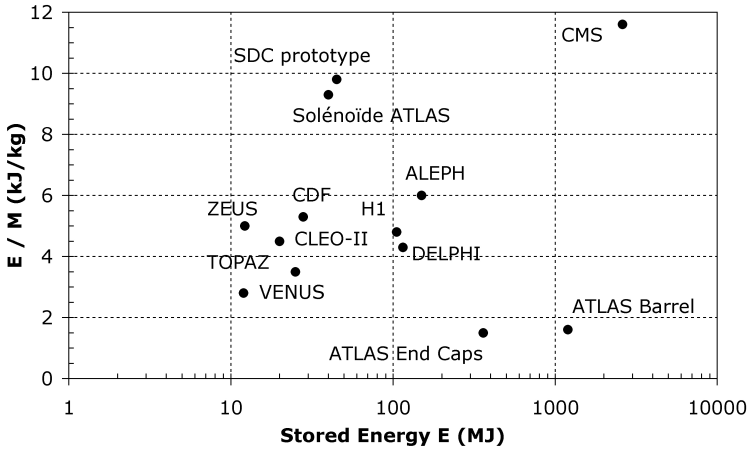

Figure 3.7: Ratio of stored energy to mass (E/M) for a variety of detector superconducting magnets Credit: [38].

nuclear magnetic resonance (NMR) probes that provide a very accurate measurement of the magnetic field. To determine the field in the return yoke, cosmic ray tracks are propagated from the tracker volume to the muon stations. By comparing the deflection in ϕ projected from the tracks and the ϕ measured in the muon chambers, the difference between the mapped and true field can be determined.

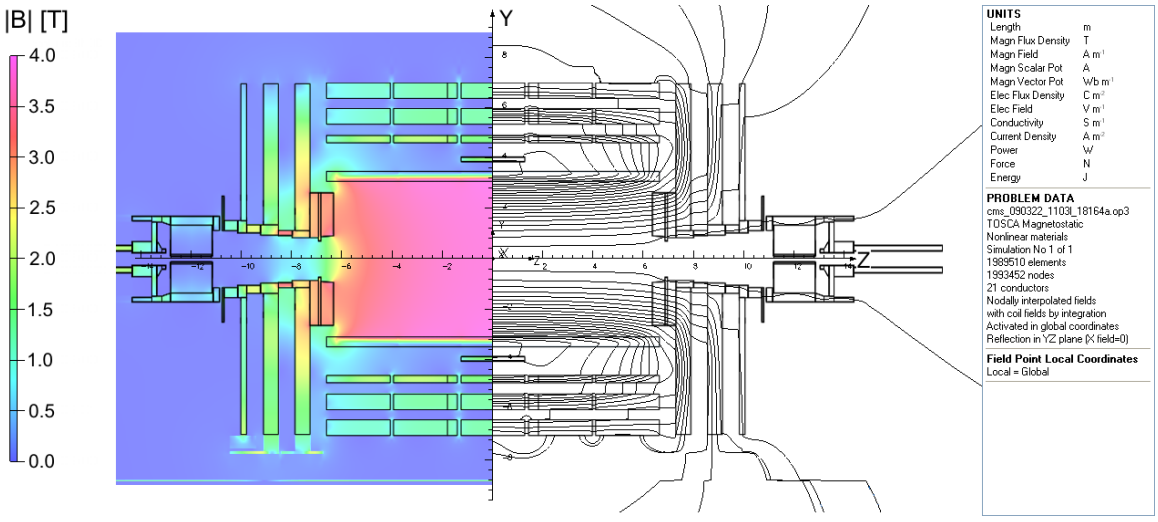

Figure 3.8: CMS magnetic field, modeled with TOSCA. The left-hand (colored) portion shows the magnitude of the magnetic field, and the right-hand side shows the flux density at 3.8 T, where each line represents a flux increment of 6 Wb. Credit: [45].

3.2.4 The silicon tracker

To keep the detector occupancy near the interaction point low requires a high granularity detector. To give some idea of the challenge, 8 TeV collisions during data collection in 2011-2012 (Run 1) saw approximately 20 interactions and 1000 particles produced per bunch crossing. The CMS tracker uses pixels and strip silicon sensors to measure the charged track momentum and the position of primary and secondary vertices. Some key features of the tracking system are outlined in Table 3.4.

The tracking system utilizes silicon sensors. The operating principle of silicon sensors is to reverse bias a pn junction; as a charged particle traverses the silicon, it creates electron-hole pairs. The electric field then causes the electron-hole pairs to

Table 3.4: Summary of some general features of the silicon tracker.

Tracker	
Pixels modules (number of pixels, million)	1440 (66)
Strip modules (number strips, million)	15148 (9.3)
Power consumption (kW)	60
Operating temperature (C)	-25
Radiation lengths (X/Xo)	0.5-1.8
Active silicon (m^2)	200
Momentum resolution [p_T, η dependent] (%)	0.8-7

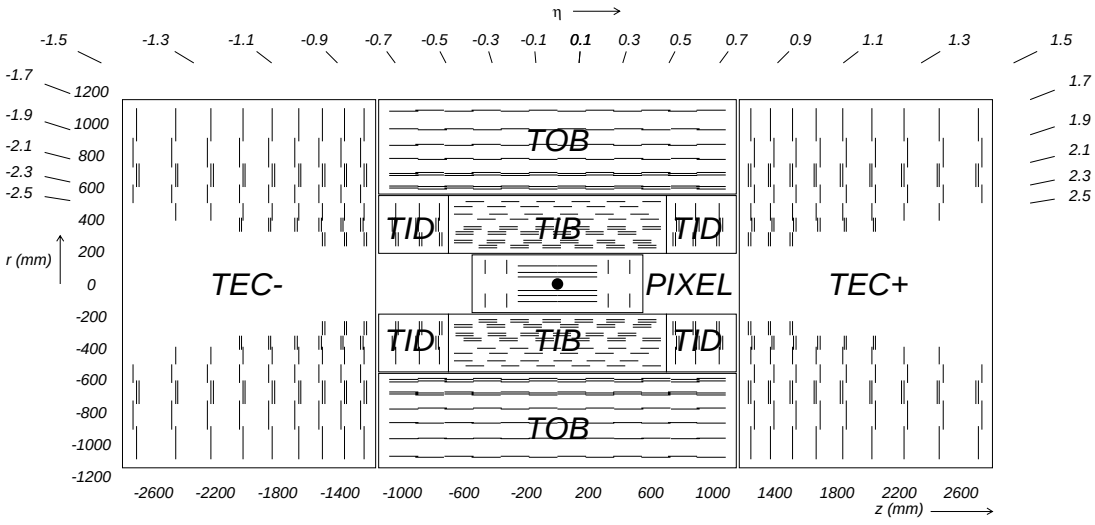

Figure 3.9: The layout of the tracker showing the main detector regions. TIB(TID) are the tracker inner barrel (disks). TOB is the tracker outer barrel, TEC+(-) are the tracker endcaps for +(-) z. Credit: [38].

travel to opposite sides of the sensor where accumulated charges are read-out. CMS uses n-doped silicon, with an n+ strip.

As depicted in Fig. 3.9 the tracking system consists of an inner pixel system made up of 100×150 μm silicon sensors, and extends to a radius r of 10 cm. As the distance from the interaction point increases, the occupancy decreases, and silicon strips are used for 10 cm $< r <$ 100 cm.

For a charged particle in a magnetic field, the momentum is related to the radius of curvature by [47]:

$$p_{\mathrm{T}} = qBR \tag{3.3}$$

$$p_{\mathrm{T}}(MeV/c) = 300(T \cdot m)BR \tag{3.4}$$

where R is the radius of curvature, and B the magnetic field. A series of track hits with precise r, ϕ, z coordinates can then be reconstructed into a track with known momentum given the magnetic field map [48, 49] and material budget.

The material budget of the tracker volume was measured using photon and nuclear conversion in the tracker material [50]. Soft-photon conversion to e^+e^- can occur in the material of the silicon tracker. These electrons can then be reconstructed as a secondary vertex. The distribution of these secondary vertices allows a material map to be developed and compared with the expected material distribution. A plot of these conversion vertices is depicted in Fig. 3.10, where the outline of the silicon tracker can clearly be seen. The track momentum scale and resolution were measured using cosmic rays at high momentum and decays from resonances such as the J/ψ at low momentum [51].

3.2.5 Electromagnetic calorimeter

One of the pillars of the CMS experiment is an excellent electromagnetic calorimeter (ECAL) to allow for studies of the Higgs decay to two photons. Some of the key features of ECAL are summarized in Table 3.5.

Table 3.5: Summary of some general features of the ECAL.

ECAL	
Crystal material	$PbWO_4$
Number of crystals: barrel	61200
Number of crystals: endcap	7324
Crystal cross section ($\eta - \phi$)	0.0174×0.0174
Crystal length (mm, Xo)	230, 25.8
Scintillation time (ns)	25
Mass (tons)	67
Operating temperature (°C)	18

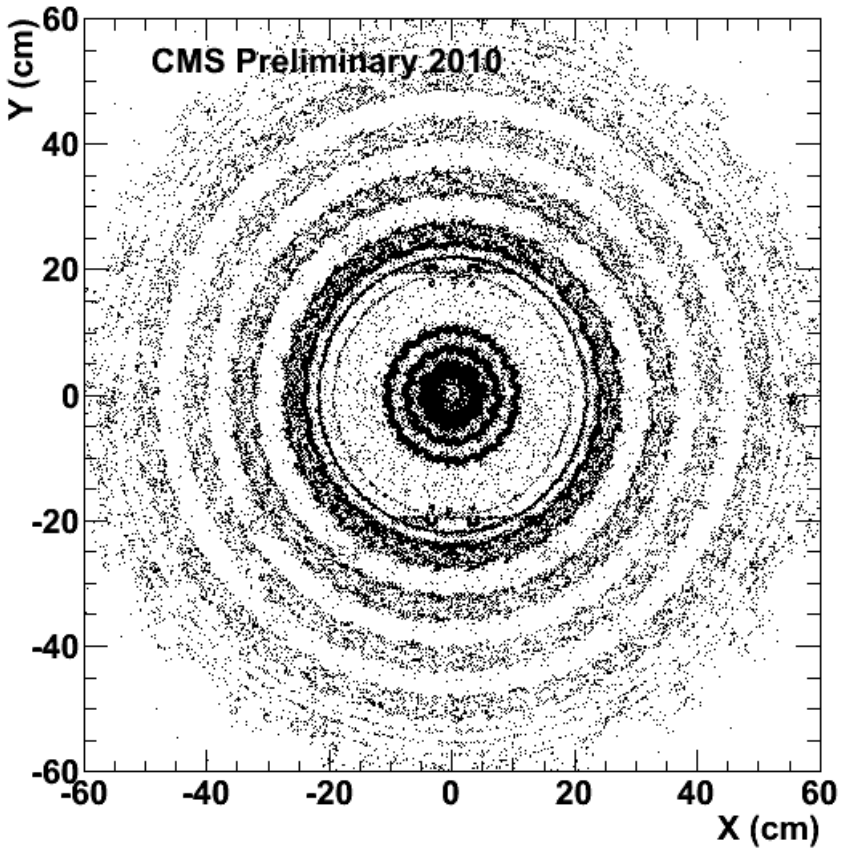

Figure 3.10: Conversion vertices in the x-y plane showing the layout of the silicon tracker, see Ref. [50].

The ECAL consists of 75,000 $PbWO_4$ crystals arranged to cover $|\eta| < 1.479$ (barrel) and $1.479 < |\eta| < 3.0$ (endcaps). The crystals emit 4.5 photoelectrons/MeV, which are collected by avalanche photodiodes (APDs) in the barrel region and VPTs (vacuum phototriodes) in the endcaps. The response of the crystals depends on the temperature. The ECAL is cooled to 18 °C using a water cooling system. The preshower detector covers $1.653 < |\eta| < 2.6$, and initiates showers in the endcap. It consists of two layers of lead absorbers and two layers of silicon strip detectors.

The transparency of the ECAL crystals changes rapidly with radiation dose. To account for this, the transparency of the crystals is measured and corrected for using a laser calibration system.

The resolution of calorimeters is parameterized as a simple function described below.

$$\left(\frac{\sigma}{E}\right)^2 = \left(\frac{S}{\sqrt{E}}\right)^2 + \left(\frac{N}{E}\right)^2 + C^2 \tag{3.5}$$

where S is the stochastic term, N is the noise term, and C the constant term. In ECAL, S has to do with effects such as fluctuations in the shape of the shower and photostatistics. The constant term is related to how the crystals are calibrated, and the uniformity of light collection. The noise is impacted by electronics and digitization, as well as pileup.

Test beam measurements of an ECAL prototype resulted in: $S = 2.8\%$, $N = 12\%$, and $C = 0.30\%$. Additional calibrations were performed using a variety of techniques in data, such as the reconstruction of the $\pi^0 \to \gamma\gamma$ peak [52].

For the reconstruction of photons and electrons, basic clusters are formed by combining crystals together; this starts with a seed crystal, which has some minimum energy. Then adjacent crystals are added to the cluster if they contain an energy deposit, are not already assigned to a cluster and if the energy is lower than the previous crystal. Super clusters are made in a similar way, except that instead of combining crystals, super clusters are built from basic clusters. [53]. Photons are reconstructed from the super clusters, using requirements on a variety shower variables [54]. Electron reconstruction matches ECAL clusters with tracks using super clusters in the ECAL as a seed to reconstruct the track [55, 56, 57].

3.2.6 Hadronic calorimeter

The hadron calorimeter is depicted in Fig. 3.11 and consists of layers of brass absorbers and plastic scintillators. Hadrons are detected by showers of pions that result when a hadron collides with the absorber material. The showering eventually produces π^0s, which decay to photons and are detected.

The calorimeter is subdivided into the: hadron barrel (HB), endcap (HE), outer (HO) and forward (HF) calorimeters. The HB is the first layer after the ECAL barrel

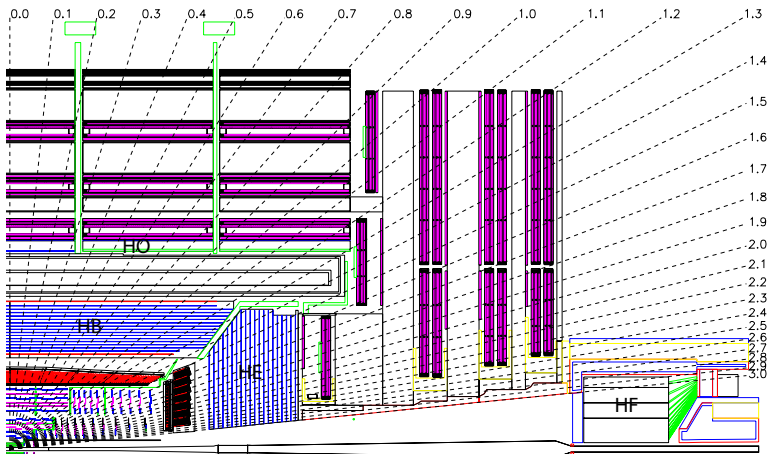

Figure 3.11: Cross Section of the HCAL detector: hadron barrel (HB), endcap (HE), outer (HO) and forward (HF) calorimeters. Credit: Ref [38]

inside the magnetic field. It consists of a wedge of absorber-scintillator material, with granularity in $(\Delta\phi, \Delta\eta)$ cells of (0.087,0.087). The light from the scintillator material is collected by wavelength-shifting fibers, and read out by hybrid photodiodes (HPDs). HB consists of 5.8-10 interactions lengths of material and covers $|\eta| < 1.3$. HE covers $1.3 < |\eta| < 3.0$, has 10 interaction lengths, and (0.087,0.087) cells. The HF covers $3.0 < |\eta| < 5.0$, which on average collects 760 GeV per collision, compared to only 100 GeV for the rest of the detector. It is also used for a real-time measurement of the luminosity.

3.2.7 Muon detectors

The muon system is also a key feature of the CMS program, motivated by low-background physics signatures, such as $H \to ZZ^* \to \mu^+\mu^-\mu^+\mu^-$. The muon system consists of three gaseous detectors: drift tubes (DT), resistive plate chambers (RPC), and cathode strips chambers (CSC).

Table 3.6 outlines some of the key features of the muon system. The details of the detectors are slightly different but the guiding principle for all three subsystems is that a muon ionizes the gas, resulting in a measurable current. The DT consist of positively charged wires in gas tubes. When a muon ionizes the gas, the electric field causes a current to be read on the wire. The geometry of the CSC consist of positively charged wires, with strips at ground running perpendicularly. The RPC consist of two parallel plates separated by a region filled with gas, which creates an

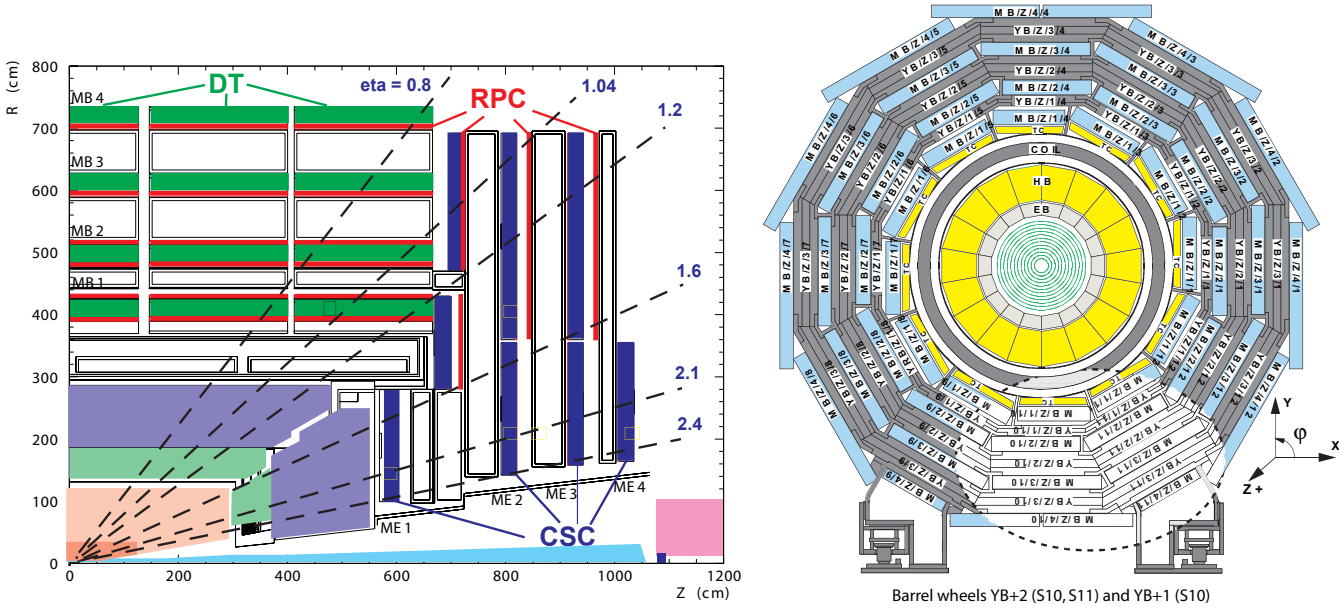

Figure 3.12: Left: projection of muon system components in the r-z plane, showing the DT, RPC and CSC detectors. Right: transverse projection of the muon system.

Table 3.6: Summary of some general features of the CMS muon detector.

DT	
$\|\eta\|$	0–0.8
Area (m^2)	2500
Sensitive wires	172,000
Gas	Ar(85%)/CO_2 (15%)
CSC	
$\|\eta\|$	0.9–2.4
Area (m^2)	5000
Sensitive wires	2 million
Gas	Ar(40%)/CO_2 (50%)/CF_4 (10%)
RPC	
$\|\eta\|$	0–1.6
Number of strips	80,640
Area (m^2)	2400
Gas	R134a (96.2%,$C_2H_2F_4$)/C_4H_{10}(3.5%)/ SF_6(0.3%)

avalanche of electrons when a charged particle goes through it. The current is read by external sensors.

The combination of the tracking and muon systems allows for excellent momentum resolution for muon p_{T} from 10 GeV to 1 TeV [58]. The resolution from an algorithm that combines both systems is shown in Fig. 3.13.

The muon system must be aligned at the level of 100 μm. Misalignment can come from gravitational forces on the return yoke, stresses from the solenoid field, and thermal instabilities. The position is monitored using LEDs and laser light with

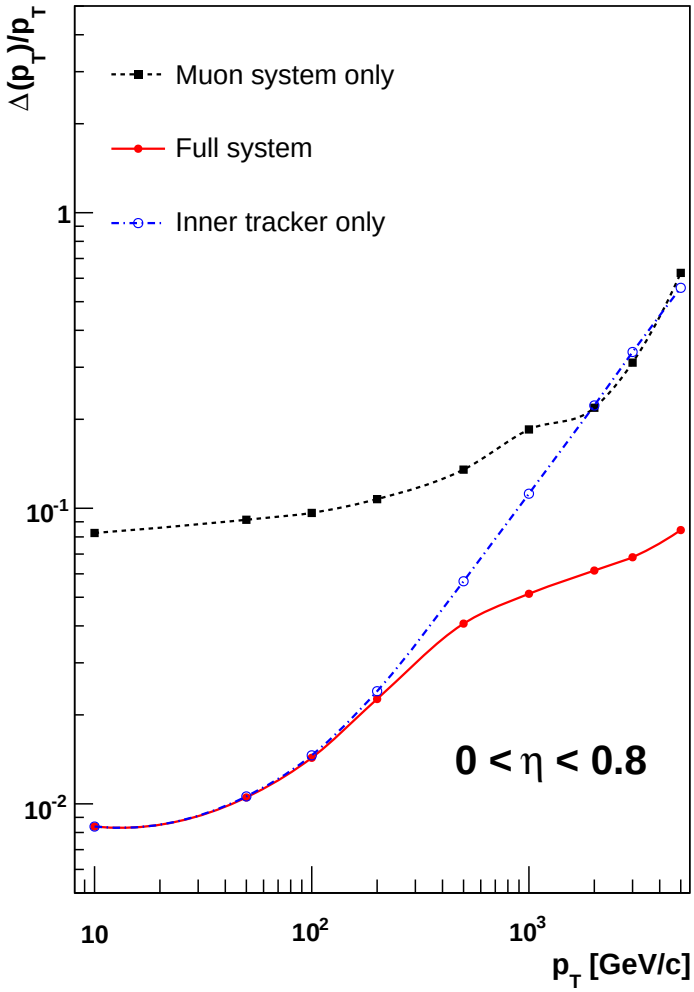

Figure 3.13: Muon resolution in the barrel using only the muon system, a combined reconstruction involving both the tracking and muon systems, and only the tracking system.

photodetectors.

3.2.8 Data acquisition and trigger

The collision rate during Run 1 was 40 MHz. Since it is not practical to store every event, a trigger system is needed to reduce the rate by a factor of 10^6, yielding a more manageable 400 Hz of events to be written to tape.

The challenge of the trigger system is to reduce the rate and simultaneously save interesting events at as high an efficiency as possible. Table 3.7 outlines the number of events expected for a few major processes. The challenge is obvious from the fact that the expected background from QCD is orders of magnitude above the expected number of events expected for a new physics process such as top squark pair production $\tilde{t}\,\tilde{t}$.

Table 3.7: The number of expected events per second and year assuming 20 fb^{-1} is collected in one year at $\sqrt{s} = 8$ TeV for a few SM processes. The number of events expected does not include p_{T} thresholds on muons or jets.

Process	Events/s	Events/yr
QCD	10^7	10^{15}
W$\rightarrow \mu\nu$	2	10^8
Z$\rightarrow \mu\mu$	0.2	10^6
$t\bar{t}$	0.2	10^6
$\tilde{t}\,\tilde{t}$ (300 GeV)	10^{-3}	10^4

To select physics processes of interest while rejecting background events, the CMS trigger system must be capable of making sophisticated and fast decisions. This goal is accomplished in the CMS trigger in a two-stage system: a level-one (L1) hardware trigger [59], and a high-level trigger (HLT) [60] implemented on a computing farm. It is worth noting that this is a unique trigger design in that it only has two tiers. Such a setup was enabled by rapid advances in the speed of network switching technology.

The L1 trigger hierarchy starts with local trigger primitive generators (TPG). Trigger objects (e.g., muons) are then passed from the TPGs to regional trigger systems where the objects are ranked according to transverse energy, momentum, and quality information such as hit patterns in the muon chambers. The results of the regional triggers are assessed by the global trigger system to determine whether to accept the event. This is depicted in a schematic of the L1 trigger in Fig. 3.14. The latency of the L1 trigger is 3.2 μs. After this time interval, a trigger decision must be sent to the detector front-end electronics.

Given a L1 accept, the data acquisition system (DAQ) reads data from the detector front end, builds the events from fragments in the builder unit (BU), then passes the data through an event filter (FU) that performs the HLT trigger decision [61] as depicted in Fig. 3.15.

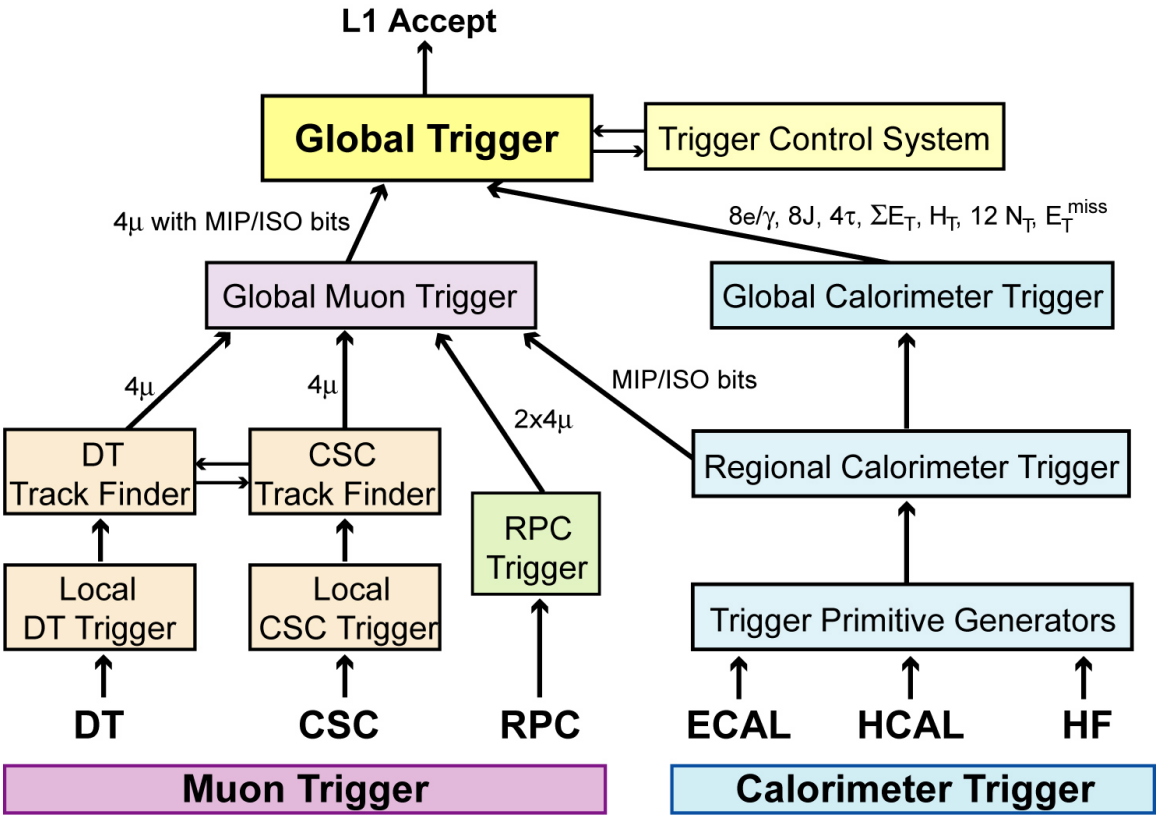

Figure 3.14: L1 trigger architecture.

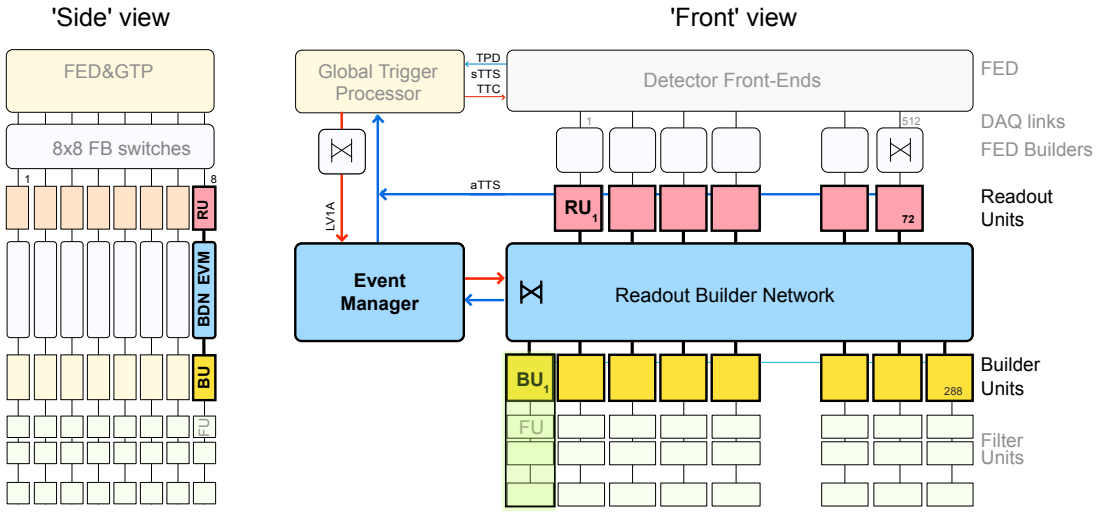

Figure 3.15: Readout builder slice.

The DAQ system must be capable of handling the rate from the L1 trigger (100 kHz), which results in a data flow of $\approx$ 650 Gb/s from 650 different sources. Event filtering in the HLT is performed on a farm of approximately 13,000 cores (updated in 2012) and allows for a processing time of 150 ms/event given a L1 rate of 100 kHz [62]. Based on the L1 trigger, the HLT selection performs a coarse reconstruction of the event, including calorimeter information, the muon and tracking systems. Objects such as muons, electrons, and jets are reconstructed, and kinematic variables such as missing transverse energy are all used at the HLT level to perform a final trigger decision. The limitation of the rate of data from the CMS detector is the rate that can be recorded and reconstructed. Event sizes are typically around 1 Mb, and the rate of data written for storage corresponds to a data rate of about 100 Mb/s. To avoid this constraint, during Run 1, a set of less stringent triggers were also archived for later reconstruction (data parking) [63]. For hadronic triggers (e.g., 2 jets with a total p_{T} of 200 GeV), where the rate was too high to record, data scouting was also implemented, where only the HLT information rather than the full event was recorded. These types of triggers are useful for searching for low-mass states that decay to dijets, for example [64].

Chapter 4

Search for supersymmetry

4.1 Introduction to SUSY searches

As described in Section 2.2, SUSY is a well motivated theory often searched for using $\vec{p}_{\mathrm{T}}^{\,\mathrm{miss}}$, although there are particularly interesting models with low $\vec{p}_{\mathrm{T}}^{\,\mathrm{miss}}$, including stealth SUSY. This chapter will describe the search for stealth SUSY implemented by CMS and is organized as follows. Section 4.2 explains the Monte Carlo (MC) simulation procedures used at a hadron collider, and for this analysis in particular. Section 4.3 describes the "object" reconstruction, such as muons and jets, and Section 4.4 the data samples and trigger. In Section 4.6, details of the background estimation procedures are given, and in Section 4.7 the systematic uncertainties are outlined. The results are shown and interpreted in Section 4.8.

4.2 Monte Carlo simulation

The general strategy for simulation of proton-proton (pp) collisions is to factorize the problem into several pieces dependent on the momentum transfer Q^2. Domains with $Q \gg \Lambda_{QCD}$, where $\Lambda_{QCD} \approx 200$ MeV, are considered to be the "hard scattering" portion of the process and can be calculated at a fixed order in perturbation theory, typically using a matrix element (ME) generator to evaluate all the allowed Feynman diagrams. Two sample diagrams associated with the process pp$\rightarrow$ Z j, Z$\rightarrow \ell^+\ell^-$ are depicted in Fig. 4.1.

This hard scatter can be thought of as the interaction of two partons i and j that produce a third parton k according to the expression:

$$\sigma_{ij\rightarrow k} = \int dx_1 \int dx_2 f_i^1(x_1, Q^2) f_j^2(x_2, Q^2) \hat{\sigma}_{ij\rightarrow k}, \tag{4.1}$$

where $\hat{\sigma}_{ij\rightarrow k}$ is the parton-level cross section and $f_i(x, Q^2)$ is the parton distribution function (PDF) of each parton i inside the proton. The PDF is function of the

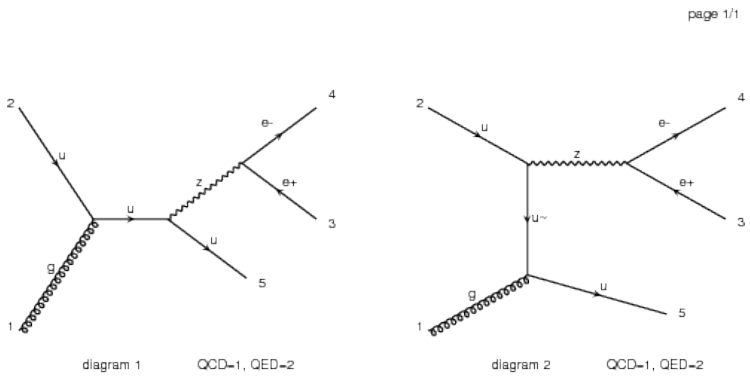

Figure 4.1: Two sample diagrams produced by MadGraph for the process pp$\rightarrow$ Z j, Z$\rightarrow \ell^+\ell^-$.

momentum fraction x and the Q^2. Sample PDFs for quarks and gluons in the proton are shown in Fig. 4.2. The QCD evolution equations [66, 67, 68] allow quarks and gluons generated from the hard scatter to radiate additional quarks and gluons. This process of "parton showering" (PS) contains logarithmically divergent terms if the radiated partons are soft or collinear with the initial parton. The KLN theorem [69, 70] guarantees that in the calculation of the inclusive cross section, large logarithmic terms that arise from soft or collinear radiation are cancelled with virtual corrections order by order in perturbation theory. Thus, PS effects can be approximated as a product of probabilities, rather than amplitudes. Because each step in the PS is independent of previous steps, this allows for the use of a MC algorithm for the showering, as first introduced in Ref. [71]. In such procedures, the final-state partons are allowed to produce additional radiation according to probability distributions depending on the parton species and momenta. This procedure is iterated until there is no further splitting of the final-state partons. Since partons are colored, the simulation requires that each step keeps track of the color information so that the resultant collection of partons has the correct connections between partons to form color-neutral objects.

The PS portion of the simulation only applies in the limit of soft or collinear particles, while the ME generators only apply to energetic or well separated particles. To give smooth distributions and not double count contributions to the total cross section, a full simulation typically merges the two approaches by using a "matching"

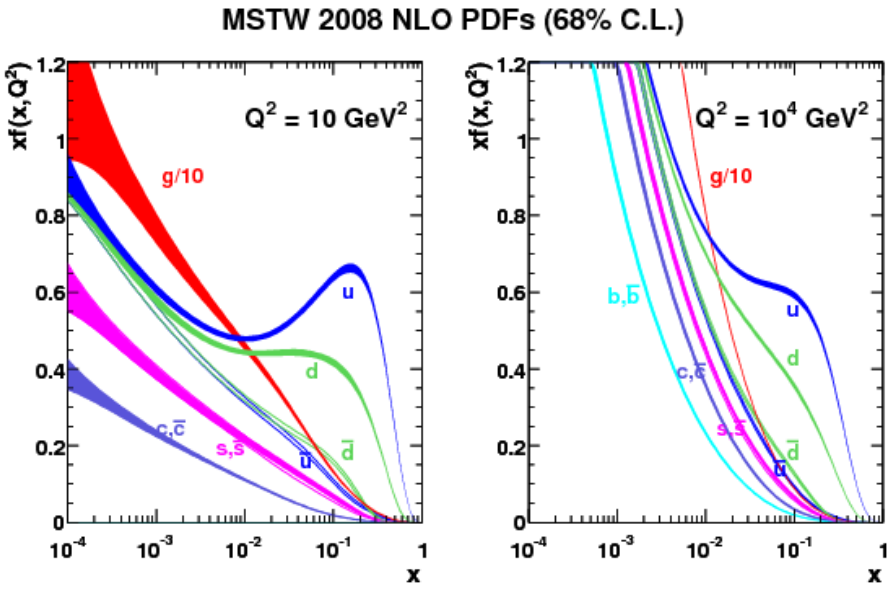

Figure 4.2: The MSTW PDF set [65] for $Q^2 = 10$ GeV^2 (left) and $Q^2 = 10^4$ GeV^2 (right).

algorithm. In this procedure, jets (see next Section) are clustered from the partons after the PS. Jets with p_{T} above a matching scale Q_{cut} are then compared with the initial set of partons. If all of the partons are not matched with a jet, the event is rejected [72, 73, 74].

The process of "hadronization" transforms the colored partons after the PS into color-neutral, bound-state hadrons. There are two physical pictures typically used to describe hadronization: the "string model" [75, 76] and the "cluster model" [77, 78, 79, 80]. In the string model, quarks are thought of as bound by a linear potential $V(r) = \kappa r$. This can be thought of as a "string" connecting two quarks. As the quarks move apart, the potential increases and can eventually produce an additional pair of quarks, so that $q\bar{q} \rightarrow q\bar{q}' + q'\bar{q}$. In the analogy, the string breaks forming two separate strings. In the cluster model, any gluons in the final state after PS are forced to decay to $q\bar{q}$, and these pairs are subsequently decayed to hadrons. Models of hadronization always include adjustable parameters that can be determined from data.

In addition to the hard process and the ensuing radiation, there are low-p_{T} effects such as elastic pp scattering and additional interactions occurring inside the proton, which are called the "underlying event" (UE). The UE includes multiple parton-parton interactions (MPI) in a given pp collision [81, 82]. Though the particles produced from MPI tend to be too soft to make a significant impact on observables such as jets, there can be an impact on the color flow of the event.

A simulation of the CMS detector is then applied to all the stable and quasi-stable particles produced the procedure described above. The most sophisticated detector simulation, GEANT4 [83], allows for a full description of the detector geometry and material. This includes the effects of electromagnetic and hadronic interactions of particles with the detector over a wide range of energies (see Section 3.2.2). An alternative fast simulation [84, 85] reduces the run time by approximately a factor of 100. This simulates the same interactions as the full simulation, but using simplified detector layouts and reconstruction. The silicon tracker is modeled using cylinders rather than the actual geometry, and the simulated hits fit using a simplified method (see Section 4.3 for a discussion of the full track fit). The calorimeters are assumed to be solid, and the shower evolution simulated using a parameterization. Results of this simulation were found to describe early data relatively well.

For this analysis, the SM backgrounds $t\bar{t}$, Drell-Yan (DY), WW, WZ and ZZ were simulated using the leading-order (LO) ME event generator MADGRAPH [86] with the CTEQ6M PDF set [87]. Single top quark backgrounds were simulated at NLO using the POWHEG [88] event generator and the CTEQ6M PDF set. Additional partons were simulated in addition to the primary process, as limited by the speed of generating the events. For $t\bar{t}$ three additional partons were generated, four for DY, and two for diboson samples. MADGRAPH uses matching scheme where jets must have a p_{T} greater than Q_{cut} to be considered. For $t\bar{t}$, $Q_{cut} = 20$ GeV, and all other backgrounds must have a Q_{cut} value of 10 GeV. The renormalization Q^2 scale

for $t\bar{t}$ events was set by the event value of $M_t^2 + \sum p_T^2(\text{jet})$ where M_t is the mass of the top quark fixed at 172.5 GeV. An estimate of the impact of the arbitrary Q choice was obtained by varying the scale Q by a factor of 1/2(2). The hard scatter was then passed to Pythia 6.426 with parameters based on measurements from early LHC data [89] to simulate the PS, hadronization, and the UE, including MPI [89]. Each event is superimposed with a simulated set of "minimum bias" events (such as elastic pp scattering) to reproduce the effect of pileup. The cross sections used to normalize the background MC simulations are listed in Table 4.1.

Samples of stealth SUSY events are generated with values of $M_{\tilde{q}} = 300$–$900\,\text{GeV}$ in steps of 100 GeV. The masses of the other particles in the decay chain are stated in Section 2.3.4. The events are generated using the same version of Pythia and processed with a fast simulation of the CMS detector [84, 85].

Typical cross sections for strongly produced SUSY particles are listed in Table 4.2. These include cross sections for gluino $\tilde{g}$, squark $\tilde{q}$ and top squark $\tilde{t}$ production. These cross sections are computed at next-to-leading-order (NLO) accuracy and include soft-gluon emission at next-to-leading-logarithm (NLL) accuracy [94, 95, 96, 97]. The uncertainties are typically 15–25% and include the impact of varying the renormalization scale and PDF set [98].

4.3 Object reconstruction

Physics objects used for analysis include: muons, electrons, photons, charged hadrons, neutral hadrons, and jets reconstructed from the collection of reconstructed particles. Excellent momentum resolution can be obtained for charged particles using the silicon tracker. The track reconstruction method uses an iterative procedure that is an

Table 4.1: List of cross sections for each underlying process computed at NNLO or NLO. The cross section listed for $Z\to \ell\ell$ includes the branching fraction to all three lepton flavors.

Process	σ (pb)	Calculation
$Z\to \ell\ell$	3504	NNLO [90]
$t\bar{t}$	245.8	NNLO [91]
Single t($\bar{t}$) quark, tW channel	11.1	NLO [92]
Single $\bar{t}$ quark, t-channel	30.7	NLO
Single t quark, t-channel	56.4	NLO
Single $\bar{t}$ quark, s-channel	1.76	NLO
Single t quark, s-channel	3.79	NLO
WW	56.0	NLO [93]
WZ	33.6	NLO (M($\ell\ell$)$>$ 12 GeV)
ZZ	17	NLO (M($\ell\ell$)$>$ 12 GeV)

Table 4.2: Typical cross sections in pb for pair production of gluinos ($\tilde{g}$), squarks ($\tilde{q}$) and top (bottom) squarks, where the $\tilde{t}$ and $\tilde{b}$ squarks are degenerate. For the gluino cross sections, the squarks are decoupled. For the squark entry, gluinos and top squarks are decoupled. For the top squark entry, gluinos and the light-flavor squarks are decoupled. The mass given in each row is the mass of the gluino, squark or top (bottom) squark.

	σ (pb)		
M (GeV)	$\tilde{g}\tilde{g}$	$\tilde{q}\tilde{q}$	$\tilde{t}\tilde{t}$
200	1010	183	18
500	4.5	0.9	0.09
1000	0.02	0.004	0.0004

adaptation of the Kalman filter [99]. First, track finding associates hits in the silicon tracker detector with a track. This is based on a seed of at least three hits, or two hits and an additional constraint based on pp collision point. The track is then extrapolated outward based on the charged particle trajectory to each through each layer of the detector, and the four-momentum of the track is updated based on the surrounding hits. The extrapolation ends when there are no compatible hits or the track reaches the outer layer of the detector. Finally, a fit of the hit associated with the tracks is performed to determine the track four-momentum.

The primary vertex of the event is determined using an adaptive vertex fitting (AVF) [100] algorithm. A collection of vertices is reconstructed from all tracks compatible with the pp collision point, then the PV is defined as the vertex with the highest sum of p_{T}^2 from the tracks contributing to that vertex. The "impact parameter" of a track is the distance of closest approach between the track and the PV along each of the three directions.

The particle flow (PF) algorithm combines information from all subdetectors to reconstruct objects. First, the track reconstruction is run, as described above. In addition, clusters based on energy deposits are formed for each calorimeter subdetector. Then each track is extrapolated to its predicted position at each subdetector in order to search for "links" between tracks and clusters. A similar linking is performed between the ECAL and HCAL clusters, and between tracks and the muon chamber hits. These links serve as a way to distinguish between particle types, and produce a list of particles (i.e., electrons, muons, taus, charged hadrons, and neutral hadrons) similar to a general-level particle collection.

The four-momentum of quarks and gluons can be reconstructed from the particles produced by the PS and hadronization using jet clustering algorithms [101, 102, 103, 104]. For each pair of particles (or jets) i, j in the event, the quantity:

$$d_{ij} = \min[p_{\mathrm{T}}(i)^{2p}, p_{\mathrm{T}}(j)^{2p}][(y(i) - y(j))^{2p} + (\phi(i) - \phi(j))^{2p}]/R^2 \tag{4.2}$$

is computed, where y is the rapidity, ϕ the azimuthal angle, p a power parameter, and R typically has a value of 0.5. Each d_{ij} is compared with the particle p_{T} relative to the beam:

$$d_{iB} = p_{\mathrm{T}}(i)^{2p}. \tag{4.3}$$

Clustering then proceeds by combining the energy and momenta of i and j if d_{ij} is less than d_{iB}, and if not, i is removed from the collection and called a jet. For values with $p = 1$, this algorithm is called the k_{T} algorithm [101]. To ensure that events with many soft particles and a few hard particles correctly form jets around the hard particles, we set p = -1, which is called the anti-k_{T} algorithm.

For this analysis, jets are reconstructed from PF objects [105] using the anti-k_{T} algorithm [106] with $R = 0.5$. Jet reconstruction starting with the PF particle collection substantially improves the performance of the jet-finding algorithm. For example, for a $p_{\mathrm{T}} = 30$ GeV jet, 90% of all jets reconstructed from PF particles can

be matched to jets obtained from the generator-level particle collection. As a point of comparison, the same matching efficiency for jets constructed only from calorimeter cells is around 50%.

There are additional, standard CMS requirements to select quality jets. Jets from instrumental and non-collision sources are reduced by requiring that some of the jet energy comes from charged hadrons and not all from neutral hadrons. Additionally, the jet cannot be composed entirely of energy deposits in the ECAL. The energy and momentum of the jets are corrected as a function of the jet p_{T} and η to account for the non-linear response of the calorimeter and dead regions.

For each event, an average energy density from pileup based on number of reconstructed vertices is determined. The energy contribution from pileup is computed for each jet, based on the area of the jet. This energy is subtracted from the jet [107].

Once the collection of jets is defined, AVF is used on the jet collection to find secondary vertices (SV) within the jets. The combined secondary-vertex (CSV) algorithm then uses information from the track impact parameter and SV information to discriminate between jets that originate from b quarks (b-tagged jets) and jets from light-flavor quarks and gluons. The medium working point of the CSV b-tagging procedure identifies jets originating from b quarks with an efficiency of approximately 70% and misidentifies jets from c quarks with a rate of approximately 20% and light-flavor quarks or gluons at a rate of approximately 1% [108].

The dominant process at the LHC is QCD production, with quarks and gluons in the final state. Though these are typically reconstructed as jets, hadron decay (e.g., b decays) can result in leptons. To reduce this background, isolation constraints are imposed on the energy $E_{T,\mathrm{cone}}$ from particle tracks or deposits in the calorimeter within a cone $\Delta R = \sqrt{(\Delta\eta)^2 + (\Delta\phi)^2} = 0.4(0.3)$ around the trajectory of a muon (electron) candidate. The energy from the reconstructed lepton is subtracted from $E_{T,\mathrm{cone}}$. Using a similar procedure as the pileup energy subtraction corrections described above for jets, the average energy density from pileup collisions is also subtracted from $E_{T,\mathrm{cone}}$.

Muons are reconstructed using PF with a combined fit of momentum information from the tracking system and the muon chambers. Cosmic ray muons are rejected by requiring that the transverse (longitudinal) impact parameter be less than 2 (5) mm relative to the PV. Only muons with at least ten hits in the silicon strip tracker and at least one hit in the pixel detector are considered, which ensures a precise momentum measurement. Isolation is imposed by the requirement that $E_{T,\mathrm{cone}}$ be less than 12% of the muon p_{T} [58].

Electrons are reconstructed by matching an energy cluster in the ECAL with a track reconstructed using a Gaussian sum filter [109]. The difference in the inverse cluster energy determined from the ECAL and the inverse track momentum must be within $0.05\,\mathrm{GeV}^{-1}$, and the shape of the cluster in the ECAL must be consistent with the shape expected for an electron. To reduce backgrounds that arise from photon conversions in the inner pixel detector, at least one pixel hit in the innermost pixel layer is required and the electron must be inconsistent with photon pair production

in the tracker. The energy behind the cluster in the HCAL is computed, and the ratio of the HCAL to ECAL energy must be less than 0.12. The track for the electron candidate must have a longitudinal impact parameter of less than 1mm. The electron is isolated from other activity in the event by requiring that $E_{T,\text{cone}}$ be less than 10% of the electron p_{T} [110].

The magnitude of $\vec{p}_{\text{T}}^{\text{miss}}$ is referred to as $E_{\text{T}}^{\text{miss}}$ and is computed using the sum of all PF particles.

4.4 Data and trigger

Data used for this search were collected in 2012, and correspond to 19.7 fb^{-1} at $\sqrt{s}$ =8 TeV. The data were collected using a trigger based on a single isolated muon with p_{T} greater than 24 GeV and $|\eta| < 2.1$.

The scalar sum of the transverse energy in the event S_{T} is computed as the scalar sum of the p_{T} from jets, electrons, muons and $E_{\text{T}}^{\text{miss}}$ (for $E_{\text{T}}^{\text{miss}} > 15$ GeV). The following kinematic requirements are applied:

- Jet $p_{\text{T}} > 30$ GeV, $|\eta| < 2.4$,
- Muon $p_{\text{T}} > 30$ GeV, $|\eta| < 2.1$,
- Electron $p_{\text{T}} > 15$ GeV, $|\eta| < 1.44$,
- $S_{\text{T}} > 300$ GeV.

To prevent overlaps, any electron found within $\Delta R < 0.3$ of a muon is removed from the electron collection. For stealth SUSY signal, this selection was found to not remove any electrons that would otherwise meet the reconstruction requirements. Then, any jet found to be within $\Delta R < 0.5$ of a reconstructed electron or muon is removed from the jet collection.

Events with an opposite-charge electron and muon (eμ) are selected. This reduces the otherwise dominant QCD and W+jets backgrounds. The remaining SM background comes from: $t\bar{t}$, single top quark, DY, and diboson (WW, WZ, ZZ) processes. The requirement of exactly two leptons reduces the small contribution from WZ and ZZ. DY can produce eμ from $Z \to \tau\tau$, $\tau \to$e(μ). A small contribution to the total SM background also comes from non-prompt events where one or more of the jets results in an isolated lepton (from b decays, for instance).

The jet multiplicity N_{jets} must be at least four, and none of those jets can be b-tagged. This reduces the contribution from $t\bar{t}$, though it still remains the dominant background.

4.5 Optimization

For stealth-SUSY events with a large squark mass, the squarks are essentially produced at rest, and decay into leptons and jets within the acceptance requirements on each object, resulting in the scalar sum of p_{T} being approximately equal to the squark mass. Thus, because the squarks are pair produced, the S_{T} in the event is approximately twice the mass of the squark. To obtain an optimized analysis for a range of squark masses, the S_{T} thresholds for each squark mass hypothesis were optimized. As a figure of merit, we use the Z_{Bi} [111] variable, which is the ratio of the Poisson means of the expected signal and background, given the systematic uncertainty in the expected background. The backgrounds were estimated from MC simulation. The value of Z_{Bi} is computed in bins of the S_{T} threshold $S_{\mathrm{T}}^{\mathrm{min}}$, with the systematic uncertainty in the dominant background, $t\bar{t}$, included. The optimum $S_{\mathrm{T}}^{\mathrm{min}}$ values as a function of the squark mass are summarized in Table 4.3.

Table 4.3: Summary of the S_{T} optimization results showing the optimum maximum Z_{Bi} $S_{\mathrm{T}}^{\mathrm{min}}$ values as a function of the squark mass. In addition, both the $S_{\mathrm{T}}^{\mathrm{min}}$ value used in the analysis and the corresponding maximum Z_{Bi} value for each squark mass are shown. For all squark masses greater than 600 GeV, the same $S_{\mathrm{T}}^{\mathrm{min}}$ values, determined from the 600 GeV squark mass are used.

	Optimum		Actual used	
$M_{\tilde{q}}$	Z_{Bi}	$S_{\mathrm{T}}^{\mathrm{min}}$ (GeV)	Z_{Bi}	$S_{\mathrm{T}}^{\mathrm{min}}$ (GeV)
300	11.9	300	11.9	300
400	3.9	500	3.1	700
500	2.5	700	2.5	700
600	2.0	1200	2.0	1200
700	2.0	1200	2.0	1200

Because three S_{T} thresholds (300, 700 and 1200 GeV) are nearly optimal for all mass points, the analysis is simplified by using only these three S_{T} bins.

4.5.1 Sensitivity of $E_{\mathrm{T}}^{\mathrm{miss}}$ to stealth SUSY

Since the signal contains two $W \to \ell\nu$ decays, there could be some $E_{\mathrm{T}}^{\mathrm{miss}}$ in the events. To determine if an $E_{\mathrm{T}}^{\mathrm{miss}}$ requirement would add sensitivity to the analysis, the ratio $S/\sqrt{B}$ is evaluated, where S is signal for a 300 GeV squark and B is background from MC as a function of minimum and maximum requirements on the value of $E_{\mathrm{T}}^{\mathrm{miss}}$ in the event. As demonstrated by Fig. 4.3, imposing no constraints on $E_{\mathrm{T}}^{\mathrm{miss}}$ gives $S/\sqrt{B} \approx 20$. Requiring that $E_{\mathrm{T}}^{\mathrm{miss}}$ be less than 100 GeV makes a marginal improvement in sensitivity. To maintain sensitivity to a range of models with or without $E_{\mathrm{T}}^{\mathrm{miss}}$, we imposed no explicit requirement on $E_{\mathrm{T}}^{\mathrm{miss}}$.

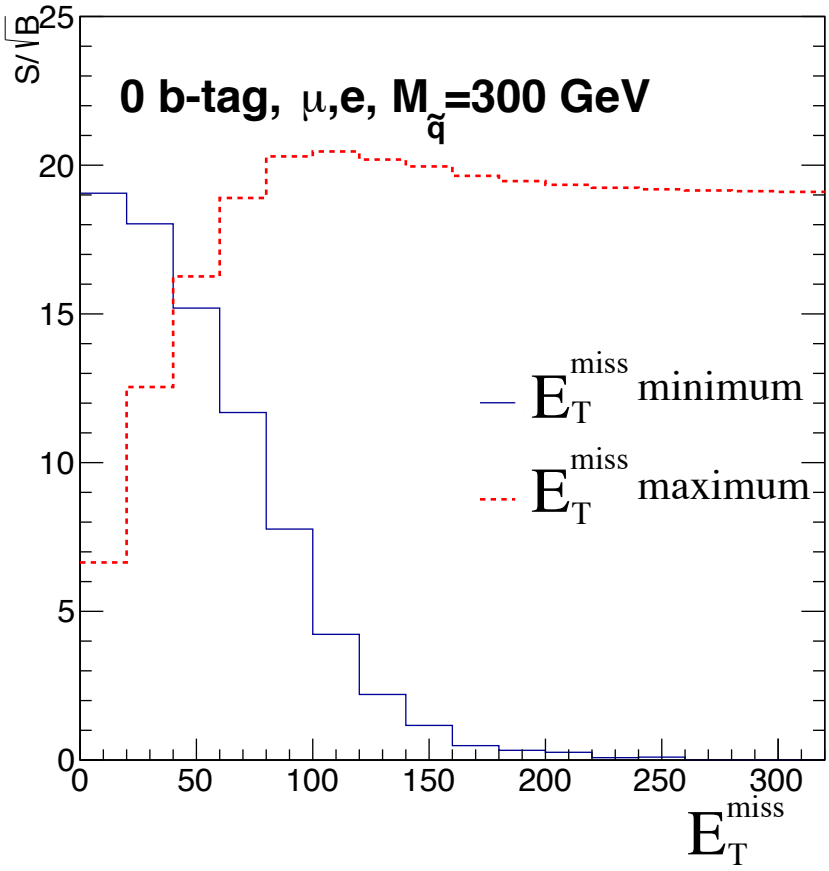

Figure 4.3: The $S/\sqrt{B}$ distribution as a function of the requirement on the minimum and maximum $E_{\mathrm{T}}^{\mathrm{miss}}$ values in an event, for MC events with opposite-sign μ,e, ≥ 4 jets, and 0 b-tags, for a 300 GeV squark mass.

4.6 Background estimation

Because of the potential dependence of SM processes on generator assumptions such as the renormalization and factorization scale, the accuracy of the jets that arise from PS simulations, the jet matching scale, and higher-order diagrams not included in the generation, particular care is taken to establish control samples in data that are not contaminated by signal. The data-driven estimation procedure for each background, based on the control samples listed in Table 4.4, are explained below.

Most of the background estimation procedures, though data-driven, still rely on MC simulation. The background estimation procedure is validated using a signal-depleted sample of events with one b-tagged jet.

4.6.1 MC reweighting

,

The efficiencies of the trigger requirement, the jet b-tagging, and the lepton identification procedure are measured in data and simulation. The simulation is then corrected to match the efficiencies in data. In addition, the simulated samples are generated with a pileup distribution slightly different than the data, and the simulation pileup distribution is reweighted to that measured in data.

To account for each of these effects, we scale the MC distributions by a weight:

$$w = \frac{\sigma \cdot L_{\text{int}}}{N^{\text{gen}}} \cdot w_{\text{pileup}} \cdot w_{\text{trigger}} \cdot w_{\text{eID}} \cdot w_{\text{btag}} \tag{4.4}$$

where each term is defined as

- σ: LO or NNLO cross section as available (see Table 4.1),
- L_{int}: integrated luminosity (19.7 fb^{-1}),

Table 4.4: Summary of the search and control samples used to estimate each background. The table is broken into categories of dilepton flavor ($\ell\ell$), whether the leptons are the same sign (SS) or opposite sign (OS), the number of jets, and the number of b-tagged jets.

Selection	Leptons	N_{jets}	$N_{\text{b-tagged jets}}$
Search	OS e,μ	≥ 4	0
Top shape	OS e,μ	$\geq$2	$\geq$2
Top normalization	OS e,μ	< 4	0
Drell-Yan	OS μ,μ	$\geq$2	0
Non-Prompt	SS e,μ	$\geq$2	0
Validation	OS e,μ	$\geq$2	1

- N^{gen}: number of generated MC events,
- w_{trigger}: weight that corrects the muon trigger efficiency to data,
- w_{eID}: weight that corrects the electron ID efficiency to data,
- w_{btag}: weight that corrects the b-tag efficiency to data and,
- w_{pileup}: weight that corrects the MC pileup distribution to the pileup distribution in data.

The first term in the expression, $\frac{\sigma \cdot L_{int}}{N^{gen}}$, normalizes the MC distribution to the theoretical cross section. Three corrections based on differences between the efficiency measurements in data and the MC are made. The trigger is applied to MC directly using the HLT trigger emulator. Then the $w_{trigger}$ scale factor corrects for the difference between the efficiencies measured using data and MC simulation. In the dimuon control sample, to account for the possibility of either 1 or 2 muons in the event, the following expression is evaluated:

$$w_{\text{trigger}} = \frac{[1-(1-\epsilon_1)\cdot(1-\epsilon_2)]^{\text{data}}}{[1-(1-\epsilon_1)\cdot(1-\epsilon_2)]^{\text{MC}}} \tag{4.5}$$

where ϵ_1 (ϵ_2) is the efficiency for each muon measured in p_{T} and η bins. All other selection regions contain only one muon in the event selection, so the w_{trigger} is always equal to ε_1. For selections with one electron, we apply a single scale factor. Since the signal is generated with the fast simulation rather than the full detector simulation, there is an additional scale factor (0.95-0.99) to account for the lepton efficiency difference between these simulation procedures.

The pileup distribution of the MC simulation is reweighted to match the distribution in data. The number of primary vertices for data and background the MC-simulated before pileup reweighting is shown in Fig.4.4 on the left, and on the right after reweighting.

The b-tagging efficiency and fake rate as implemented in the MC simulation is corrected by the factor w_{btag}. This factor is derived from b-tag efficiency measurements in data. The efficiency of reconstructing a b-tagged jet can be measured in data using a variety of procedures, including reconstruction of events with top quarks [112]. For each jet, the efficiency in the MC simulation is corrected by the scale factor SF=$\varepsilon_{data}/\varepsilon_{MC}$. Typically the scale factors range from 0.9–1.1. The scale factors for b and c quarks are the same, and light flavor quarks (udgs) are computed separately. The approach is to compute the event-by-event weight to scale the MC simulation events to the data, which requires both the SF and b-tagging efficiency. The b-tagging efficiency in the MC simulation, binned in jet flavor, η and p_T, is defined as:

$$\varepsilon_{flavor}(\eta, p_T) = \frac{N^{b-tagged}_{flavor}(\eta, p_T)}{N^{total}_{flavor}(\eta, p_T)}, \tag{4.6}$$

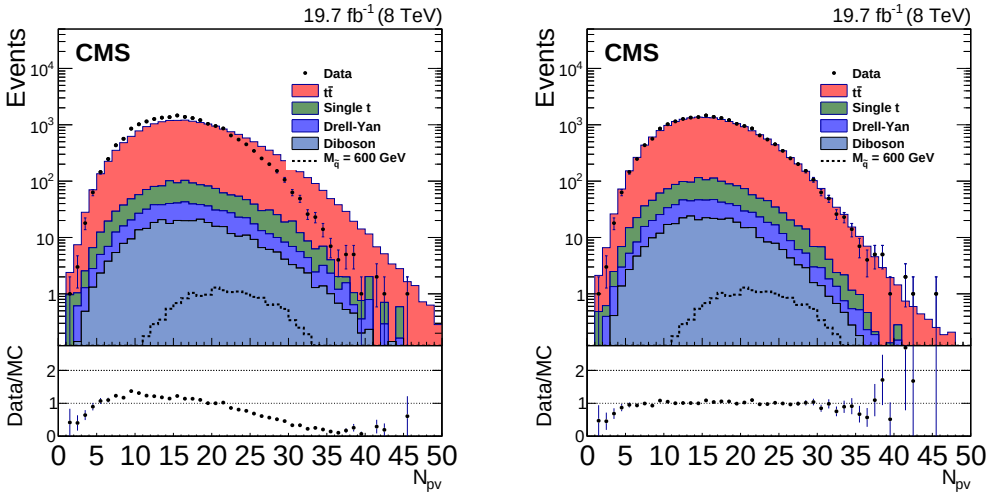

Figure 4.4: The number of primary vertices for events in data and MC simulation with ≥ 2 jets, μ,e. Left: before pileup reweighting. Right: after pileup reweighting

where the efficiency is computed separately for the MC simulation truth jet flavors. This efficiency is computed separately for b, c, g, and u, d, s. The flavor of the parton assigned to the jet is based on the parton within the cone $\Delta R = 0.3$ around the jet axis. If multiple partons are found within the jet, preference is given to largest-mass parton. Note that some low-p_T jets do not have a jet flavor defined. These jets are included in the u, d, s efficiency.

The probability of having a given jet and b-tag configuration in the MC simulation is:

$$P(\text{MC}) = \prod_{i=\text{tagged}} \varepsilon^i_{flavor} \prod_{j=\text{not tagged}} (1 - \varepsilon^j_{flavor}). \tag{4.7}$$

The corresponding probability for the event in data is computed by replacing ε with $SF \cdot \varepsilon$,

$$P(\text{data}) = \prod_{i=\text{tagged}} SF^i_{flavor} \cdot \varepsilon^i_{flavor} \prod_{j=\text{not tagged}} (1 - SF^j_{flavor} \cdot \varepsilon^j_{flavor}). \tag{4.8}$$

Note that $P(\text{data})$ is not evaluated for data events. Instead, it is evaluated for MC simulation events and gives the probability one would expect in data based on the measured b-tag efficiencies. The event weight:

$$w_{\text{btag}} = P(\text{data})/P(\text{MC}) = \prod_{i=\text{tagged}} SF^i_{flavor} \frac{\prod_{j=\text{not tagged}} (1 - SF^j_{flavor} \cdot \varepsilon^j_{flavor})}{\prod_{j=\text{not tagged}} (1 - \varepsilon^j_{flavor})} \tag{4.9}$$

is then used to correct each MC simulation event.

4.6.2 $t\bar{t}$ + jets

For the $t\bar{t}$ background, corrections are made to the N_{jets} distribution using a sample of events with ≥ 2 b-tagged jets, where N_{jets} is the total number of jets including the b-tagged jets. Then a sample of data events with 2 or 3 jets is used to normalize the distribution in the signal region that has 0 b-tagged jets.

The N_{jets} distribution from $t\bar{t}$ events is is studied in a sample of MC simulated events with ≥ 2 b-tagged jets, as shown in Fig. 4.5. As demonstrated by the figure, the control sample does not allow $t\bar{t}$ and single top events to be distinguished, so the procedure to estimate $t\bar{t}$ background combines $t\bar{t}$ and single top events and are referred to as "top". For each jet multiplicity bin we compute the shape correction factor,

$$C_{\text{shape}}(N_{\text{jets}}) = \frac{N^{\text{data}}}{M^{\text{top}}}(N_{\text{jets}})\frac{M^{\text{top}}}{N^{\text{data}}}(\text{All jet bins}), \tag{4.10}$$

where N^{data} is the number of data events in the ≥ 2 b-tagged jets sample and M^{top} the number of simulated top events. The fraction on the left is binned in N_{jets} and describes deviations of data from MC simulation in each bin. The normalization is then divided out using the fraction on the right, so that C_{shape} is independent of the overall normalization predicted by the $t\bar{t}$ simulation. C_{shape} is evaluated for $S_{\text{T}} > 300$ GeV. To check for an S_{T} -dependent effect, we evaluate C_{shape} using exclusive S_{T} bins: 300–700 GeV and ≥ 700 GeV. The shapes are statistically compatible. Finally, the MC simulation prediction in the 0 b-tagged jet signal region is corrected by C_{shape} in each N_{jets} bin.

For the $t\bar{t}$ and single top quark MC simulation, the normalization was derived using the 2 or 3 jet data, with 0 b-tagged jets. The sample with 0 b-tagged jets is dominated by $t\bar{t}$ background, which always decays to two b quarks. For top events to be reconstructed with 0 b-tagged jets, there are three possibilities: there are two b jets that satisfy the selection requirements but they are not b-tagged, only one b jet is in the acceptance and the other not b-tagged, and there are no b jets that satisfy the selection criteria. The typical fraction of events is 60%, 30%, and 10%, respectively. As demonstrated by Eq. 4.9, the overall normalization of $t\bar{t}$ and single top quark MC simulation is impacted by the b-tag efficiency and therefore depends on the number of b-tagged jets, but is insensitive to N_{jets}. The normalization region was chosen to have 0 b-tagged jets to remove sensitivity to the b-tag efficiency. The normalization correction is defined as:

$$C_{\text{norm}} = \frac{N^{\text{data}} - M^{\text{DY}} - M^{\text{diboson}} - N^{\text{non-prompt}}}{M^{\text{top}}}, \tag{4.11}$$

where N is the number of data events and M the number of simulated events for each sample. When evaluated with events that have $S_{\text{T}} > 300$ GeV, $C_{\text{norm}} = 0.97 \pm 0.02$, where the uncertainty is statistical. To check for an S_{T} dependence on the normalization, the sample is split into two exclusive S_{T} bins: 300–700 and ≥ 700 GeV. The normalization coefficients are 0.97 ± 0.02 and 0.86 ± 0.12, respectively. Here the

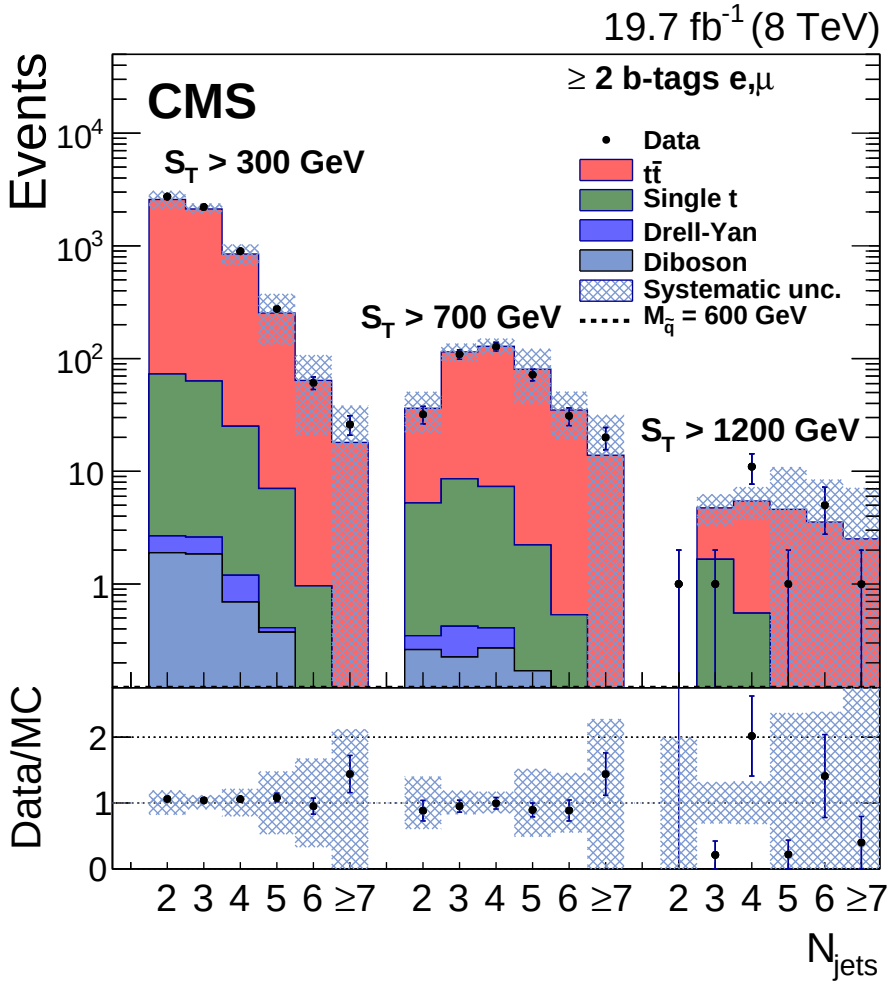

Figure 4.5: Distribution of N_{jets} for data and MC simulation for three S_{T} thresholds in the "top shape" control sample (see Table 4.4). The lower plot shows the ratio of the data and simulation, with systematic uncertainties derived from variations of the renormalization/factorization scale shown by the shaded bands. The (negligible) signal contribution to this control sample is shown by the dashed line that appears to coincide with the horizontal axis.

uncertainties are only statistical. Since the coefficients are statistically compatible, the normalization from the inclusive bin $S_{\text{T}} > 300$ GeV is used, and a conservative systematic uncertainty assigned to cover the difference (see Section 4.7).

4.6.3 Drell-Yan + jets

DY processes produce only 10% of the total background. We estimate the normalization corrections to DY in bins of N_{jets}. The control sample with at least six jets

has substantial signal contamination from stealth SUSY if the squark mass is 300 GeV. To account for this contamination, we designed a fitting procedure to separate DY events which have a Z peak in the dimuon invariant mass distribution from non-peaking background and potential signal. The DY and diboson shapes were evaluated using simulation, and the additional background was parameterized as a first-order polynomial. Table 4.5 shows the result of a fit to background MC simulation events. This trivial closure test ensures that the number of DY events from background MC simulation matches the number of fit DY events from the fit. In addition, the number of top background events agrees with the number associated with the polynomial normalization. We then perform the same fit after simulated stealth SUSY signal events are injected. To do this, we constructed a histogram that is the sum of all SM backgrounds and simulated signal events. As demonstrated by Table 4.6, the number of DY events from the fit is consistent with the number included in the MC simulation. The top background and injected signal events are described by the polynomial. The signal injection test gives us confidence that the fitting procedure can separate the number of DY events from potential signal. We fit the data to extract the actual number of DY events in each jet bin, as shown in Table 4.7. A sample fit for the 5-jet bin is illustrated in Fig. 4.6. We then correct the DY MC simulation in bins of N_{jets}, using the ratio R of the number of DY events from the fit compared to the number expected in MC. This number is reported in Table. 4.8, where the uncertainties are statistical.

Table 4.5: Inputs and results for fits to combination of background MC simulation samples, where N_{DY}, N_{diboson}, and N_{top} are the number of DY, diboson and top events from the MC simulation, respectively. N_{sig} is the number of signal events, which is 0 in this table. The right hand side of the table shows the number of fit DY events, and the number of background events from the polynomial function in the fit, N_{pol}. In this example, this parameterization only accounts for top background. The parameter $p1$ is the slope of the polynomial, and $N_{diboson}$ is fixed in the fit.

	MC Composition				Fit results			
N_{jets}	N_{DY}	N_{diboson}	N_{top}	N_{sig}	N_{DY}	N_{diboson}	N_{pol}	p1
2	33490	485	783	0	33540 ± 200	485	679 ± 82	-0.1 ± 0.2
3	15580	340	485	0	15610 ± 137	340	433 ± 57	-0.2 ± 0.2
4	3665	105	123	0	3674 ± 67	105	110 ± 29	-0.3 ± 0.3
5	429	15	18	0	430 ± 23	15	17 ± 10	-0.5 ± 0.6
6	27	1.3	2	0	28 ± 6	1.3	1.2 ± 2.4	-1.0 ± 1.8

Table 4.6: Inputs and results for fits to combinations of background MC simulation samples, where N_{DY}, N_{diboson}, and N_{top} are the number of DY, diboson and top events from the MC simulation, respectively. N_{sig} is the number of signal events from the simulated stealth model with a 300 GeV squark. The right hand side of the table shows the number of fit DY events, and the number of background events from the polynomial function in the fit, N_{pol}. Here N_{pol} describes both the events from top background and signal. The parameter $p1$ is the slope of the polynomial, and N_{diboson} is fixed in the fit.

	MC Composition				Fit results			
N_{jets}	N_{DY}	N_{diboson}	N_{top}	N_{sig}	N_{dDY}	N_{diboson}	N_{pol}	p1
2	33490	485	783	32	33540 ± 200	485	711 ± 82	-0.1 ± 0.1
3	15580	340	485	88	15620 ± 137	340	511 ± 58	-0.2 ± 0.1
4	3665	105	123	137	3700 ± 68	105	221 ± 32	-0.4 ± 0.2
5	429	15	18	76	432 ± 24	15	91 ± 15	-0.5 ± 0.2
6	27	1.3	2	12	26 ± 6	1.3	15 ± 5	-0.7 ± 0.4

Table 4.7: Results of the fit to data for the determination of the DY normalization. The uncertainties are statistical only.

N_{jets}	N_{DY}	N_{diboson}	N_{pol}	p1
2	34210 ± 202	485	911 ± 86	-0.1 ± 0.1
3	16910 ± 142	340	448 ± 59	-0.4 ± 0.2
4	4033 ± 70	105	135 ± 30	-0.1 ± 0.3
5	526 ± 25	15	31 ± 11	-0.7 ± 0.4
6	42 ± 7	1.3	0 ± 3	-0.8 ± 1.8

Table 4.8: The DY correction factor R as a function of N_{jets}. The uncertainties are statistical only.

N_{jets}	R
2	1.02 ± 0.01
3	1.09 ± 0.01
4	1.10 ± 0.02
5	1.22 ± 0.06
6	1.56 ± 0.25

4.6.4 Diboson + jets

The expected background from diboson processes are estimated from simulation. It is assumed that any mis-modeling of the jet multiplicity, as seen for the DY background also applies to diboson backgrounds (see Section 4.7).

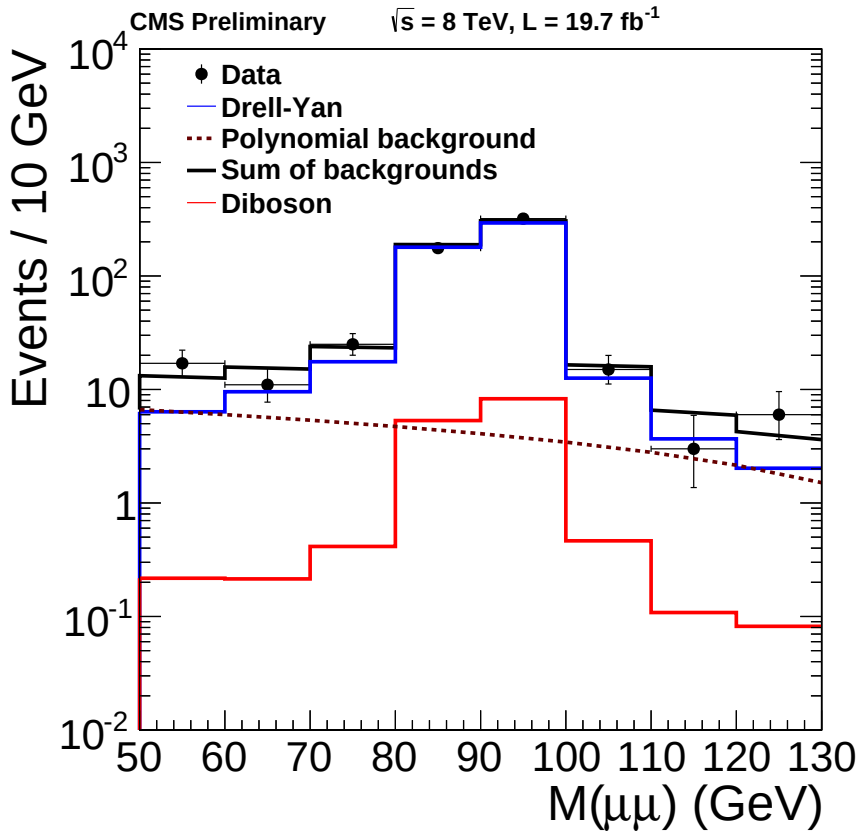

Figure 4.6: Results from a sample fit for events with 5-jets, demonstrating the DY fit method as applied to the dimuon invariant mass distribution. The figure shows the results of the best overall fit to the DY normalization background (blue curve), and the polynomial term (brown curve). The diboson background (red curve) that contains a peak near 90 GeV is fixed from simulation. The sum of all background components (black curve) has a slope across each bin introduced by the polynomial background, which is a continuous function.

4.6.5 Non-prompt

To estimate the background from non-prompt sources such as W+jets or $t\bar{t}$ events where at least one lepton originates from a jet rather than a W decay, we use a control sample of same-sign (SS) eμ pairs, as shown in Fig. 4.7. To estimate this effect, we subtract the contribution that is already included in the background estimation from the data, then use the difference as an estimate on the non-prompt backgrounds in the opposite-sign (OS) sample. Due to the low event counts at high jet multiplicity and S_{T} , we rely on a fit of the jet multiplicity for $S_{\mathrm{T}} > 300\,\mathrm{GeV}$. We use an exponential shape, as illustrated in Fig. 4.7, to extrapolate the N_{jets} distribution to large values

of N_{jets}. In each S_{T} bin, the shape from the SS control sample is normalized to the total number of events.

4.6.6 Validation

After estimating the top, DY and non-prompt backgrounds from data, we use a sample of data events with 1 b-tagged jet to validate the data-driven background procedures. As depicted in Fig. 4.8, the predicted background in this signal free region agrees with the number of observed events. The systematic uncertainties shown in the plot will be described in Section 4.7.

4.7 Systematic uncertainties

The sources of systematic uncertainty can be divided into two categories: uncertainty in the number of expected background events and in the signal efficiency. The sources of uncertainty affecting the background estimate are described below, roughly in order of decreasing importance.

- **Top normalization**: The systematic uncertainty in the top normalization is determined from the statistical uncertainty in the data used to evaluate Eq. 4.11.

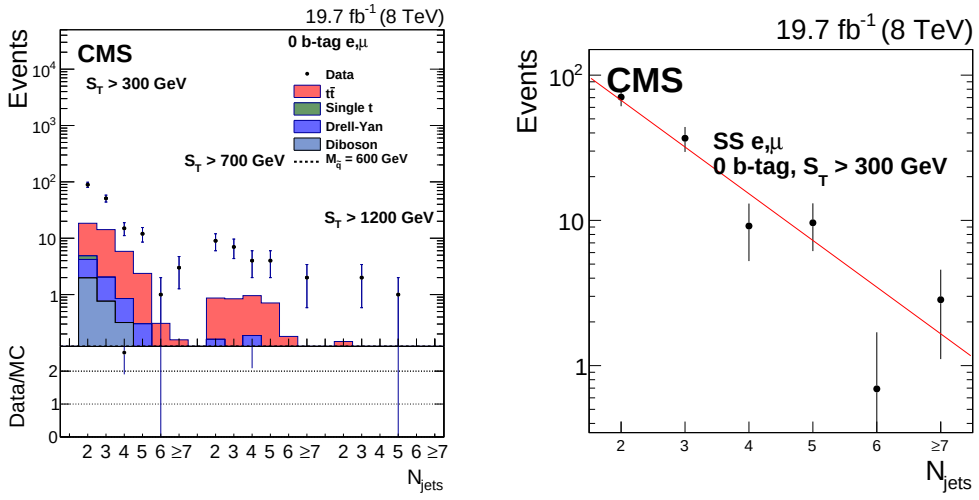

Figure 4.7: Left: Comparison of N_{jets} distributions from data and MC simulation in the SS e-μ non-prompt control sample for three different values of $S_{\text{T}}^{\text{min}}$. The predicted contributions from the various backgrounds are shown by the histograms and the expected contribution from a 600 GeV squark is shown by the dotted line. The excess in the data estimates the non-prompt backgrounds that are unaccounted for in the OS search region. Right: Fit of the jet multiplicity distribution for SS eμ pairs with 0 b-tags, to an exponential, for $S_{\text{T}} > 300$ GeV.

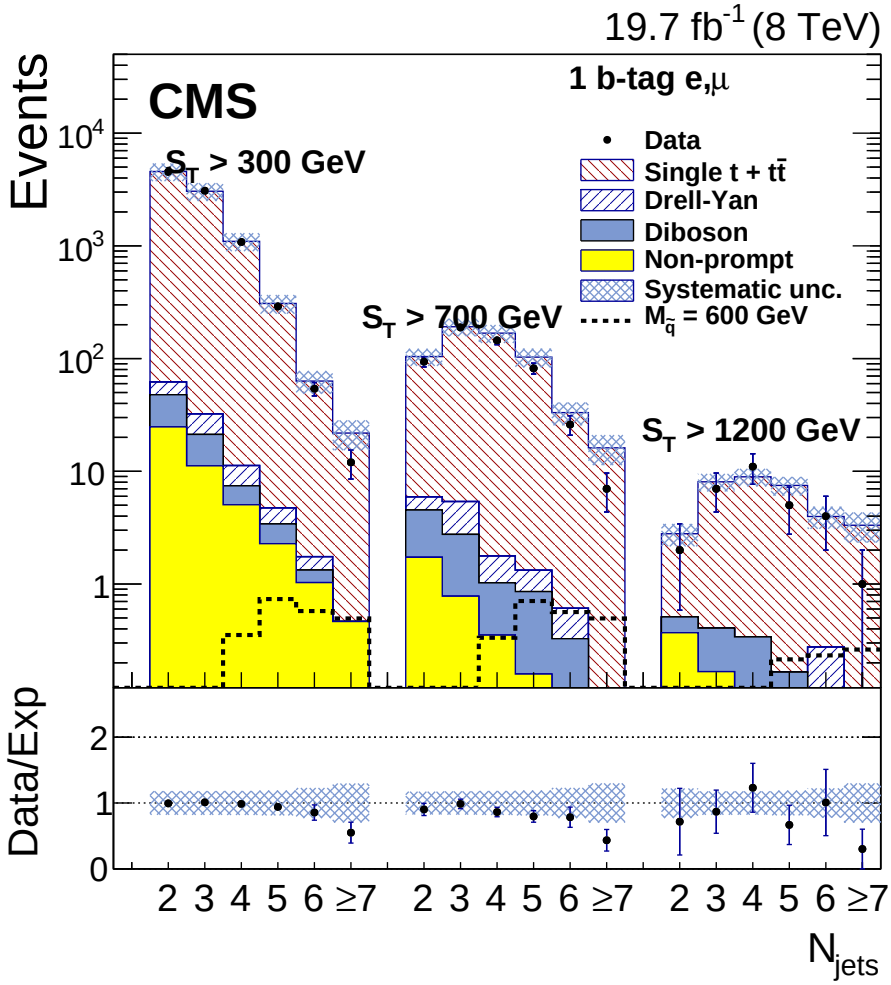

Figure 4.8: The N_{jets} distribution observed in data and the prediction from MC simulation for the signal sample with 1 b-tagged jet for three different values of $S_{\text{T}}^{\text{min}}$. The predicted contributions from the various backgrounds are shown by the histograms and the expected contribution from a 600 GeV squark is shown by the dotted line. The cross hatched region shows the systematic uncertainties, described in Section 4.7.

In addition, to account for a possible S_{T} dependence of the normalization, we divide the sample into two exclusive bins, $300 < S_{\text{T}} < 700$ GeV and $S_{\text{T}} > 700$ GeV. The resulting normalization coefficients are 0.97 ± 0.02 and 0.86 ± 0.12, respectively, where the uncertainties are statistical. Although the results agree within the uncertainties, we assign a 15% systematic uncertainty. This is determined from the sum in quadrature of the individual statistical uncertainties and the difference in normalization between the two S_{T} bins.

- **Top shape**: The uncertainty in the shape of the N_{jets} distribution for the top background is determined from the statistical uncertainty on the number of data events used to evaluate Eq. 4.10, in each N_{jets} bin. This uncertainty ranges from negligible to 20%, depending on jet multiplicity.

- **Top simulation** : To understand how the MC simulation inputs to Eq. 4.11 and Eq. 4.10 depend on generator parameters in the top simulation, we recompute the background prediction with the renormalization and factorization scales varied by a factor of 2 (0.5). Since the background estimation is derived using data, it should be insensitive to these parameters. However, we find that there is a 10% variation in the number of expected top background events for $N_{\text{jets}} \geq 4$, which we assign as an additional systematic uncertainty.

- **B-tagging efficiency and fake rate**: Each b-tag efficiency scale factor described in Section 4.6.1 has an associated systematic uncertainty, and depend on the jet p_{T}, η, and correct flavor from the MC simulation. These uncertainties are typically 5–8%. In addition, the scale factors of b and c jets are correlated with each other, but uncorrelated with the light-flavor jets. The systematic uncertainty is determined by separately evaluating Eq. 4.9, with the scale factors shifted by their systematic uncertainties for any b or c jet: $w_{\text{b,c}} = w(SF_{b,c} \pm \sigma_{SF_{b,c}})$. For light-flavor jets, Eq. 4.9 is evaluated again with the variation: $w_{\text{light}} = w(SF_{light} \pm \sigma_{SF_{light}})$. The uncertainties are then combined in quadrature, so the total uncertainty for a given number N of MC simulation events with weights from Eq. 4.9 is given by:

$$N_{\pm} = N \pm \sqrt{(N_{b,c} - N)^2 + (N_{light} - N)^2} \tag{4.12}$$

  where N_{bc} and N_{light} are the number of events computed as the b-tag efficiency scale factors are varied by the b, c and light-flavor quark systematic uncertainties. The final uncertainty on the top background is determined by evaluating Eq. 4.10 with the estimates from the MC simulation varied by $N_{\pm}$ from Eq. 4.12. This uncertainty is 1–3% depending on the jet multiplicity, and is substantially smaller than the uncertainty on the b-tag efficiency scale factors. The systematic uncertainty related to b-tagging is reduced because the top background prediction is normalized in a bin with the same number of b-tags as the signal region.

- **Drell-Yan and diboson**: For each jet multiplicity bin, we take half the correction to the DY MC simulation from the fit in the control sample (Table 4.8) as the uncertainty.

- **Diboson**: We assign a 30% uncertainty to cover the difference between the CMS measurement of the WW cross section [113] and the theoretical cross section. In addition we assume that mis-modeling of the jets in the DY MC

simulation could also be an issue for the diboson MC simulation. We add a 30% uncertainty in quadrature with half the correction from the DY fit in the control sample (Table 4.8). We do not apply this correction to the diboson background.

- **Non-prompt**: We use the Poisson uncertainty on the number of non-prompt events in the SS control region.

- **Finite-size MC simulation**: We assume a Poisson uncertainty on the number of background MC simulation events. For $t\bar{t}$ this is 0-6%, Drell-Yan 4-50% and diboson 2-35%.

The sources of uncertainty affecting the signal efficiency are described below in order of roughly decreasing importance.

- **Jet energy scale**: We evaluate the change in the signal efficiency as the jet energy scale is varied within its one-standard-deviation uncertainties. The resulting changes depend on the squark mass and N_{jets} bin, and the maximum deviation was 5% of the efficiency computed using the nominal jet energy scale. Thus, we conservatively assign an uncertainty of 5% for all squark masses and N_{jets} bins.

- **Finite-size MC simulation**: The uncertainty on the signal efficiency due to the finite-size of the MC simulation samples ranges from negligible to 7%, depending on jet multiplicity.

- **Pileup**: We find that the signal efficiency does not depend on the vertex multiplicity. Therefore, the uncertainty assigned to pileup effects is negligible. Pileup does not contribute to the systematic uncertainty because the selections used are not impacted by pileup.

- **Lepton trigger and ID systematics**: We assign a 1% systematic for the muon trigger and identification, and a 3% uncertainty for the electron identification.

- **Luminosity**The uncertainty on the luminosity is 2.6% as determined by the CMS Lumi Group [114].

The relative systematic uncertainties are summarized in Table 4.9.

Table 4.9: Table of systematic uncertainties.

Source	Uncertainty
Top normalization	15%
Top shape	negligible–20%
Top simulation	10%
B-tag efficiency and fake rate	1–3%
Drell-Yan	10–30%
Diboson	30–48%
Non-prompt	50–100%
Finite MC sample	negligible–50% (depending on sample)
Luminosity	2.6%
Jet energy scale	5%
Lepton identification (trigger)	1(3)%

4.8 Results and interpretation

The expected and observed numbers of events in the signal region are depicted in Fig. 4.9 as a function of N_{jets} for three values of $S_{\text{T}}^{\text{min}}$. As demonstrated by the figure, the background tends to fall rapidly with increasing N_{jets}, while the signal tends to produce events with large values of N_{jets}. The three S_{T} bins are used to improve the sensitivity to higher-mass squarks, as described in Table 4.3. The data agree with the expected background.

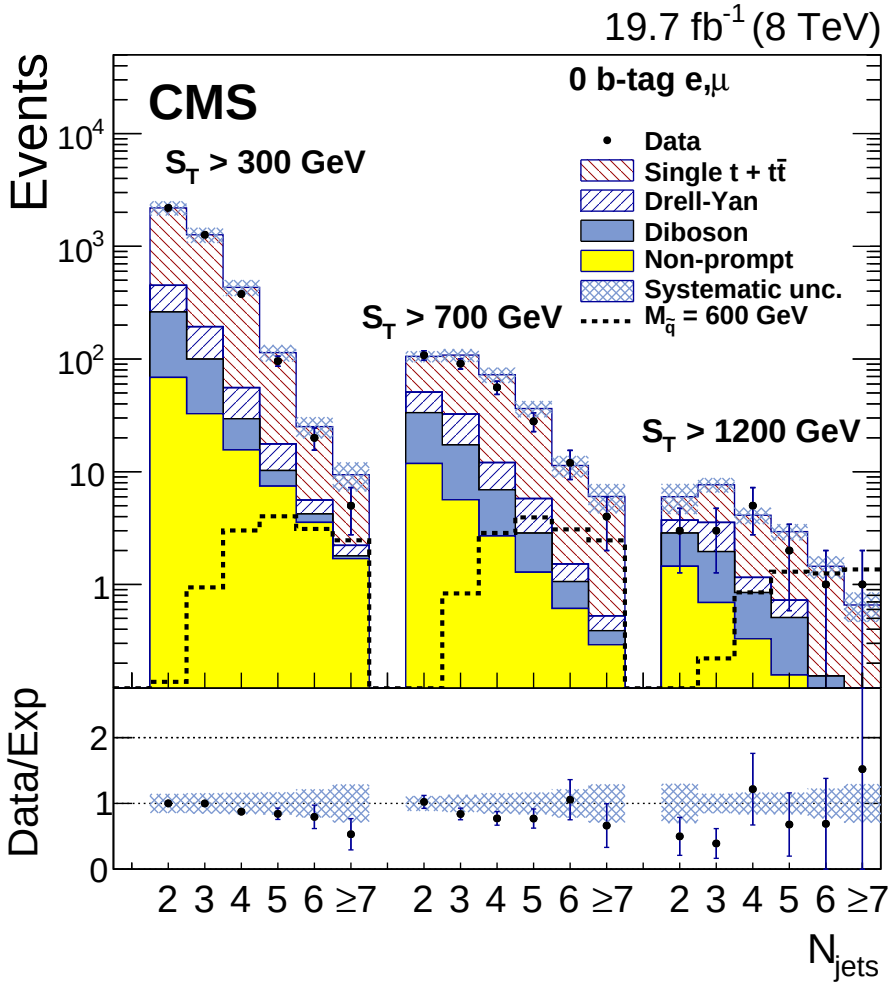

Figure 4.9: The N_{jets} distributions for three different values of $S_{\text{T}}^{\text{min}}$ from the data and the data-driven background prediction for the search region with 0 b-tagged jets.

4.8.1 Calculation of cross section upper limits

To determine the limit on the stealth SUSY cross section based on the data, we use the frequentist-inspired CLs procedure [115, 116, 117]. We assume that if X is the number of measured events, that they will be Poisson distributed and result in the likelihood:

$$\mathcal{L}(X|\mu,\nu) = \frac{e^{-\lambda(\mu,\nu)}\lambda^X(\mu,\nu)}{X!}, \tag{4.13}$$

where $\lambda(\mu,\nu)$ is the number of expected events. The signal strength modifier μ scales the number of expected signal events, and ν is the nuisance parameter. The nuisance parameter accounts for the dependence of λ on theoretical or experimental effects, for example the jet energy scale. Typically there are many nuisance parameters. To account for multiple exclusive bins, we multiply the Poisson likelihoods. In addition, we consider constraints on each nuisance parameter to be independent experiments, where ν is distributed according to the probability distribution function $\pi(\nu)$. Thus, a more realistic expression for the likelihood, given N bins and M nuisance parameters, is

$$\mathcal{L}(X|\mu,\vec{\nu}) = \prod_i^N \prod_j^M \frac{e^{-\lambda_i}(\mu,\vec{\nu})\lambda_i^{X_i}(\mu,\vec{\nu})}{X!}\pi_{i,j}(\nu_j) \tag{4.14}$$

where $\mathcal{L}$ is a function of all the nuisance parameters $\vec{\nu}$. The first product runs over all the exclusive bins, and the second runs over all the nuisance parameters. The distribution $\pi_{i,j}$ is defined for each bin i and each parameter j. In subsequent discussion, the vector notation will be dropped and assumed implicitly. For a given data set and prediction, a maximum-likelihood fit is performed resulting in the optimum set of nuisance parameters for a given μ, denoted by $\hat{\nu}_\mu$.

Systematic uncertainties, as summarized in Table 4.9, are treated as nuisance parameters in the likelihood. The probability distribution π for each nuisance parameter is assumed to be log-normal for the uncertainties except for the normalization of the top quark background. This is directly related to the number of events in data, and consequently treated using a gamma distribution. For the combination of jet multiplicity bins, we treat the top normalization, simulation, b-tagging, jet energy scale, and lepton identification systematic uncertainties as fully correlated. The remainder of uncertainties are treated as uncorrelated.

In general, to distinguish between hypotheses using a measured set of data, one refers to a test-statistic. In CLs, this is the log-likelihood ratio (LLR), defined as

$$q_\mu(X) = -2\ln\frac{\mathcal{L}(X|\mu,\hat{\nu}_\mu)}{\mathcal{L}(X|\mu',\hat{\nu}_{\mu'})}, \tag{4.15}$$

where $\hat{\nu}_\mu$ is the value of ν determined from the maximum-likelihood fit. The parameter μ' is the value of μ that corresponds to the global maximum of the likelihood, and $\hat{\nu}_{\mu'}$ the value of the nuisance parameter refit for μ'. An ensemble of experiments will measure a distribution of X values, and $q_\mu(X)$ will have different values for each

measurement. The distribution of these values is $f = f(q_\mu|\mu, \hat{\nu}_\mu)$. The distribution f is evaluated from toy MC simulation experiments, where X is generated using a Poisson distribution and the nuisance parameters generated according to their probability distributions. Since the use of toy experiments is computationally expensive, f can be approximated using asymptotic expansions [118].

To determine the probability that a given measurement arose from a statistical fluctuation, we evaluate the quantity:

$$CL_{S+B}(\mu) = \int_{q_\mu(X)}^{\infty} dq_\mu f(q_\mu|\mu, \hat{\nu}_\mu). \tag{4.16}$$

This is the probability that an additional measurement would produce a test-statistic greater than the measured value. We normalize this to the probability that the measurement produces a greater value of the test-statistic with the background only hypothesis, $\mu = 0$, given by:

$$1 - CL_B(\mu) = \int_{q_\mu(X)}^{\infty} dq_\mu f(q_\mu|0, \hat{\nu}_0). \tag{4.17}$$

Thus, CLs is defined as:

$$CL_S(\mu) = \frac{CL_{S+B}(\mu)}{1 - CL_B(\mu)}, \tag{4.18}$$

and can be thought of as the confidence level (CL) of the signal-only hypothesis. If CLs is less than 0.05 for a given μ, that value of μ is said to be excluded at 95% CL.

For each squark mass hypothesis, we evaluate the $\mathrm{CL_S}$ using the signal acceptance from MC simulation and the theoretical cross section for squark pair production. The four jet multiplicity bins are combined using the product of the likelihoods with the most sensitive $S_{\mathrm{T}}^{\mathrm{min}}$ value (see Section 4.5).

The upper limit on the cross section can then be computed at 95% CL, and is the maximum value of μ that satisfies Eq. 4.18. This calculation is performed for both the number of expected number of background events based on the SM, and the number of observed events, to give both expected and observed cross section limits. The expected and observed cross section limits depicted as a function of the squark mass hypothesis in Fig 4.10, which also shows the theoretical cross section for squark production. The interSection of the theoretical cross section with the expected or observed cross section can be interpreted as a lower limit on the squark mass. Thus, based on the 95% CL upper limit on the cross section, we can exclude squark masses up to 550 GeV in this model at the 95% CL.

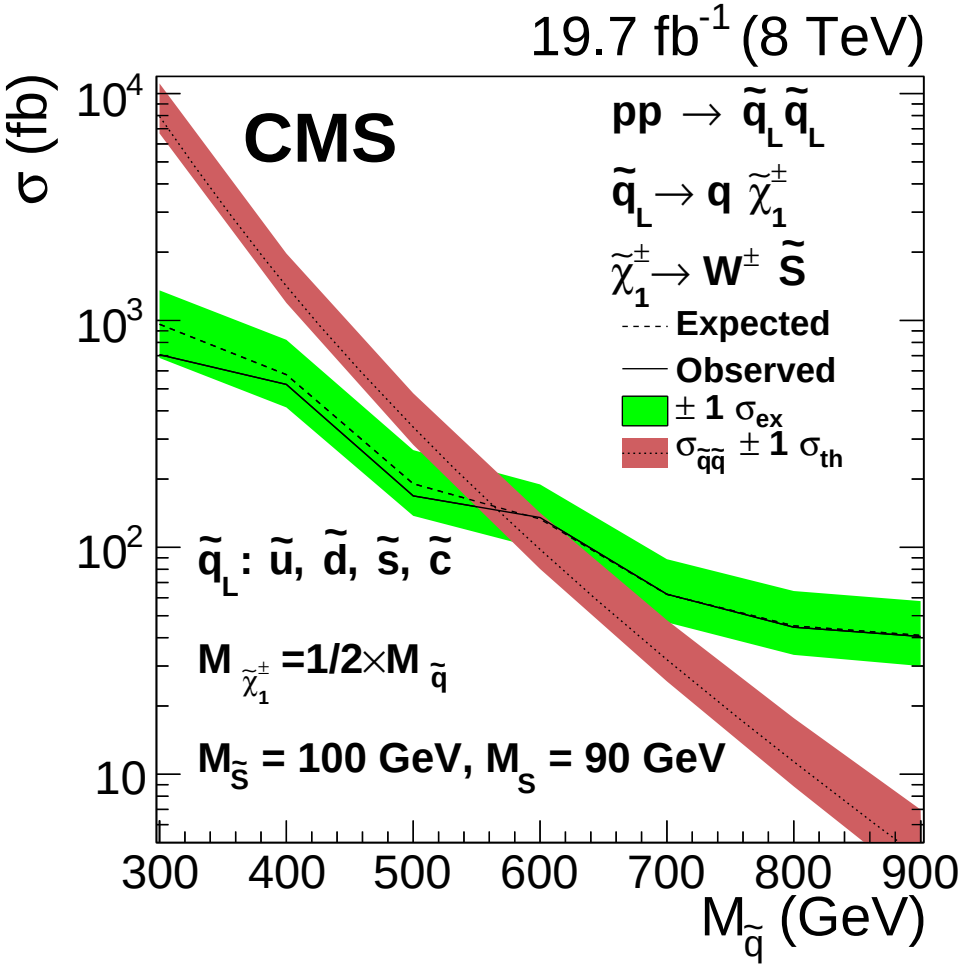

Figure 4.10: Observed and expected 95% CL upper limits on the squark production cross section as a function of the squark mass for stealth SUSY. In addition, the theoretical cross section is depicted for squark production.

4.8.2 Supplemental distributions: S_{T}

Figures 4.11–4.13 compares the S_{T} distributions from data and MC simulation. The vertical bars on the data points are the statistical uncertainty, and the hashed band shown in each figure shows the systematic uncertainty. The dominant systematic uncertainties are derived from the variation of the renormalization and factorization scale by a factor of 2(0.5). They demonstrate that the MC simulation does an excellent job describing the backgrounds in this analysis.

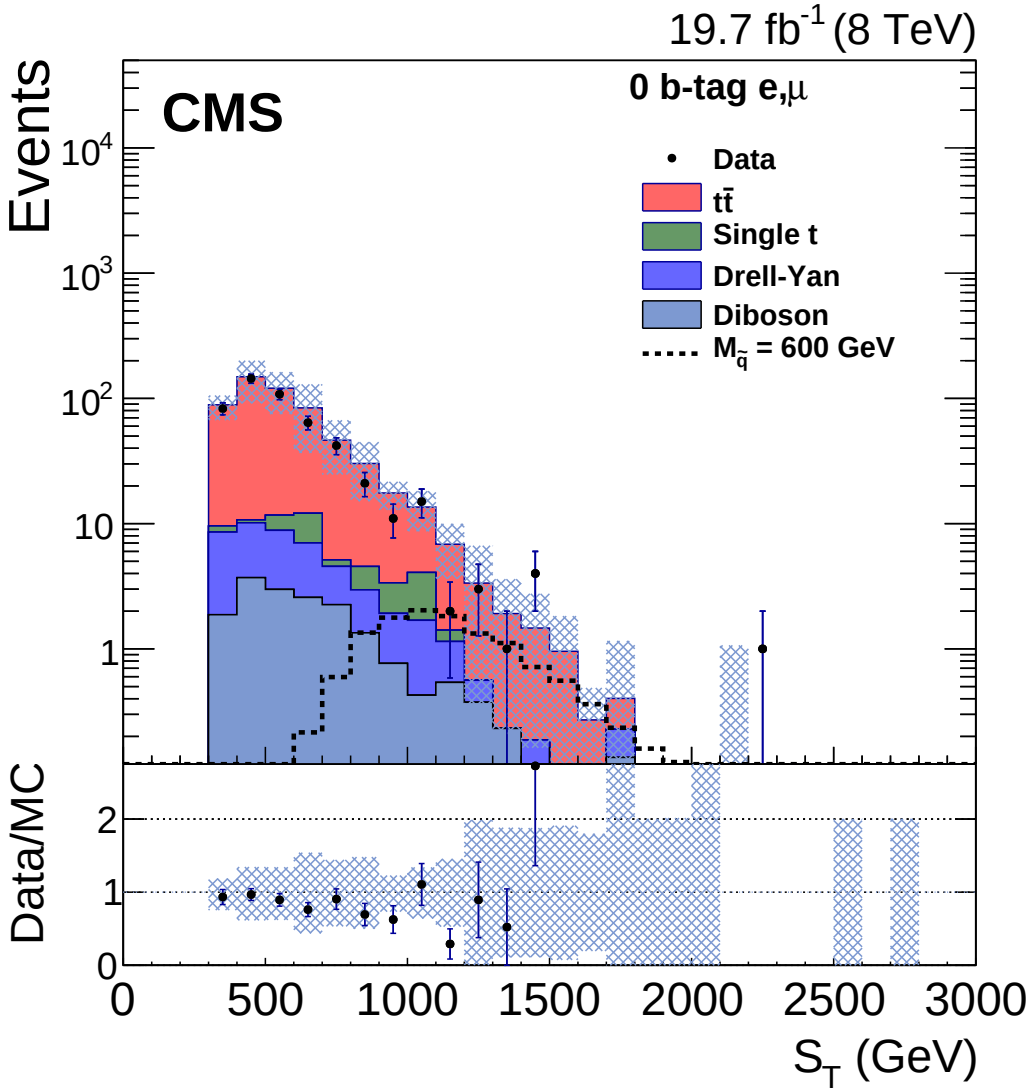

Figure 4.11: Comparison of the S_{T} distributions from data (points) and from MC simulation (histograms) for e,μ events with $\geq$ 4 jets and 0 b-tagged jets. The lower plots show the ratio of the data to the MC simulation distributions in each bin.

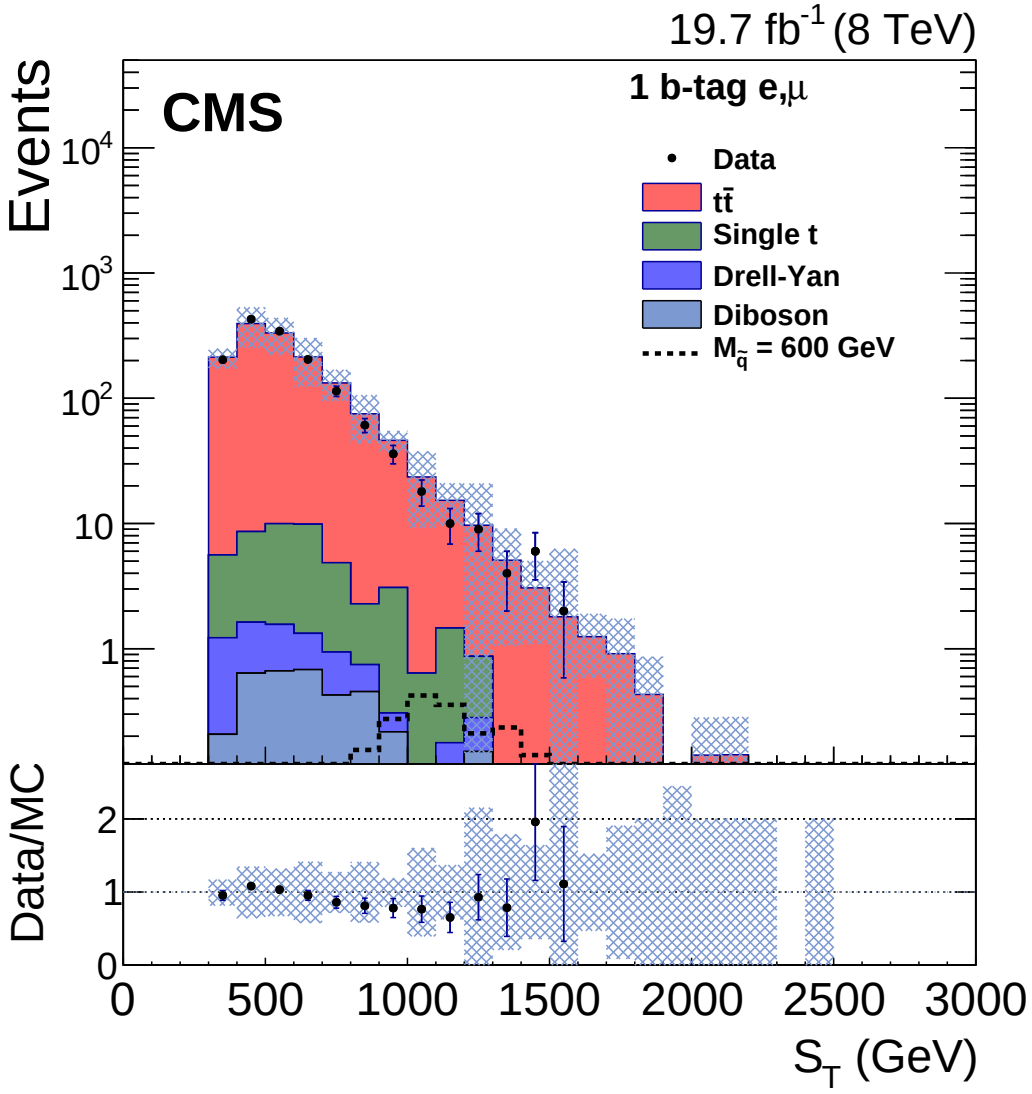

Figure 4.12: Comparison of the S_{T} distributions from data (points) and from MC simulation (histograms) for e,μ events with $\geq$ 4 jets and 1 b-tagged jet. The lower plots show the ratio of the data to the MC simulation distributions in each bin.

4.8.3 Supplemental distributions: $E_{\mathrm{T}}^{\mathrm{miss}}$

Figure 4.14– 4.16 compares the $E_{\mathrm{T}}^{\mathrm{miss}}$ distributions from data and MC simulation. The vertical bars on the data points are statistical uncertainty and the hashed bands are the systematic uncertainties. These plots demonstrate that there is not an excess of events with substantial $E_{\mathrm{T}}^{\mathrm{miss}}$.

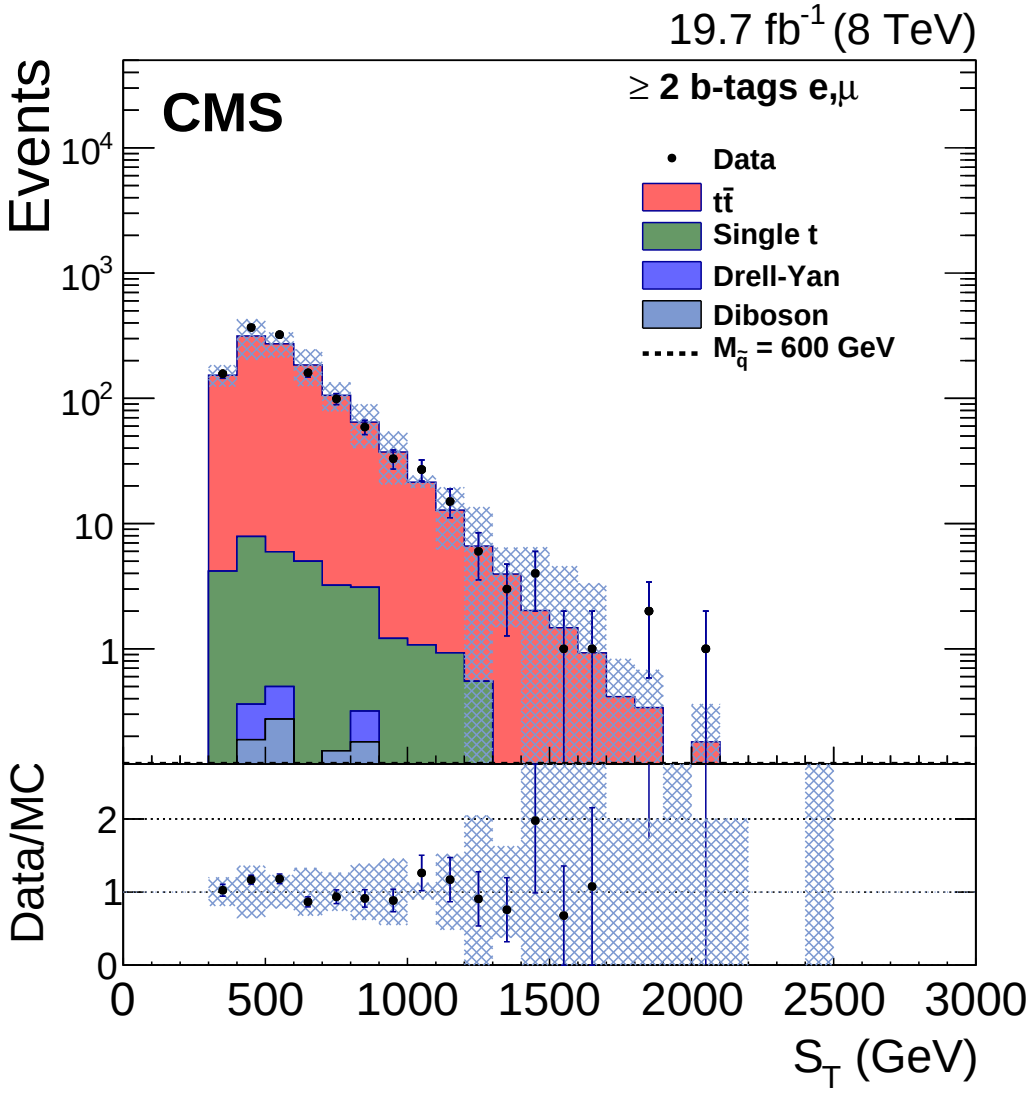

Figure 4.13: Comparison of the S_{T} distributions from data (points) and from MC simulation (histograms) for e,μ events with ≥ 4 jets and ≥ 2 b-tagged jets. The lower plots show the ratio of the data to the MC simulation distributions in each bin.

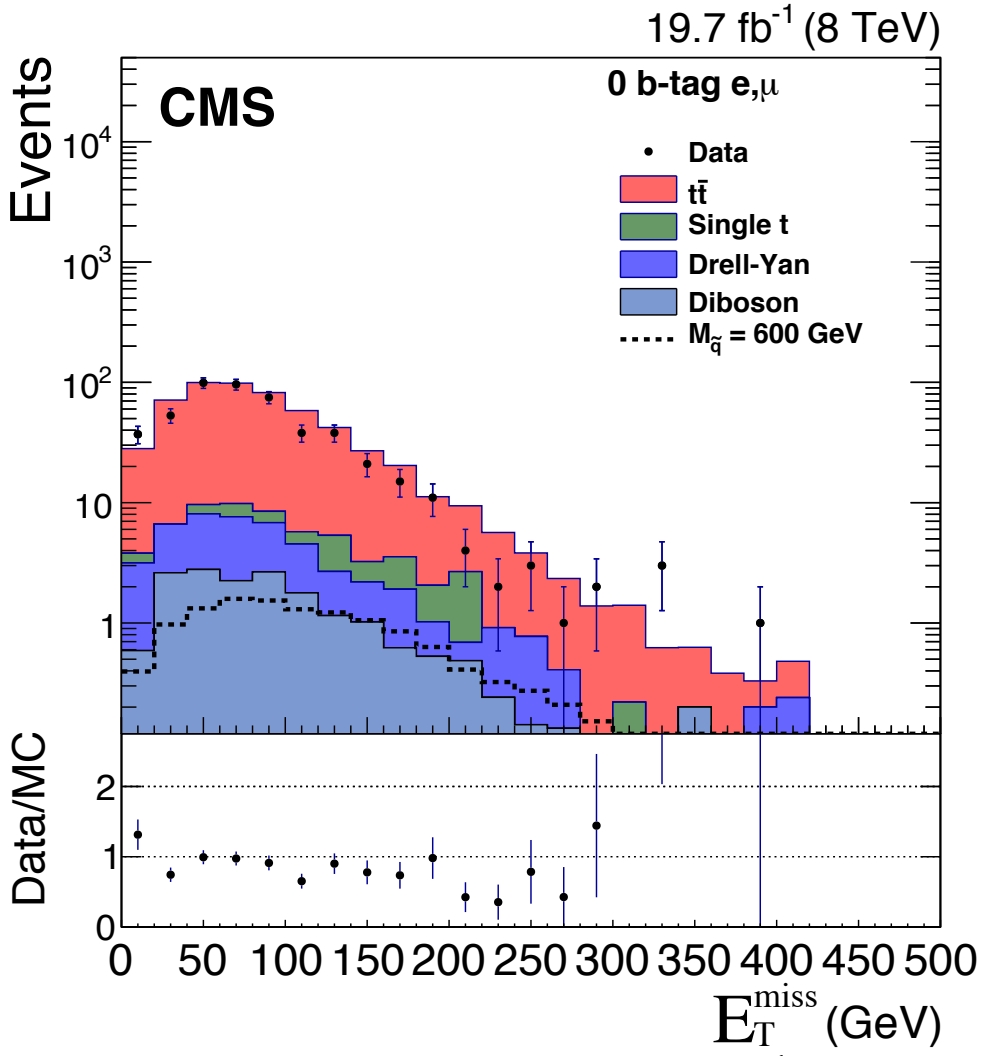

Figure 4.14: Comparison of the $E_{\mathrm{T}}^{\mathrm{miss}}$ distributions from data (points) and from MC simulation (histograms) for e,μ events with $\geq$ 4 jets and 0 b-tagged jets. The lower plots show the ratio of the data to the MC simulation distributions in each bin.

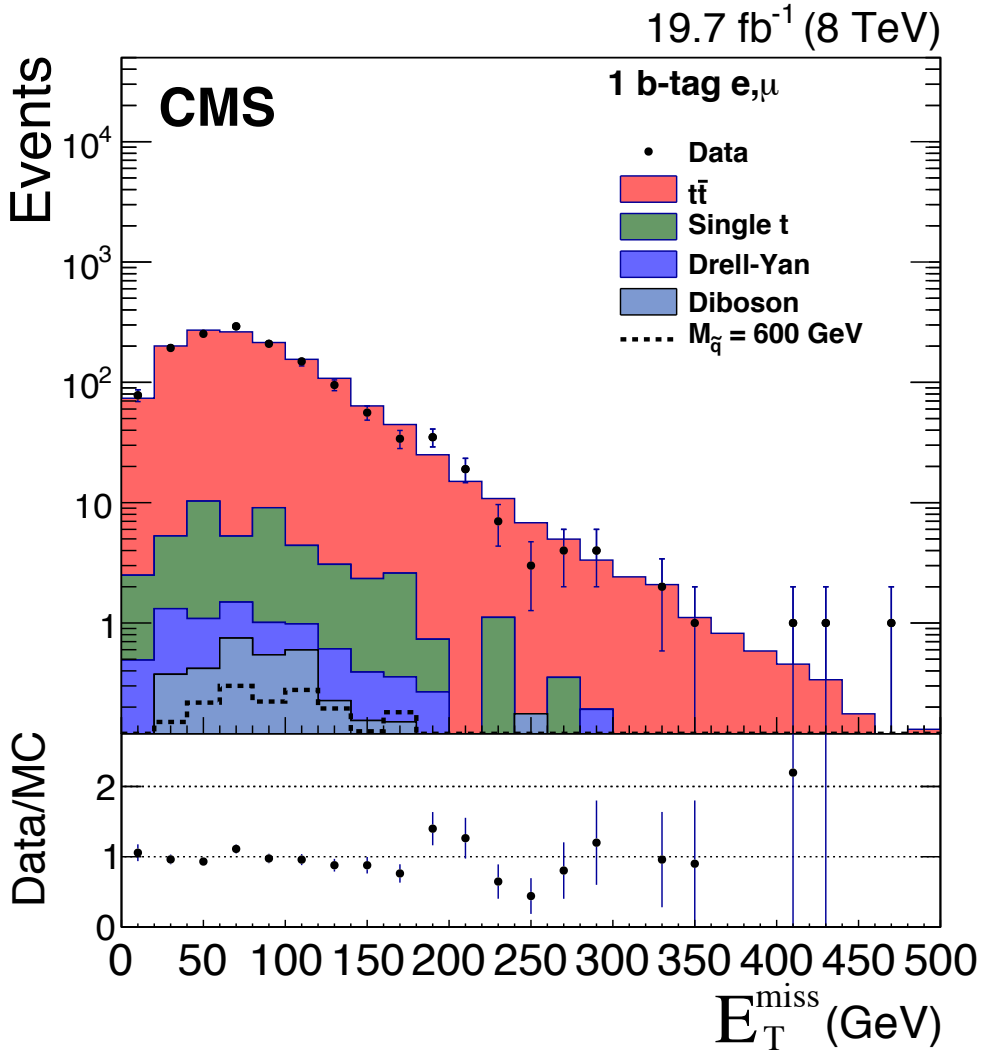

Figure 4.15: Comparison of the $E_{\mathrm{T}}^{\mathrm{miss}}$ distributions from data (points) and from MC simulation (histograms) for e,μ events with $\geq$ 4 jets and 1 b-tagged jet. The lower plots show the ratio of the data to the MC simulation distributions in each bin.

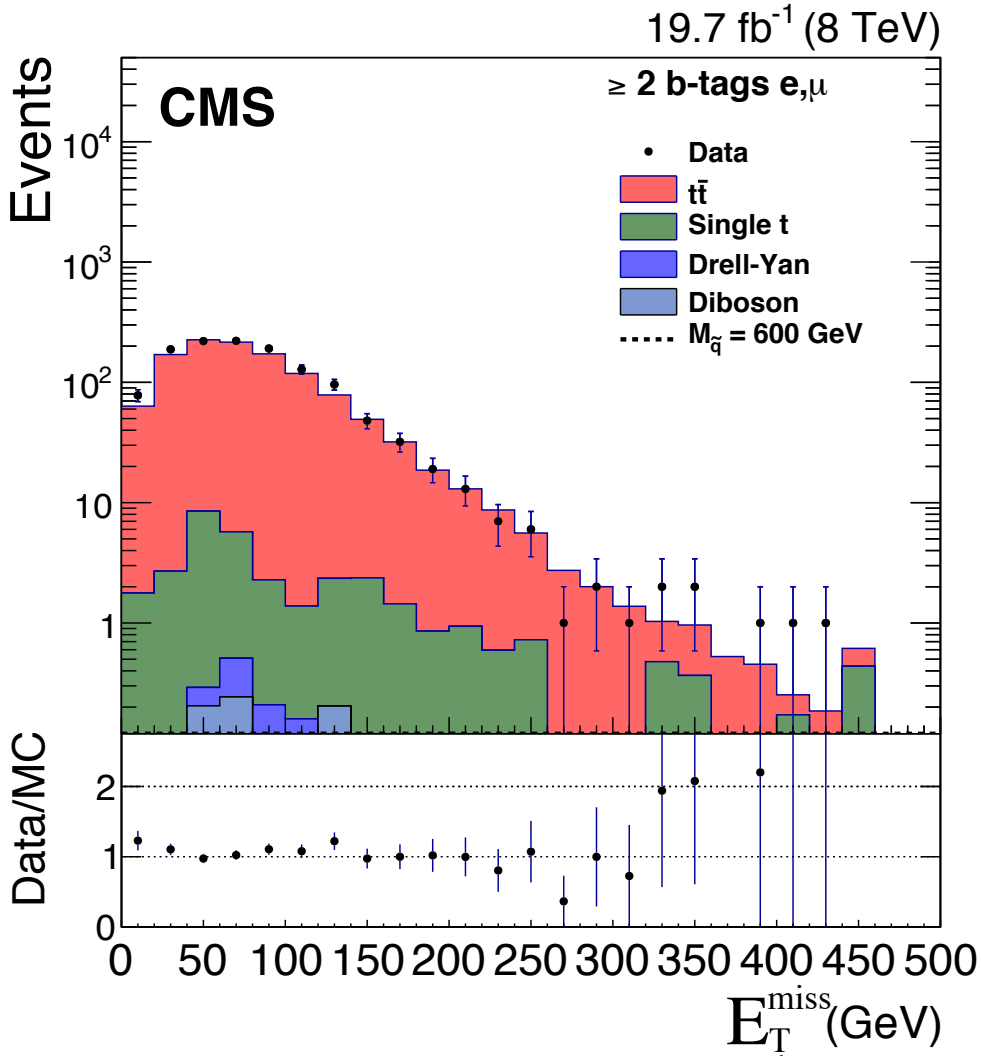

Figure 4.16: Comparison of the $E_{\mathrm{T}}^{\mathrm{miss}}$ distributions from data (points) and from MC simulation (histograms) for e,μ events with ≥ 4 jets and ≥ 2 b-tagged jets. The lower plots show the ratio of the data to the MC simulation distributions in each bin.

Chapter 5

Measurements of the $\Upsilon(1S)$, $\Upsilon(2S)$, and $\Upsilon(3S)$ cross sections

5.1 Introduction and analysis overview

As described in Section 2.2, measurements particularly at high-p_{T} of the Υ decays provide a way to study the QCD related to hadronization of heavy-quarks. The LHC data taken at $\sqrt{s} = 7\,\mathrm{TeV}$ corresponding to an integrated luminosity of $4.9\,\mathrm{fb}^{-1}$ provide a large sample of Υ events, as depicted in Fig. 5.1 and Fig. 5.2. There are approximately 413,000 $\Upsilon(1S)$ events, 152,000 $\Upsilon(2S)$ events, and 111,000 $\Upsilon(3S)$ events, which allows a measurement of the cross section even at high-p_{T}. This section will describe the measurement of the $\Upsilon(n\mathrm{S})$ (n=1,2,3) cross sections using the decay to two muons.

The $\Upsilon(n\mathrm{S})$ differential cross section times dimuon branching ratio integrated over rapidity interval $\Delta|y|$ (abbreviated as y) in a given p_{T} bin of width Δp_T is

$$\left.\frac{d\sigma\left(pp \to \Upsilon(\mathrm{nS})\right)}{dp_T}\right|_{\Delta|y|} \times \mathcal{B}\left(\Upsilon(\mathrm{nS}) \to \mu^+\mu^-\right) = \frac{N^{\mathrm{fit}}_{\Upsilon(\mathrm{nS})}}{L_{int} \cdot \Delta p_T \cdot \mathcal{A} \cdot \varepsilon}[p_{\mathrm{T}}, y]\,, \tag{5.1}$$

where $N^{\mathrm{fit}}_{\Upsilon(\mathrm{nS})}$ is the number of $\Upsilon(nS)$ events in a p_{T} bin of width Δp_{T} and rapidity bin $\Delta|y|$, ε the reconstruction efficiency averaged over the bin, L_{int} the integrated luminosity, and $\mathcal{A}(p_T)$ the polarization-corrected acceptance. Each of these terms will be explained in detail in the following sections.

The number of signal events was extracted using a fit to the data in (p_{T}, y) bins which will be discussed in Section 5.5. Signal shapes were determined using a data-driven procedure determined from the generator-level dimuon invariant mass distribution after final-state radiation and the mass uncertainty distribution is determined from data. The background for this analysis comes from a variety of sources, for example, B meson decays and Drell-Yan. We use a parametrization of Chebyshev polynomials or exponentials to describe the background shape. Since the maximum Chebyshev order (or more precisely the number of free parameters) is not a priori

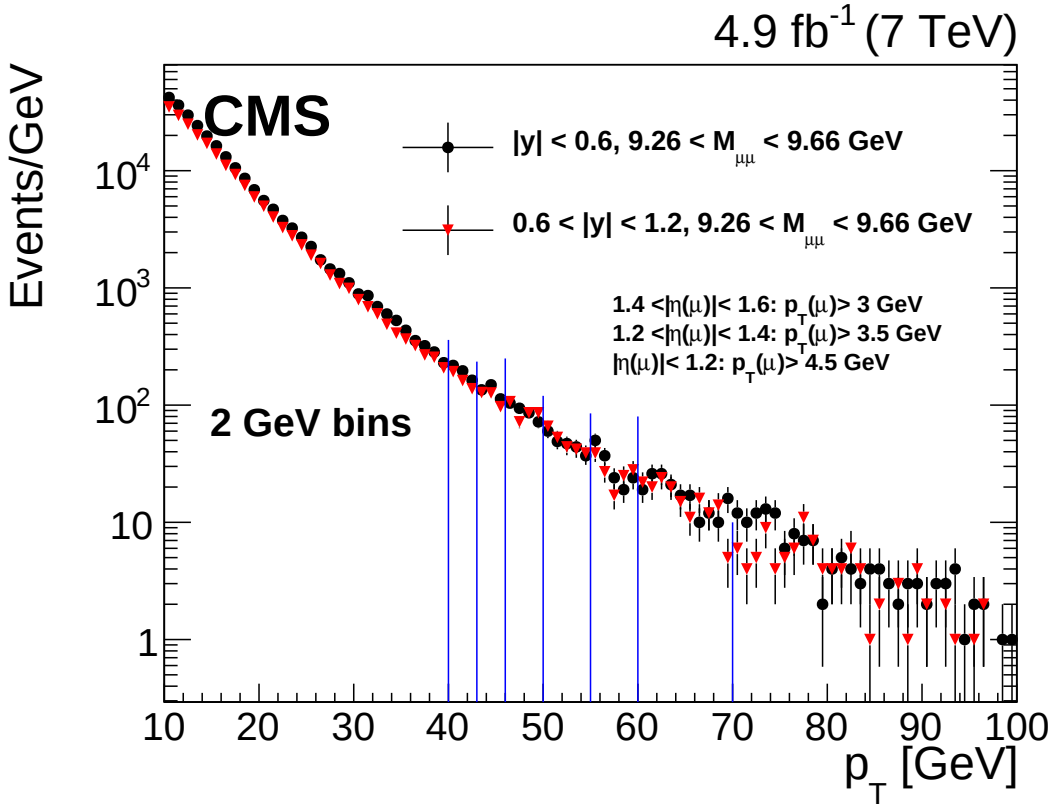

Figure 5.1: The dimuon invariant mass distribution for both rapidity ranges integrated over p_{T} for the selections listed in this Section. The vertical lines show the signal regions in the data, a 400 MeV mass range for the $\Upsilon(1S)$ state and 200 MeV for the $\Upsilon(2S)$ and $\Upsilon(3S)$.

known, we implement a procedure to determine the "best" background shape. In addition to fitting for the signal yields, we made a second fit to compute directly the ratio r_{n1}^{fit}, automatically accounting for fitting correlations. We then compute the efficiency and acceptance corrected ratio, as shown in Eq. 5.2.

$$R_{n1}[p_{\mathrm{T}}, y] = r_{n1}^{fit} \cdot \frac{A_{1S}}{A_{nS}} \cdot \frac{\varepsilon(1S)}{\varepsilon(nS)}[p_{\mathrm{T}}, y]. \tag{5.2}$$

The dimuon acceptance is the fraction of dimuons for which both muons have the minimum p_{T} and $|\eta|$ criteria, as will be discussed in Section 5.4. This quantity is computed from simulation. Since the polarization changes the angular distribution of the muons, we correct the acceptance using weights determined from the measured polarization parameters. The dimuon efficiency is computed using data and MC simulation.

The cross section and ratios of the cross sections are calculated in two bins with $|y| < 0.6$ and $0.6 < |y| < 1.2$. To determine whether there is a shift in the p_{T}-

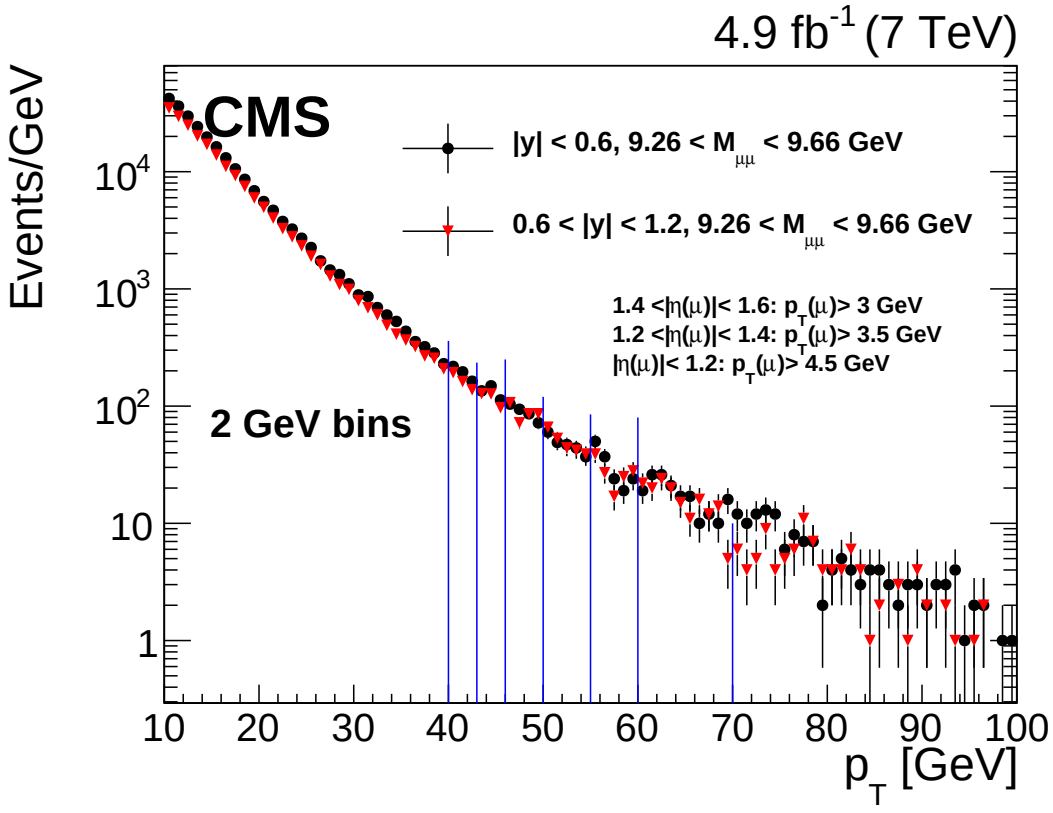

Figure 5.2: The p_{T} distribution for both rapidity ranges for a 400 MeV mass range around the $\Upsilon(1S)$peak. The vertical lines show the bin boundaries for $p_{\mathrm{T}} > 40$ GeV. Below that, bin widths are 2 GeV.

dependence of the cross section, we fit the cross sections to exponential and power-law forms for low and high p_{T} regions, respectively.

5.2 Data, trigger and object selection

Data used for the measurement of the Υ cross sections was 4.9 fb^{-1} of 7 TeV pp collisions, recorded in 2011. We use a dedicated Υ trigger, which uses HLT information from both the muon chambers and the tracking system. The trigger requires at least two muons with dimuon rapidity $|y|$ less than 1.25, p_{T} greater than 5-9 GeV (depending on the luminosity), dimuon invariant mass between 8.5 and 11.5 GeV and the fit to the dimuon vertex must have a χ^2 probability of greater than 0.5%. The trigger selects only muons that bend away from each other in the magnetic field ("seagulls"), which is implemented by requiring that $\phi(\mu^+) - \phi(\mu^-) < 0$. Requiring that muons do not cross in the transverse plane improves the determination of the muon efficiency.

Offline we require that $|y| < 1.2$ and the vertex fit must have a χ^2 probability

greater than 1%. We require that the muons meet the standard CMS quality requirements for low p_{T} muons. The muon tracks are required to have at least ten hits in the silicon tracker, at least one hit in the silicon pixel detector, and be matched with at least one segment of the muon system. The muon track fit quality must have a χ^2 per degree of freedom of less than 1.8. The distance of the track from the closest primary vertex must be less than 15 cm in the longitudinal direction and 3 cm in the transverse direction. Reconstructed muons have the following p_{T} thresholds depending on the muon $|\eta|$:

$$\begin{gathered} p_{\mathrm{T}}(\mu) > 3\,\mathrm{GeV} \text{ for } 1.4 < |\eta(\mu)| < 1.6, \\ p_{\mathrm{T}}(\mu) > 3.5\,\mathrm{GeV} \text{ for } 1.2 < |\eta(\mu)| < 1.4, \\ p_{\mathrm{T}}(\mu) > 4.5\,\mathrm{GeV} \text{ for } |\eta(\mu)| < 1.2\ . \end{gathered} \tag{5.3}$$

5.3 Efficiency

The total efficiency to reconstruct an Υ event is given by:

$$\varepsilon = \varepsilon_{\mu\mu} \cdot \varepsilon_{\mathrm{sg}} \cdot \varepsilon_{\mathrm{vp}}, \tag{5.4}$$

where $\varepsilon_{\mu\mu}$ is the dimuon efficiency (including the effect of the trigger and muon identification), $\varepsilon_{\mathrm{sg}}$ the seagull efficiency and $\varepsilon_{\mathrm{vp}}$ the efficiency of the vertex probability requirement. The seagull efficiency is determined only by whether the muons bend toward or away from each other in the magnetic field. The efficiency $\varepsilon_{\mathrm{sg}} = 0.5$, and determined from the MC simulation. The efficiency to reconstruct a vertex is 0.99 ± 0.01. This is determined from MC simulation and validated in data using a dedicated trigger without the vertex requirement.

The determination of $\varepsilon_{\mu\mu}$ is the most involved, as it includes contributions from the trigger and muon selections and must be understood using data as well as simulation. In CMS, the trigger efficiency for muons is typically measured using the tag-and-probe procedure (see [58] for further details on the procedure). A dedicated trigger requires a single muon and one additional opposite-charge track that makes a vertex. The effective mass of the pair is consistent with the J/ψ mass, then the track is tagged as a muon candidate. The faction of muon candidates that are fully reconstructed as muons can be used to determine the muon efficiency. Mass sideband events are used to subtract background from accidental muon-track overlaps. The total efficiency, in the absence of correlations between the muons is then the product of the two individual muon efficiencies. For this analysis, the focus is on Υ events with high p_{T}. As the Υ becomes boosted, the spatial separation between the muons can be reduced enough to cause the muons to be merged by the trigger, which decreases the efficiency. This effect is called the ρ factor. The final dimuon efficiency is then given by,

$$\varepsilon_{\mu\mu} \equiv \varepsilon_1[p_T(\mu_1), \eta(\mu_1)] \cdot \varepsilon_2[p_T(\mu_2), \eta(\mu_2)] \cdot \rho, \tag{5.5}$$

where $\varepsilon_{1,2}[p_T(\mu_1), \eta(\mu_{1,2})]$ are the muon efficiencies depicted in Fig. 5.3, measured using tag-and-probe for each muon (labeled 1,2) as a function of p_{T} and $|\eta|$.

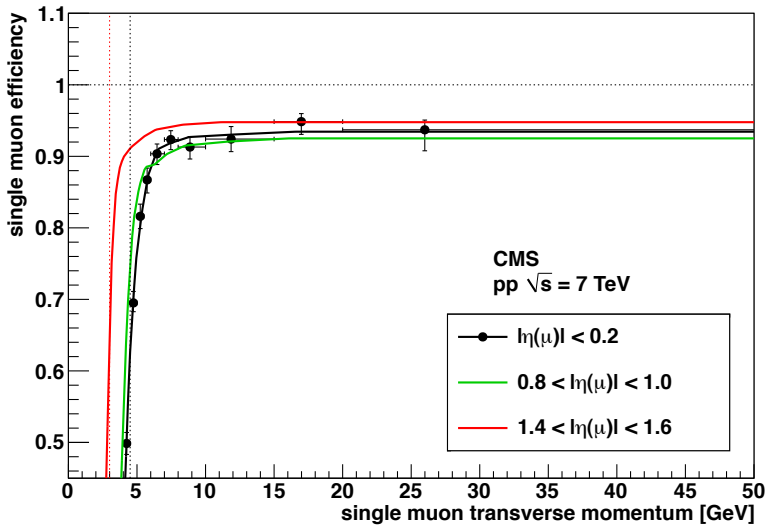

Figure 5.3: The efficiency to reconstruct a single muon as a function of muon p_{T}.

The parameter ρ is calculated in terms of $\Delta R^{elliptic}_{\Delta p_{\mathrm{T}}}$,

$$\Delta R^{elliptic}_{\Delta p_{\mathrm{T}}} = \sqrt{(0.00157\Delta p_{\mathrm{T}})^2 + (\Delta\eta)^2 + (1.2\Delta\phi)^2}. \tag{5.6}$$

This parameterization is chosen because $\Delta R^{elliptic}_{\Delta p_{\mathrm{T}}}$ drops rapidly for values less than about 1, as expected due to the fact that the muons are close together in the detector. We compute the ρ factor in both simulation and data. To compute the ρ factor in simulation, we simply rearrange Eq. 5.5 to the form:

$$\rho(\Delta R^{elliptic}_{\Delta p_{\mathrm{T}}}, y) = \frac{N_{MC}(\Delta R^{elliptic}_{\Delta p_{\mathrm{T}}}, y|PS\,\&\,\mathrm{qual}^{\mu}\,\&\,\mathrm{trigger})}{N_{MC}(\Delta R^{elliptic}_{\Delta p_{\mathrm{T}}}, y|PS)} \frac{1}{\varepsilon_{MC}[p_T(\mu_1), \eta(\mu_1)] \cdot \varepsilon_{1,2}[p_T(\mu_2), \eta(\mu_2)]}, \tag{5.7}$$

where PS means both muons satisfy Eq. 5.3, qual^{μ} means that the muons in the numerator pass the muon quality selections and trigger means that the event passed the trigger. The efficiency terms $\varepsilon_{1,2}$ are determined from the tag-and-probe procedure described above. To measure the ρ factor we obtain a sample of muons using a single muon trigger with a p_{T} threshold of 24 GeV. Because this sample contains at least one muon, this sets $\varepsilon[p_T(\mu), \eta(\mu)]$ of the leading p_{T} muon to 1. To estimate the number of Υ events in the numerator and denominator of Eq. 5.7, we perform a crude background subtraction by fitting the side band regions (8.5–9.2 and 10.6–11.5 GeV) to a first order polynomial. Figure 5.4 shows the ρ factor measurements in both simulation and data.

For each measurement (p_{T}, y) bin, we compute the average efficiency of events in the data using Eq. 5.5 for each $\Upsilon(n\mathrm{S})$ state, averaged over the mass regions listed in Table 5.1. The average efficiency for the $\Upsilon(1S)$ state is shown in Fig. 5.5.

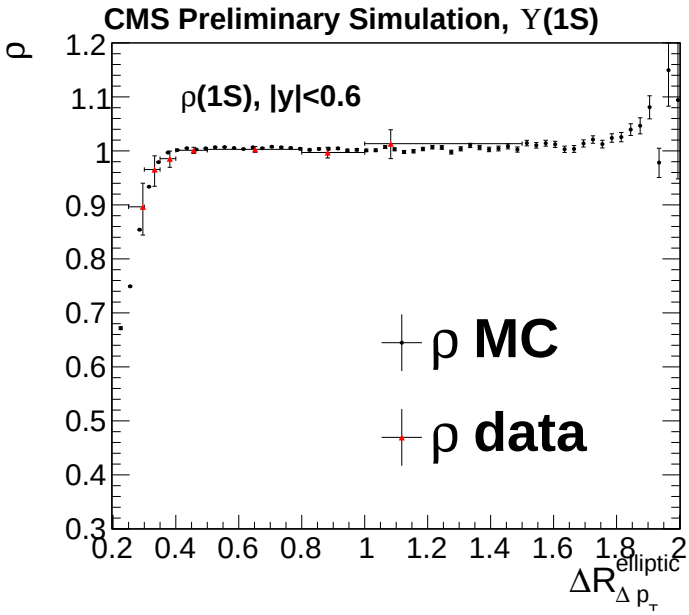

Figure 5.4: The ρ factor measured in MC simulation for $\Upsilon(1S)$ events with p_{T} in the range 10–100 GeV compared with ρ factor measurements from data.

Table 5.1: Mass ranges used for computing the average dimuon efficiency for each state.

	$\Upsilon(1S)$	$\Upsilon(2S)$	$\Upsilon(3S)$
Mass Range [GeV]	9.26< $M_{\mu\mu}$ <9.66	9.92< $M_{\mu\mu}$ <10.12	10.255< $M_{\mu\mu}$ <10.455
Abbreviation	M1	M2	M3

5.4 Acceptance

The acceptance is the ratio of the number of polarization-weighted Υ decays where the muons satisfy Eq. 5.3 to the total number of weighted events in a given (p_{T}, y) bin:

$$\mathcal{A}(p_T, y) = \frac{N_{MC}(p_T, y|\text{muon pair satisfying Eq. 5.3}; w)}{N_{MC}(p_T, y; w)}. \tag{5.8}$$

The acceptance is only computed given a set of seagull dimuons. For a given p_{T} bin, we compute the event weight w from the measured polarization parameters:

$$w = \frac{3/(4\pi)}{3+\lambda_\theta}\left(1 + \lambda_\theta \cos^2\theta + \lambda_\phi \sin^2\theta \cos 2\phi + \lambda_{\theta\phi} \sin 2\theta \cos\phi\right), \tag{5.9}$$

where $\lambda_\theta, \lambda_\phi, \lambda_{\theta\phi}$ are the polarization parameters that were measured in a CMS analysis up to a p_{T} of 50 GeV [119] in the center of mass helicity (HX) frame, where the Upsilon momentum defines the polar axis [120]. The polar angle θ and azimuthal

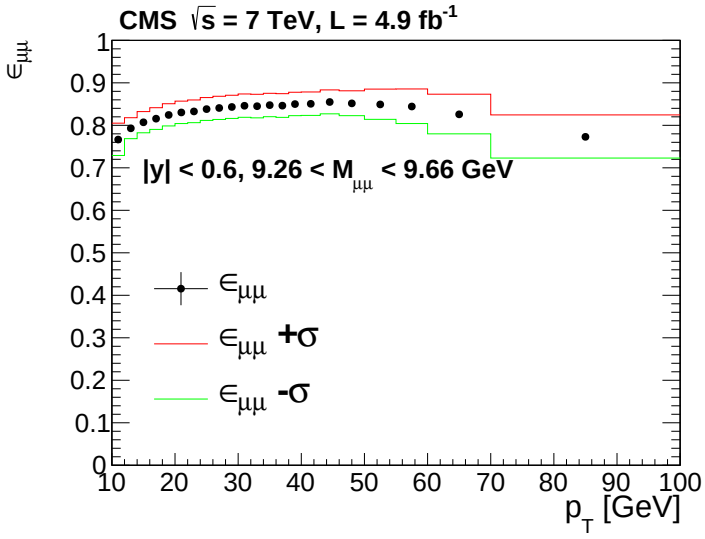

Figure 5.5: The p_{T} variation of average $\overline{\epsilon_{\mu\mu}}$ and the uncertainties due to $\pm 1\sigma$ variations in the single muon efficiencies and ρ factor for data, averaged over mass range M1.

angle ϕ are defined for the positive lepton using the HX axes. The angular correction w is used to reweight the unpolarized distribution to account for polarization effects. Since the polarization parameters are measured in coarser p_{T} bins than the cross section measurement, we perform a linear interpolation between the measured points. To extrapolate beyond $p_{\mathrm{T}} = 50\,\mathrm{GeV}$, we use the average of the measured polarization with $p_{\mathrm{T}} < 50$ GeV to create a point at $p_{\mathrm{T}} = 65$ GeV, which is the mean p_{T} of the data with p_{T} between 50–100 GeV. The same procedure is performed to extrapolate the 68.3% CL uncertainties. The resultant overlay of the interpolated and extrapolated polarization parameter λ_θ is depicted in the left-hand portion of Fig. 5.6.

The right plot of Fig. 5.6 shows the p_{T}-variation of the acceptance using the interpolated polarization parameters and its changes in each p_{T}-bin when the polarization parameters are shifted up or down by the interpolated 68.3% CL bounds. A comparison of the acceptance computed with the measured polarization to the fully transverse or longitudinal polarization in Fig. 5.6 clearly illustrates the reduction in systematic uncertainty that can be attained by using the measured polarization to compute the acceptance.

We evaluate the acceptance calculation using kinematics from the generator-level muons. To check the impact of this assumption on the acceptance we ensured that the finite reconstruction resolution of muons does not change the accepted fraction of muons by more than 2%. This justifies the use of generator-level kinematics.

We then evaluated the impact of the flat Υ p_{T} distribution of the simulated sample on the acceptance. Initially to compute the cross section, we used the average acceptance in each p_{T} bin. We then performed an additional iteration, where we reweight

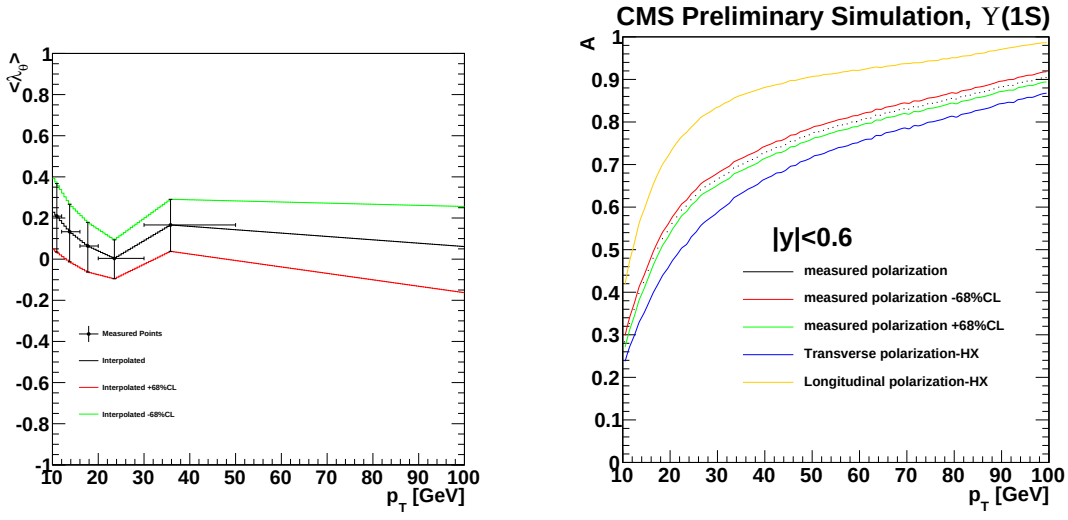

Figure 5.6: Left: Measured and extrapolated λ_θ parameters for the Υ(1S) in the HX frame and the 68.3% CL bars. Right: $\Upsilon(1S)$ acceptance as a function of dimuon p_{T} for $|y| < 0.6$. The green(red) error bands show the effects of moving all parameters up (down) by one-standard deviation as described in the text. The solid yellow and blue curves show the acceptance assuming the extreme case of fully transverse or fully longitudinal polarization.

the acceptance according to the measured p_{T} spectrum. This weight was computed using a fit of the data to a parameterization (see Section 5.7). The acceptance was recomputed based on the following expression: $\bar{A}(p_T) = \frac{\sum_i^N A_i f(\bar{p}_T)_i}{\sum_i^N f(\bar{p}_T)_i}$, where A_i was evaluated in 1 GeV p_{T} bins, and the fit function was evaluated at the center of the 1 GeV bin. The largest deviation between the two iterations occurred in the 70-100 GeV bin and was less than 1.5%.

5.5 Yield fitting procedure

To determine the number of Υ events in the selection we fit the dimuon invariant mass distribution with a signal and background model. Typically in cross section measurements the Υ signal shape is parameterized with a crystal ball function, which consists of a Gaussian core and a power-law at low mass to account for the final-state radiation (FSR) effects [121]. There are four adjustable parameters for a crystal ball function, which either have to be determined from the fit or fixed from some other procedure (e.g., simulation). We reduce the number of free parameters using a signal model based on data.

The dimuon signal shape is dominated by the finite resolution of the detector, and the radiation of a photon from one of the muons. Photon radiation tends to

shift the dimuon mass distribution to the left of the Upsilon peak, as depicted by Fig. 5.7 (left). FSR was simulated using PHOTOS, which has a fixed photon energy threshold 1% of half the mass of the decaying particle (about 50 MeV depending on the Upsilon state), which can clearly be seen in Fig. 5.7. This was too large for this analysis, and we extended the photon energy range down to 2 MeV by fitting the tail of the distribution to the expression for final state radiation in the PHOTOS documentation [122, 123], as shown in Fig. 5.7.

The signal shape for a muon measured by a detector with finite momentum resolution results from taking Fig. 5.7 and including a finite resolution for each muon, effectively giving a mass uncertainty to each event. To account for this effect, we compute the mass uncertainty distribution for each (p_{T},y) bin in data, as depicted in Fig. 5.7 right. The double peaking structure observed in this figure results from the combination of several muon $|\eta|$ bins. The mass resolution is worse for events where higher $|\eta|$ is required since muons pass through more material.

The determination of the normalized lineshape $\mathcal{F}(M_{\mu\mu}; c_w, \delta m)$ as a function of dimuon mass $M_{\mu\mu}$ is determined by evaluating the following expression:

$$\mathcal{F}(M_{\mu\mu}; c_w, \delta m) = \frac{1}{N}\sum_{i=1}^{N} \frac{1}{\sqrt{2\pi}c_w\zeta_i} e^{-(M_{\mu\mu}-m_i-\delta m)^2/2c_w^2\zeta_i^2}, \tag{5.10}$$

where N=25,000, and m_i is randomly sampled from Fig. 5.7 (left) and ζ_i randomly sampled from Fig. 5.7 (right). Parameters c_w and δm are nuisance parameters, which account for an overall mis-measurement of the momentum resolution scale, and δm allows for a mis-measurement in the absolute momentum scale between data and

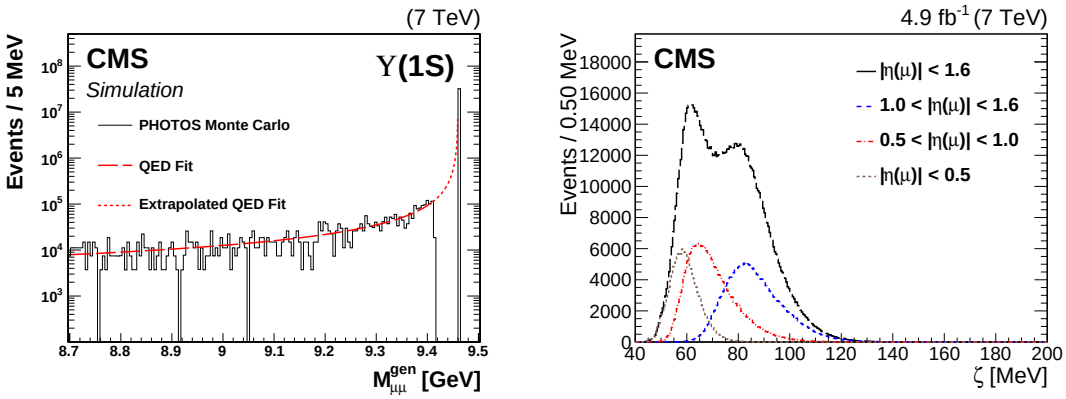

Figure 5.7: Left: generator-level dimuon invariant mass distribution. The red line shows the fit to the data, and the extrapolation between 9.4–9.46 GeV. Right: plot showing the mass resolution for several $|\eta(\mu)|$ bins, which produces the structure seen in the overall ζ distribution for a given (p_{T}, $|y|$) bin. Note that the muon $|\eta(\mu)|$ selections apply to both muons, so the histograms with tighter muon selections do not sum up to the histogram of $|\eta(\mu)|$ <1.6 (top contour).

simulation. Three sample lineshape curves are depicted in Fig. 5.8, with various c_w and δm values. The parameters apply to the entire mass distribution, not to each peak separately.

To validate that the lineshape procedure works, we took the simulation sample, and split it into 50 equal parts. Using 1 part, we generated a sample lineshape, which we then used to fit the remaining 49 samples. The fits show that the lineshape describes the simulation.

We perform a simultaneous maximum-likelihood fit of signal and background using the following expressions:

$$N(M_{\mu\mu}) = N_1\mathcal{F}(M_{\mu\mu};c_w,\delta m)_{\Upsilon(1S)} + N_2\mathcal{F}(M_{\mu\mu};c_w,\delta m)_{\Upsilon(2S)} + N_3\mathcal{F}(M_{\mu\mu};c_w,\delta m)_{\Upsilon(3S)} + B\sum_{i=0}^{n_{max}} b_i T_i \tag{5.11}$$

where $N_{1,2,3}$ is the number if signal events for each Υ state. The last term in the sum describes the background, where B is the background normalization. The background is a modeled as a series of Chebychev polynomials T_i, each with coefficient b_i. We also use the following parametrization to compute the ratio of yields r_{21}, r_{31} normalized

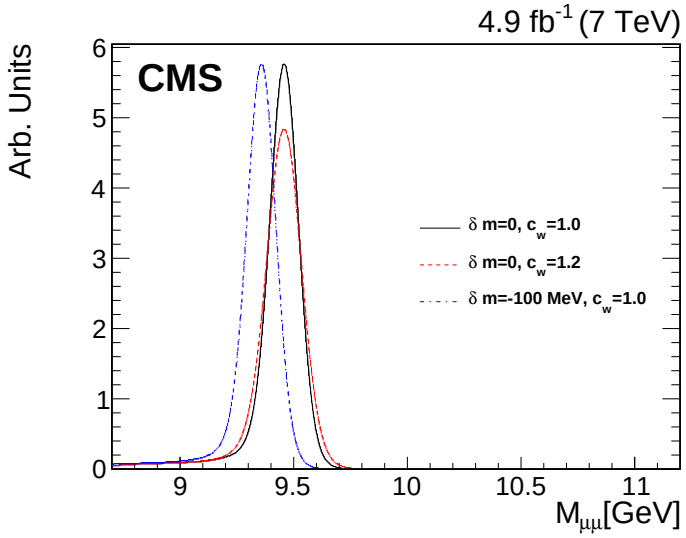

Figure 5.8: Data-driven lineshape for the $\Upsilon(1S)$ in the p_{T} bin 10–12 GeV (black curve). The red curve shows the lineshape function with the same ζ distribution, but with width scale factor $c_w = 1.2$ and no mass shift. The blue curve is the lineshape function evaluated with unit width scale factor, but $\delta m = 100$ MeV.

to the $\Upsilon(1S)$yield, automatically including correlations:

$$N(M_{\mu\mu}) = S_1[(\mathcal{F}(M_{\mu\mu}; c_w, \delta m)_{\Upsilon(1S)} + r_{21}\mathcal{F}(M_{\mu\mu}; c_w, \delta m)_{\Upsilon(2S)} + r_{31}\mathcal{F}(M_{\mu\mu}; c_w, \delta m)_{\Upsilon(3S)}] + B\sum_{i=0}^{n_{max}} b_i T_i \tag{5.12}$$

The likelihood is defined as,

$$\mathcal{L} = \prod_i \mathcal{P}(M_{\mu\mu}; \vec{\alpha}) \tag{5.13}$$

where $\mathcal{P}(\mathcal{M}_{\mu\mu}; \vec{\alpha})$ is the probability distribution as a function of $M_{\mu\mu}$ (Eq. 5.11 or 5.12 normalized to unit area) and $\vec{\alpha}$ is the set of free parameters. In practice, the value of $\mathcal{L}$ becomes intractably large, so we instead take the natural log and evaluate the following sum:

$$ln\mathcal{L} = -\sum_i \mathcal{P}(M_{\mu\mu}; \vec{\alpha}). \tag{5.14}$$

We constrain the overall normalization to the total number of events predicted by the PDF N_{expected} to be the same as the number of data events N_{data} in that bin This is implemented using a modification to the likelihood, which then becomes:

$$ln\mathcal{L} = -\sum_i \mathcal{P}(M_{\mu\mu}; \vec{\alpha}) - log(Poisson(N_{\text{expected}}, N_{\text{data}})), \tag{5.15}$$

where the final term is determined by the Poisson distribution. The fit was performed using RooFit [124]. For p_{T} less than 50 GeV, we use a binned fit (the product in Eq. 5.13 is over bins), while for high-p_{T} we use an unbinned fit (the product in Eq. 5.13 is over events.)

As evident from Fig. 5.1, the background as a function of dimuon mass can easily be described by a polynomial series. We form a set of ansatz functions for the background from a Chebychev series terminated at $N = 2$, and an exponential (generally the slope of the fit function will be small, and this can be thought of as approximating a linear function). We implement a method to determine the best background function from this set of possible functions using the AIC [125, 126],

$$AIC_c = 2 \cdot ln(\mathcal{L})_{min} + 2 \cdot k + \frac{2k(k+1)}{n-k-1} \tag{5.16}$$

where $ln(\mathcal{L})_{min}$ is the minimum likelihood determined from the fit, k the number of free parameters, and n the number of events or bins. Finite size corrections are implemented using the term $\frac{2k(k+1)}{n-k-1}$.

For each trial function, we compute the normalized probability,

$$p_i = \frac{e^{-\Delta_i/2}}{\sum_i e^{-\Delta_i/2}} \quad \Delta_i = AIC_i - AIC_{min}, \tag{5.17}$$

which determines the probability of each background shape relative to the other fits. Table 5.2 lists some typical AIC values and probabilities for a sample fit. One of the interesting features is how the AIC tends to clearly prefer a single fit, whereas the χ^2 probability tends to be less sensitive to the background order. It is also important to note that the difference in yield between each background hypothesis is within two statistical σ. The fits are repeated for each (p_{T}, y) bin, and two of them are depicted in Fig. 5.9.

Table 5.2: $\Upsilon(1S)$ fit results for several trial background functions in the bin $|y| < 0.6$, $12 < p_T < 14\,\mathrm{GeV}$, showing the background model, yield (Y), statistical uncertainty on the yield (σ_Y, χ^2, number of free parameters (k), AIC probability (p_i) and χ^2 probability.

order	Y	σ_Y	χ^2	k	AIC	p_i	χ^2 prob
0	49098	252	303	6	-2495540	3.58e-15	0.0904
1	48852	257	289	7	-2495553	2.82e-12	0.291
2	48662	265	282	8	-2495606	1	0.47
exponential	48870	259	289	7	-2495538	1.39e-15	0.149
Yield	σ	σ_{sys}					
48662	265	191					

5.6 Systematic uncertainties

Sources of systematic uncertainties on the cross section (in roughly equal order of importance) are: acceptance (due to uncertainty on the polarization), efficiency (due

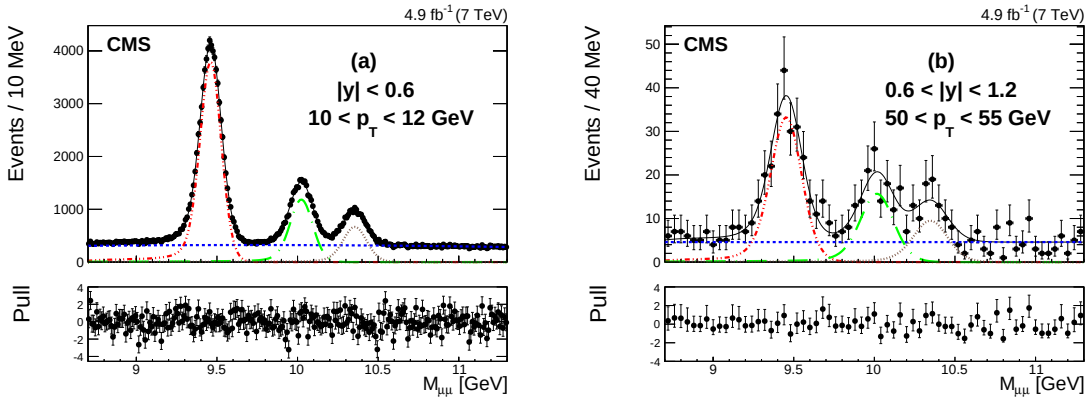

Figure 5.9: $\Upsilon(nS)$ fits with the best background function. (a) $0 < |y| < 0.6$, (b) $0.6 < |y| < 1.2$ and $50 < p_T < 55$ GeV.

to uncertainties on tag-and-probe and the ρ factor), efficiency of vertex probability requirement, luminosity, and choice of background function.

To evaluate the systematic uncertainty on the acceptance, we vary all of the polarization parameters by their 68.3% CL uncertainties (see Fig. 5.6 left). The resulting change in acceptance is depicted in the right of Fig. 5.6, and is substantially less than what the systematic uncertainty would have been if there was no knowledge of the Υ polarization.

Tag-and-probe efficiencies enter into Eq. 5.5, where each have an uncertainty [119], and the ρ factor has an uncertainty determined from the comparison to the ρ factor measured in data. The ρ factor uncertainties are summarized below:

$$\begin{array}{c} \Delta R^{elliptic}_{\Delta p_{\mathrm{T}}} \leq 0.4 \quad 5\% \\ 0.4 < \Delta R^{elliptic}_{\Delta p_{\mathrm{T}}} < 1.7 \quad 0.5\% \\ \Delta R^{elliptic}_{\Delta p_{\mathrm{T}}} > 1.7 \quad 5\%. \end{array} \tag{5.18}$$

For $\Delta R^{elliptic}_{\Delta p_{\mathrm{T}}} < 0.4$ we assign the statistical uncertainty on the data as the uncertainty in Eq. 5.18. At intermediate p_{T}, there is excellent agreement between data and simulation, so we assign a 0.5% uncertainty. At high-p_{T} we lack the data to precisely determine ρ, so we constrain ρ to 1, and assign a 5% uncertainty.

The efficiency $\varepsilon_{\mu\mu}$ is recalculated based on the mass regions in Table 5.1 as the tag-and-probe efficiencies and ρ factor are varied by their uncertainties. The changes in the efficiency result in the systematic error band depicted in Fig. 5.5.

The choice of background function is determined by the AIC procedure outlined above. To determine a systematic uncertainty for this procedure, we assign the difference in the yield between the best background choice and an alternate background function. The alternate function is the one with the largest difference from the yield calculated using the best background choice, where $p_i > 5\%$. In the case where there is no other background function with $p_i > 5\%$, we evaluate the systematic using the next best AIC value.

All of the systematics occur on variables which are multiplicative in the cross section calculation (Eq. 5.1), and are therefore added in quadrature. The cross section measurement is systematics dominated for p_{T} less than around 50 GeV. Above this p_{T} value, statistical uncertainties dominate.

Table 5.3: Summary of systematic uncertainty ranges for each source of uncertainty.

Source	Relative uncertainty (%)
acceptance	1.0-7.0
dimuon efficiency	3.1-7.0
vertex probability efficiency	1.0
luminosity	2.2
choice of background function	0.2-9.3

Based on the definition of the ratio measurement in Eq. 5.2, the systematic uncertainty on the efficiency approximately cancels. This was evaluated by computing the ratio of efficiencies for $\Upsilon(2S)/\Upsilon(1S)$ and $\Upsilon(3S)/\Upsilon(1S)$ and coherently varying the efficiencies by the uncertainties assigned. Since the acceptance is based on different, independent measurements we add the uncertainties on the acceptance from each state in quadrature.

5.7 Results and interpretation

The cross section distributions as a function of p_{T} are presented in two independent p_{T} bins: $|y| < 0.6$ and $0.6< |y| < 1.2$, as well as a combined rapidity bin with $|y| < 1.2$. Figure 5.10 shows the cross section results for all three states, where the $\Upsilon(2S)$ and $\Upsilon(3S)$ state are scaled down to facilitate comparison. Since the shape of the differential cross section seems to change shape near 20 GeV, we parametrize the cross section in two forms: an exponential for $p_{\mathrm{T}} < 20$ GeV, and a power-law for $p_{\mathrm{T}} > 20$ GeV, where the power-law has the form:

$$\frac{d\sigma}{dp_T} = \frac{A}{C + (\frac{p_T}{p_o})^{\alpha}}. \tag{5.19}$$

A, C and p_o are normalization conditions without physical significance, and α is the power-law, which is expected from theoretical expansions at high p_{T}. Fits to all three Υ states, with $|y| < 1.2$ are shown in Fig. 5.10.

Ratios of the cross sections for the different Υ state are presented in Fig. 5.11, computed using Eq. 5.2.

Table 5.4: Parameters of the power-law fits to the $\Upsilon(nS)$ distributions for $|y| < 1.2$ shown in Fig. 5.10 (b). The fits for all states begin at $p_{\mathrm{T}} = 20$ GeV.

	$\Upsilon(1S)$	$\Upsilon(2S)$	$\Upsilon(3S)$
A	13.97 ± 0.73	6.71 ± 0.46	4.50 ± 0.34
α	5.75 ± 0.07	5.65 ± 0.10	5.27 ± 0.10
C	0.46 ± 0.13	0.64 ± 0.18	0.29 ± 0.16
χ^2:	8.6	11	17
NDOF:	14	14	14
Constant	7.69 ± 0.13	6.21 ± 0.15	5.52 ± 0.17
Slope	-0.27 ± 0.01	-0.24 ± 0.01	-0.21 ± 0.01
χ^2:	0.64	0.32	0.051
NDOF:	3	3	3

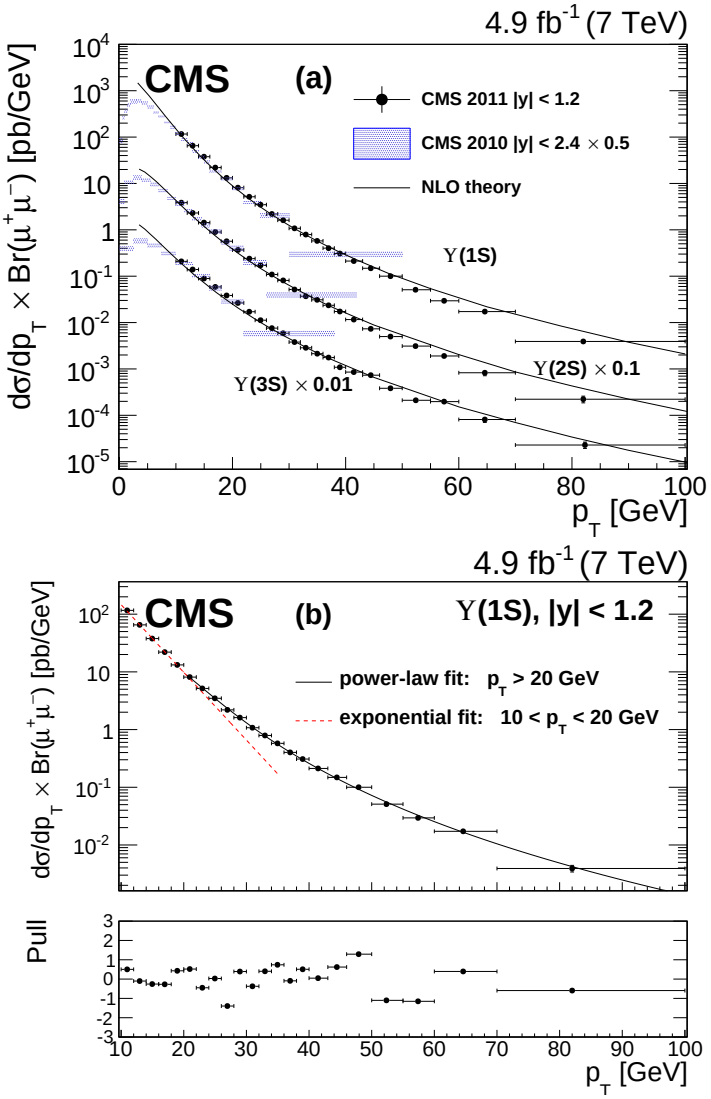

Figure 5.10: (a) The $\Upsilon(n\mathrm{S})$ differential p_{T} cross sections times dimuon branching fractions for $|y| < 1.2$. The $\Upsilon(2S)$ and $\Upsilon(3S)$ measurements are scaled by 0.1 and 0.01, respectively, for display purposes. The vertical bars show the total uncertainty, excluding the systematic uncertainty in the integrated luminosity. The horizontal bars show the bin widths. Previous CMS measurements for $|y| < 2.4$ are shown as cross-hatched areas [121]. These results have been scaled by 0.5 to account for the smaller $|y|$ range in the latest measurement, where the scaling assumes that the rapidity distribution is flat. The solid lines are the NLO calculations from Ref. [127] extended by the authors to cover the range $p_{\mathrm{T}} < 100$ GeV. (b) Details of the parametrized cross section fit described in the text for $\Upsilon(1S)$ with $|y| < 1.2$. In this plot the solid line is the result of the power-law fit (see Eq. 5.19) for $p_{\mathrm{T}} > 20$ GeV. The dashed line shows an exponential fit to the data for $10 < p_{\mathrm{T}} < 20$ GeV. The lower plot shows the pulls of the fit as defined in the text.

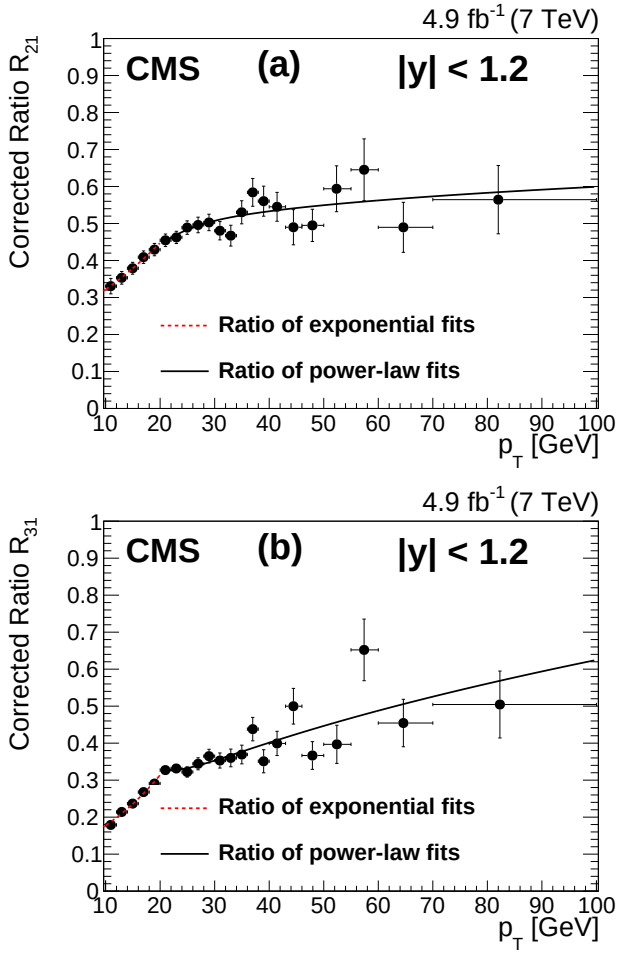

Figure 5.11: Differential cross section ratios as a function of p_{T}. (a) Ratio $R_{21} = \Upsilon(2S)/\Upsilon(1S)$; (b) $R_{31} = \Upsilon(3S)/\Upsilon(1S)$. The dashed line is the ratio of the exponential fits for $10 < p_{\mathrm{T}} < 20$ GeV. The solid line is the ratio of the power–law fits for $p_{\mathrm{T}} > 20$ GeV.

Chapter 6

Conclusions

The Run 1 of the LHC experiment was an exciting time; the center-of-mass energy exceeded the previous world record, and excellent performance of the machine and experiments allowed for a substantial data set to be collected. Included in the exciting results of Run 1 was the discovery of the Higgs boson with a mass of 125 GeV. There are still profound questions to be addressed: how can the Higgs mass be 125 GeV without fine tuning, and are there indications from particle physics for the source of dark matter. A great deal of progress has been made in answering these questions over the last few years, most importantly which models of supersymmetry can easily be excluded. In addition, we developed a broad tool box of machinery for performing searches for new physics.

The lack of immediate evidence for supersymmetry also sparked additional work between theorists and experimentalists. For example, stealth supersymmetry is an experimentally motivated theory. We are now provided with a substantial set of gaps in the current analysis strategies, motivating us to look for new physics using less obvious strategies. Stealth SUSY is a unique example, because the search for SUSY does not rely on $E_{\mathrm{T}}^{\mathrm{miss}}$.

In this thesis, I present the summary of the search for stealth supersymmetry. In this model, we can exclude squarks up to a mass of 550 GeV. This analysis serves as an important compliment to existing searches, and is the first of its kind. This search serves as an example of how gaps in the experimental strategy can be filled. Future searches for supersymmetry will critically depend on covering all possible models and final states, and models such as stealth supersymmetry can provide a framework to identify these gaps and design new searches to target them.

In addition to searches, Run 1 has provided excellent measurements of standard model processes. Section 5 provides details of a measurement of Υ production using muons. This measurement demonstrates the exquisite momentum resolution of the CMS tracker, as can be clearly seen from the summary plots where the $\Upsilon(2S)$ and $\Upsilon(3S)$ states can easily be distinguished. We also provide an Υ cross section measurement up to $p_{\mathrm{T}} = 100\,\mathrm{GeV}$, the highest value yet reported. This measurement will

be useful for understanding the details of perturbative and non-perturbative QCD involved in Υ production at a hadron collider.

It is now only a few short months until the LHC begins collecting new data. Regardless of the result, this will be an exciting time to study particle interactions at unprecedented energies.

Bibliography

[1] C. Burgess and G. Moore, "The Standard Model: A Primer". Cambridge University Press, 2007.

[2] F. Englert and R. Brout, "Broken Symmetry and the Mass of Gauge Vector Mesons", *Phys. Rev. Lett.* **13** (Aug, 1964) 321–323, doi:10.1103/PhysRevLett.13.321.

[3] P. W. Higgs, "Broken Symmetries and the Masses of Gauge Bosons", *Phys. Rev. Lett.* **13** (Oct, 1964) 508–509, doi:10.1103/PhysRevLett.13.508.

[4] G. S. Guralnik, C. R. Hagen, and T. W. B. Kibble, "Global Conservation Laws and Massless Particles", *Phys. Rev. Lett.* **13** (Nov, 1964) 585–587, doi:10.1103/PhysRevLett.13.585.

[5] S. Weinberg, "A Model of Leptons", *Phys. Rev. Lett.* **19** (Nov, 1967) 1264–1266, doi:10.1103/PhysRevLett.19.1264.

[6] J. Goldstone, A. Salam, and S. Weinberg, "Broken Symmetries", *Phys. Rev.* **127** (Aug, 1962) 965–970, doi:10.1103/PhysRev.127.965.

[7] S. L. Glashow, "Partial-symmetries of weak interactions", *Nuclear Physics* **22** (1961), no. 4, 579 – 588, doi:10.1016/0029-5582(61)90469-2.

[8] H. D. Politzer, "Asymptotic Freedom: An Approach to Strong Interactions", *Phys. Rept.* **14** (1974) 129–180, doi:10.1016/0370-1573(74)90014-3.

[9] D. J. Gross and F. Wilczek, "Ultraviolet Behavior of Nonabelian Gauge Theories", *Phys. Rev. Lett.* **30** (1973) 1343–1346, doi:10.1103/PhysRevLett.30.1343.

[10] D. Gross and F. Wilczek, "Asymptotically Free Gauge Theories. 1", *Phys. Rev. D* **8** (1973) 3633–3652, doi:10.1103/PhysRevD.8.3633.

[11] H. D. Politzer, "Reliable Perturbative Results for Strong Interactions?", *Phys. Rev. Lett.* **30** (1973) 1346–1349, doi:10.1103/PhysRevLett.30.1346.

[12] Particle Data Group, J. Beringer et al., "Review of Particle Physics", *Phys. Rev. D.* **86** (2012) 010001, doi:10.1103/PhysRevD.86.010001.

[13] CMS Collaboration, "Observation of a new boson at a mass of 125 GeV with the CMS experiment at the LHC", *Phys. Lett. B* **716** (2012) 30–61, doi:10.1016/j.physletb.2012.08.021, arXiv:1207.7235.

[14] ATLAS Collaboration, "Observation of a new particle in the search for the Standard Model Higgs boson with the ATLAS detector at the LHC", *Phys. Lett. B* **716** (2012) 1–29, doi:10.1016/j.physletb.2012.08.020, arXiv:1207.7214.

[15] P. Artoisenet et al., "Υ Production at Fermilab Tevatron and LHC Energies", *Phys. Rev. Lett.* **101** (2008) 152001, doi:10.1103/PhysRevLett.101.152001, arXiv:0806.3282.

[16] S. Baranov, "Prompt $\Upsilon(nS)$ production at the LHC in view of the k_t-factorization approach", *Phys. Rev. D* **86** (2012) 054015, doi:10.1103/PhysRevD.86.054015.

[17] P. Cho and A. K. Leibovich, "Color-octet quarkonia production", *Phys. Rev. D* **53** (1996) 150, doi:10.1103/PhysRevD.53.150.

[18] P. Cho and A. K. Leibovich, "Color-octet quarkonia production. II", *Phys. Rev. D* **53** (1996) 6203, doi:10.1103/PhysRevD.53.6203.

[19] K. Wang, Y.-Q. Ma, and K.-T. Chao, "$\Upsilon(1S)$ prompt production at the Tevatron and LHC in nonrelativistic QCD", *Phys. Rev. D* **85** (2012) 114003, doi:10.1103/PhysRevD.85.114003, arXiv:1202.6012.

[20] S. P. Martin, "A Supersymmetry primer", *Adv.Ser.Direct.High Energy Phys.* **21** (2010) 1–153, arXiv:hep-ph/9709356.

[21] J. Wess and B. Zumino, "Supergauge transformations in four dimensions", *Nuclear Physics B* **70** (1974), no. 1, 39 – 50, doi:10.1016/0550-3213(74)90355-1.

[22] R. Kitano and Y. Nomura, "Supersymmetry, naturalness, and signatures at the LHC", *Phys. Rev. D* **73** (2006) 095004, doi:10.1103/PhysRevD.73.095004, arXiv:hep-ph/0602096.

[23] V. C. Rubin and J. Ford, W. Kent, "Rotation of the Andromeda Nebula from a Spectroscopic Survey of Emission Regions", *Astrophys. J.* **159** (1970) 379–403, doi:10.1086/150317.

[24] R. Massey, T. Kitching, and J. Richard, "The dark matter of gravitational lensing", *Rept. Prog. Phys.* **73** (2010) 086901, doi:10.1088/0034-4885/73/8/086901, arXiv:1001.1739.

[25] G. Bertone, D. Hooper, and J. Silk, "Particle dark matter: Evidence, candidates and constraints", *Phys. Rept.* **405** (2005) 279–390, doi:10.1016/j.physrep.2004.08.031, arXiv:hep-ph/0404175.

[26] R. Catena and L. Covi, "SUSY dark matter(s)", *Eur. Phys. J. C* **74** (2014) 2703, doi:10.1140/epjc/s10052-013-2703-4, arXiv:1310.4776.

[27] F. W. Savas Dimopoulus, Stuart Raby, "Unification of couplings", *Physics Today* **44** (1991) 25–33, doi:10.1063/1.881292.

[28] H. Georgi and S. L. Glashow, "Unity of All Elementary-Particle Forces", *Phys. Rev. Lett.* **32** (Feb, 1974) 438–441, doi:10.1103/PhysRevLett.32.438.

[29] R. Barbier et al., "R-parity violating supersymmetry", *Phys. Rept.* **420** (2005) 1, doi:10.1016/j.physrep.2005.08.006, arXiv:hep-ph/0406039.

[30] CMS Collaboration Collaboration, "Search for pair production of third-generation scalar leptoquarks and top squarks in proton-proton collisions at $\sqrt{s} = 8$ TeV", *Phys. Lett. B* **739** (2014) 229, doi:10.1016/j.physletb.2014.10.063, arXiv:1408.0806.

[31] J. A. Evans, Y. Kats, D. Shih, and M. J. Strassler, "Toward Full LHC Coverage of Natural Supersymmetry", *JHEP* **1407** (2014) 101, doi:10.1007/JHEP07(2014)101, arXiv:1310.5758.

[32] P. Meade, M. Reece, and D. Shih, "Prompt Decays of General Neutralino NLSPs at the Tevatron", *JHEP* **1005** (2010) 105, doi:10.1007/JHEP05(2010)105, arXiv:0911.4130.

[33] J. T. Ruderman and D. Shih, "General Neutralino NLSPs at the Early LHC", *JHEP* **1208** (2012) 159, doi:10.1007/JHEP08(2012)159, arXiv:1103.6083.

[34] L. Evans and P. Bryant, "LHC Machine", *JINST* **3** (2008) S08001, doi:10.1088/1748-0221/3/08/S08001.

[35] R. Alemany-Fernandez et al., "Operation and Configuration of the LHC in Run 1",.

[36] M. Lamont, "Status of the LHC", *Journal of Physics: Conference Series* **455** (2013), no. 1, 012001.

[37] W. Herr and B. Muratori, "Concept of luminosity",.

[38] CMS Collaboration, "The CMS experiment at the CERN LHC", *JINST* **3** (2008) S08004, doi:10.1088/1748-0221/3/08/S08004.

[39] CMS Collaboration, "CMS Physics: Technical Design Report Volume 1: Detector Performance and Software",. There is an error on cover due to a technical problem for some items.

[40] L. Taylor, "CMS detector overview".

[41] D. Green, "The physics of particle detectors", *Camb. Monogr. Part. Phys. Nucl. Phys. Cosmol.* **12** (2000) 1–361.

[42] B. Martin and G. Shaw, "Particle Physics". The Manchester Physics Series. Wiley, third edition, 2008.

[43] A. C. C. Herve, "The CMS detector magnet", *Applied Superconductivity, IEEE Transactions on* **10** (March, 2000) 389–394.

[44] CMS Collaboration, "The CMS magnet project: Technical Design Report". Technical Design Report CMS. CERN, Geneva, 1997.

[45] CMS Collaboration, "Precise Mapping of the Magnetic Field in the CMS Barrel Yoke using Cosmic Rays", *JINST* **5** (2010) T03021, doi:10.1088/1748-0221/5/03/T03021, arXiv:0910.5530.

[46] U. K. Vector Fields Ltd.. Oxford, "TOSCA/OPERA-3d Software". http://www.vectorfields.com.

[47] J. D. Jackson, "Classical electrodynamics; 3rd ed.". Wiley, New York, NY, 1999.

[48] CMS Collaboration Collaboration, "CMS Tracking Performance Results from early LHC Operation", *Eur.Phys.J.* **C70** (2010) 1165–1192, doi:10.1140/epjc/s10052-010-1491-3, arXiv:1007.1988.

[49] CMS Collaboration, "Description and performance of track and primary-vertex reconstruction with the CMS tracker", arXiv:1405.6569.

[50] C. Collaboration, "Studies of Tracker Material", Technical Report CMS-PAS-TRK-10-003, 2010.

[51] CMS Collaboration, "Measurement of Momentum Scale and Resolution of the CMS Detector using Low-mass Resonances and Cosmic Ray Muons", Technical Report CMS-PAS-TRK-10-004, CERN, 2010. Geneva, 2010.

[52] CMS Collaboration, "Electromagnetic calorimeter calibration with 7 TeV data", Technical Report CMS-PAS-EGM-10-003, CERN, Geneva, 2010.

[53] CMS Collaboration, C. Collaboration, "CMS Physics: Technical Design Report Volume 1: Detector Performance and Software". Technical Design Report CMS. CERN, Geneva, 2006.

[54] CMS Collaboration, "Photon reconstruction and identification at $\sqrt{s} = 7$ TeV", Technical Report CMS-PAS-EGM-10-005, CERN, 2010. Geneva, 2010.

[55] W. Adam, R. Frühwirth, A. Strandlie, and T. Todor, "Reconstruction of Electrons with the Gaussian-Sum Filter in the CMS Tracker at the LHC", Technical Report 9, CERN, Geneva, Jan, 2005.

[56] S. Baffioni et al., "Electron reconstruction in CMS", *Eur. Phys. J. C* **49** (2007) 1099–1116, doi:10.1140/epjc/s10052-006-0175-5.

[57] CMS Collaboration, "Electron reconstruction and identification at sqrt(s) = 7 TeV", Technical Report CMS-PAS-EGM-10-004, CERN, Geneva, 2010.

[58] CMS Collaboration, "Performance of CMS muon reconstruction in pp collision events at $\sqrt{s} = 7$ TeV", *JINST* **7** (2012) P10002, doi:10.1088/1748-0221/7/10/P10002, arXiv:1206.4071.

[59] C.-E. Wulz, "Concept of the First Level Global Trigger for the CMS experiment at LHC", *Nuclear Instruments and Methods in Physics Research Section A: Accelerators, Spectrometers, Detectors and Associated Equipment* **473** (2001), no. 3, 231 – 242, doi:10.1016/S0168-9002(01)00809-9.

[60] CMS Trigger and Data Acquisition Group Collaboration, "The CMS high level trigger", *Eur. Phys. J. C* **46** (2006) 605–667, doi:10.1140/epjc/s2006-02495-8, arXiv:hep-ex/0512077.

[61] L. A. et al, "Commissioning of the CMS High Level Trigger", *Journal of Instrumentation* **4** (2009), no. 10, P10005.

[62] G. B. et al, "The CMS High Level Trigger System: Experience and Future Development", *Journal of Physics: Conference Series* **396** (2012), no. 1, 012008.

[63] CMS Collaboration, "Data Parking and Data Scouting at the CMS Experiment",.

[64] CMS Collaboration, "Search for Narrow Resonances using the Dijet Mass Spectrum in pp Collisions at sqrt s of 7 TeV", Technical Report CMS-PAS-EXO-11-094, CERN, Geneva, 2012.

[65] A. D. Martin, W. J. Stirling, R. S. Thorne, and G. Watt, "Heavy-quark mass dependence in global PDF analyses and 3- and 4-flavour parton distributions", *Eur. Phys. J. C* **70** (2010) 51, doi:10.1140/epjc/s10052-010-1462-8, arXiv:1007.2624.

[66] G. Altarelli and G. Parisi, "Asymptotic Freedom in Parton Language", *Nucl. Phys. B* **126** (1977) 298, doi:10.1016/0550-3213(77)90384-4.

[67] Y. L. Dokshitzer, "Calculation of the Structure Functions for Deep Inelastic Scattering and e^+e^- Annihilation by Perturbation Theory in Quantum Chromodynamics.", *Sov. Phys. JETP* **46** (1977) 641–653.

[68] V. Gribov and L. Lipatov, "Deep inelastic e p scattering in perturbation theory", *Sov. J. Nucl. Phys.* **15** (1972) 438–450.

[69] T. Kinoshita, "Mass singularities of Feynman amplitudes", *J. Math. Phys.* **3** (1962) 650–677, doi:10.1063/1.1724268.

[70] T. Lee and M. Nauenberg, "Degenerate Systems and Mass Singularities", *Phys. Rev.* **133** (1964) B1549–B1562, doi:10.1103/PhysRev.133.B1549.

[71] G. C. Fox and S. Wolfram, "A Model for Parton Showers in QCD", *Nucl. Phys. B* **168** (1980) 285, doi:10.1016/0550-3213(80)90111-X.

[72] J. Alwall, S. de Visscher, and F. Maltoni, "QCD radiation in the production of heavy colored particles at the LHC", *JHEP* **0902** (2009) 017, doi:10.1088/1126-6708/2009/02/017, arXiv:0810.5350.

[73] J. Alwall et al., "Comparative study of various algorithms for the merging of parton showers and matrix elements in hadronic collisions", *Eur. Phys. J. C* **53** (2008) 473–500, doi:10.1140/epjc/s10052-007-0490-5, arXiv:0706.2569.

[74] S. Frixione and B. R. Webber, "Matching NLO QCD computations and parton shower simulations", *JHEP* **0206** (2002) 029, doi:10.1088/1126-6708/2002/06/029, arXiv:hep-ph/0204244.

[75] X. Artru and G. Mennessier, "String model and multiproduction", *Nucl. Phys. B* **70** (1974) 93–115, doi:10.1016/0550-3213(74)90360-5.

[76] B. Andersson, G. Gustafson, G. Ingelman, and T. Sjostrand, "Parton Fragmentation and String Dynamics", *Phys. Rept.* **97** (1983) 31–145, doi:10.1016/0370-1573(83)90080-7.

[77] D. Amati and G. Veneziano, "Preconfinement as a Property of Perturbative QCD", *Phys. Lett. B* **83** (1979) 87, doi:10.1016/0370-2693(79)90896-7.

[78] A. Bassetto, M. Ciafaloni, and G. Marchesini, "Color Singlet Distributions and Mass Damping in Perturbative QCD", *Phys. Lett. B* **83** (1979) 207, doi:10.1016/0370-2693(79)90687-7.

[79] R. D. Field and S. Wolfram, "A QCD Model for e^+ e^- Annihilation", *Nucl. Phys. B* **213** (1983) 65, doi:10.1016/0550-3213(83)90175-X.

[80] B. Webber, "A QCD Model for Jet Fragmentation Including Soft Gluon Interference", *Nucl. Phys. B* **238** (1984) 492, doi:10.1016/0550-3213(84)90333-X.

[81] T. Sjostrand and M. van Zijl, "A Multiple Interaction Model for the Event Structure in Hadron Collisions", *Phys. Rev. D* **36** (1987) 2019, doi:10.1103/PhysRevD.36.2019.

[82] J. Butterworth, J. R. Forshaw, and M. Seymour, "Multiparton interactions in photoproduction at HERA", *Z. Phys. C* **72** (1996) 637–646, doi:10.1007/s002880050286, arXiv:hep-ph/9601371.

[83] GEANT4 Collaboration, "GEANT4: A Simulation toolkit", *Nucl. Instrum. Meth. A* **506** (2003) 250–303, doi:10.1016/S0168-9002(03)01368-8.

[84] D. Orbaker, "Fast simulation of the CMS detector", *J. Phys.: Conf. Ser.* **219** (2009), no. 3, CERN-CMS-CR-2009-074, doi:10.1088/1742-6596/219/3/032053.

[85] S. Abdullin, P. Azzi, F. Beaudette, P. Janot, and A. Perrotta, "Fast simulation of the CMS detector at the LHC", *J. Phys.: Conf. Ser.* **331** (2010), no. 3, CERN-CMS-CR-2010-297, doi:10.1088/1742-6596/331/3/032049.

[86] J. Alwall et al., "MadGraph 5: going beyond", *JHEP* **06** (2011) 128, doi:10.1007/JHEP06(2011)128, arXiv:1106.0522.

[87] J. Pumplin et al., "New generation of parton distributions with uncertainties from global QCD analysis", *JHEP* **07** (2002) 012, doi:10.1088/1126-6708/2002/07/012, arXiv:hep-ph/0201195.

[88] S. Alioli, P. Nason, C. Oleari, and E. Re, "A general framework for implementing NLO calculations in shower Monte Carlo programs: the POWHEG BOX", *JHEP* **06** (2010) 043, doi:10.1007/JHEP06(2010)043, arXiv:1002.2581.

[89] CMS Collaboration, "Study of the underlying event at forward rapidity in pp collisions at $\sqrt{s} = 0.9$, 2.76, and 7 TeV", *JHEP* **1304** (2013) 072, doi:10.1007/JHEP04(2013)072, arXiv:1302.2394.

[90] R. Gavin, Y. Li, F. Petriello, and S. Quackenbush, "FEWZ 2.0: A code for hadronic Z production at next-to-next-to-leading order", *Comput.Phys.Commun.* **182** (2011) 2388–2403, doi:10.1016/j.cpc.2011.06.008, arXiv:1011.3540.

[91] M. Czakon, P. Fiedler, and A. Mitov, "Total Top-Quark Pair-Production Cross Section at Hadron Colliders Through $O(\alpha_S^4)$", *Phys.Rev.Lett.* **110** (2013), no. 25, 252004, doi:10.1103/PhysRevLett.110.252004, arXiv:1303.6254.

[92] N. Kidonakis and R. Vogt, "The Theoretical top quark cross section at the Tevatron and the LHC", *Phys.Rev.* **D78** (2008) 074005, doi:10.1103/PhysRevD.78.074005, arXiv:0805.3844.

[93] J. M. Campbell, R. K. Ellis, and C. Williams, "Vector boson pair production at the LHC", *JHEP* **1107** (2011) 018, doi:10.1007/JHEP07(2011)018, arXiv:1105.0020.

[94] W. Beenakker, R. Hopker, M. Spira, and P. Zerwas, "Squark and gluino production at hadron colliders", *Nucl.Phys.* **B492** (1997) 51–103, doi:10.1016/S0550-3213(97)80027-2, arXiv:hep-ph/9610490.

[95] W. Beenakker et al., "Soft-gluon resummation for squark and gluino hadroproduction", *JHEP* **0912** (2009) 041, doi:10.1088/1126-6708/2009/12/041, arXiv:0909.4418.

[96] A. Kulesza and L. Motyka, "Threshold resummation for squark-antisquark and gluino-pair production at the LHC", *Phys.Rev.Lett.* **102** (2009) 111802, doi:10.1103/PhysRevLett.102.111802, arXiv:0807.2405.

[97] A. Kulesza and L. Motyka, "Soft gluon resummation for the production of gluino-gluino and squark-antisquark pairs at the LHC", *Phys.Rev.* **D80** (2009) 095004, doi:10.1103/PhysRevD.80.095004, arXiv:0905.4749.

[98] M. Kramer et al., "Supersymmetry production cross sections in pp collisions at $\sqrt{s} = 7$ TeV", arXiv:1206.2892.

[99] R. Frühwirth, "Application of Kalman filtering to track and vertex fitting", *Nucl. Instrum. Meth. A* **262** (1987) 444–450, doi:10.1016/0168-9002(87)90887-4.

[100] R. Frühwirth, W. Waltenberger, and P. Vanlaer, "Adaptive vertex fitting", *J. Phys. G* **34** (2007) N343, doi:10.1088/0954-3899/34/12/N01.

[101] S. D. Ellis and D. E. Soper, "Successive combination jet algorithm for hadron collisions", *Phys. Rev. D* **48** (1993) 3160–3166, doi:10.1103/PhysRevD.48.3160, arXiv:hep-ph/9305266.

[102] M. Wobisch and T. Wengler, "Hadronization corrections to jet cross-sections in deep inelastic scattering", arXiv:hep-ph/9907280.

[103] G. C. Blazey et al., "Run II jet physics", arXiv:hep-ex/0005012.

[104] A. Ali and G. Kramer, "Jets and QCD: A Historical Review of the Discovery of the Quark and Gluon Jets and its Impact on QCD", *Eur. Phys. J H.* **36** (2011) 245–326, doi:10.1140/epjh/e2011-10047-1, arXiv:1012.2288.

[105] CMS Collaboration, "Particle-Flow Event Reconstruction in CMS and Performance for Jets, Taus, and MET", Technical Report CMS-PAS-PFT-09-001, CERN, 2009. Geneva, Apr, 2009.

[106] M. Cacciari, G. P. Salam, and G. Soyez, "The Anti-k(t) jet clustering algorithm", *JHEP* **0804** (2008) 063, doi:10.1088/1126-6708/2008/04/063, arXiv:0802.1189.

[107] CMS Collaboration Collaboration, "Determination of Jet Energy Calibration and Transverse Momentum Resolution in CMS", *JINST* **6** (2011) P11002, doi:10.1088/1748-0221/6/11/P11002, arXiv:1107.4277.

[108] CMS Collaboration, "Identification of b-quark jets with the CMS experiment", *JINST* **8** (2013) P04013, doi:10.1088/1748-0221/8/04/P04013, arXiv:1211.4462.

[109] W. Adam, R. Frühwirth, A. Strandlie, and T. Todor, "Reconstruction of Electrons with the Gaussian-Sum Filter in the CMS Tracker at the LHC", Technical Report CMS-NOTE-2005-001, CERN, Geneva, Jan, 2005.

[110] CMS Collaboration, "Particle-flow commissioning with muons and electrons from J/ψ and W events at 7 TeV", CMS Physics Analysis Summary CMS-PAS-PFT-10-003, 2010.

[111] R. D. Cousins, J. T. Linnemann, and J. Tucker, "Evaluation of three methods for calculating statistical significance when incorporating a systematic uncertainty into a test of the background-only hypothesis for a Poisson process", *Nucl. Instrum. Meth. A* **595** (2008) 480–501, doi:10.1016/j.nima.2008.07.086.

[112] CMS Collaboration, "Performance of b tagging at $\sqrt{s} = 8$ TeV in multijet, $\mathrm{t\bar{t}}$ and boosted topology events", *CMS PAS BTV-13-001* (2013).

[113] CMS Collaboration, "Measurement of W+W- and ZZ production cross sections in pp collisions at sqrt(s) = 8 TeV", *Phys. Lett. B* **721** (2013) 190–211, doi:10.1016/j.physletb.2013.03.027, arXiv:1301.4698.

[114] CMS Collaboration, "CMS Luminosity Based on Pixel Cluster Counting - Summer 2013 Update", CMS Physics Analysis Summary CMS-PAS-LUM-13-001, 2013.

[115] A. L. Read, "Presentation of search results: the CLs technique", *Journal of Physics G: Nuclear and Particle Physics* **28** (2002), no. 10, 2693.

[116] CMS Collaboration, "Precise determination of the mass of the Higgs boson and tests of compatibility of its couplings with the standard model predictions using proton collisions at 7 and 8 TeV", arXiv:1412.8662.

[117] B. Mistlberger and F. Dulat, "Limit setting procedures and theoretical uncertainties in Higgs boson searches", arXiv:1204.3851.

[118] G. Cowan, C. K., G. E., and V. O., "Asymptotic formulae for likelihood-based tests of new physics", *Eur. Phys. J. C* **71** (2011) 1554, doi:10.1140/epjc/s10052-011-1554-0.

[119] CMS Collaboration, "Measurement of the Υ(1S), Υ(2S) and Υ(3S) polarizations in *pp* collisions at $\sqrt{s} = 7$ TeV", *Phys. Rev. Lett.* **110** (2013) 081802, doi:10.1103/PhysRevLett.110.081802, arXiv:1209.2922. arXiv:1209.2922, CMS-BPH-11-023, CERN-PH-EP-2012-205.

[120] E. Braaten, D. Kang, J. Lee, and C. Yu, "Optimal spin-quantization axes for the polarization of dileptons with large transverse momentum", *Phys. Rev. D* **79** (Jan, 2009) 014025, doi:10.1103/PhysRevD.79.014025.

[121] CMS Collaboration, "Measurement of the $\Upsilon(1S), \Upsilon(2S)$, and $\Upsilon(3S)$ cross sections in pp collisions at $\sqrt{s} = 7$ TeV", *Phys. Lett. B* **727** (2013) 101, doi:10.1016/j.physletb.2013.10.033, arXiv:1303.5900.

[122] E. Barberio, B. van Eijk, and Z. Wąs, "PHOTOS: A universal Monte Carlo for QED radiative corrections in decays", *Comput. Phys. Commun.* **66** (1991) 115, doi:10.1016/0010-4655(91)90012-A.

[123] E. Barberio and Z. Wąs, "PHOTOS: A universal Monte Carlo for QED radiative corrections: Version 2.0", *Comput. Phys. Commun.* **79** (1994) 291, doi:10.1016/0010-4655(94)90074-4.

[124] W. Verkerke and D. P. Kirkby, "The RooFit toolkit for data modeling", *eConf* **C0303241** (2003) MOLT007, arXiv:physics/0306116.

[125] H. Akaike, "A new look at the statistical model identification", *IEEE Transactions on Automatic Control* **19** (1974) 716, doi:10.1109/TAC.1974.1100705.

[126] K. Burnham and D. Anderson, "Multimodel Inference: Understanding AIC and BIC in Model Selection", *Sociological Methods Research* **33** (2004) 261, doi:10.1177/0049124104268644.

[127] B. Gong, L.-P. Wan, J.-X. Wang, and H.-F. Zhang, "Complete next-to-leading-order study on the yield and polarization of Upsilon(1S, 2S, 3S) at the Tevatron and LHC", *Phys. Rev. Lett.* **112** (2014) 032001, doi:10.1103/PhysRevLett.112.032001, arXiv:1305.0748.